

# Measurement of inelastic $J/\psi$ production in deep inelastic $ep$ scattering at Hera

Dissertation  
zur Erlangung des Doktorgrades  
des Fachbereichs Physik  
der Universität Hamburg

vorgelegt von Alexei Antonov  
aus Moskau

Hamburg, 2007

Gutachter der Dissertation:	Prof. Dr. R. Klanner JProf. Dr. J. Haller
Gutachter der Disputation:	Prof. Dr. R. Klanner Dr. A. Geiser
Datum der Disputation:	27.07.2007
Vorsitzender des Prüfungsausschusses:	Prof. Dr. E. Heumann
Vorsitzender des Promotionsausschusses:	Prof. Dr. G. Huber
MIN-Dekan des Fakultät Physik:	Prof. Dr. A. Frühwald

## Abstract

This thesis presents a measurement of the inelastic production of  $J/\psi$  mesons in  $ep$  collisions with the ZEUS detector at HERA using an integrated luminosity of  $109 \text{ pb}^{-1}$ . The  $J/\psi$  mesons were identified using the decay channel  $J/\psi \rightarrow \mu^+\mu^-$ . The measurements were performed in the kinematic range  $2 < Q^2 < 80 \text{ GeV}^2$ ,  $50 < W < 250 \text{ GeV}$ ,  $0.2 < z < 0.9$  and  $-1.6 < Y_{lab} < 1.3$ , where  $Q^2$  is the virtuality of the exchanged photon,  $W$  is the photon-proton centre-of-mass energy,  $z$  is the fraction of the photon energy carried by the  $J/\psi$  meson in the proton rest frame and  $Y_{lab}$  is the rapidity of the  $J/\psi$  in the laboratory frame. The measured cross sections are compared to theoretical predictions within the non-relativistic QCD framework including colour-singlet and colour-octet contributions, as well as to predictions based on the  $k_T$ -factorisation approach. Calculations of the colour-singlet process generally agree with the data, whereas inclusion of colour-octet terms spoils this agreement.

As a technical part of this thesis, the Straw-Tube Tracker (STT) GEANT simulation and track reconstruction software developed. Studies of the STT performance with MC data and real data presented.

## Kurzfassung

Diese Dissertation beschreibt eine Messung inelastischer  $J/\psi$ -Meson-Produktion in  $ep$  Kollisionen mit dem ZEUS Detektor bei HERA unter Verwendung einer integrierten Luminosität von  $109 \text{ pb}^{-1}$ . Die  $J/\psi$ -Mesonen wurden mit Hilfe des Zerfallskanals  $J/\psi \rightarrow \mu^+\mu^-$  identifiziert. Die Messungen wurden im kinematischen Bereich  $2 < Q^2 < 80 \text{ GeV}^2$ ,  $50 < W < 250 \text{ GeV}$ ,  $0.2 < z < 0.9$  und  $-1.6 < Y_{lab} < 1.3$  durchgeführt. Dabei beschreibt  $Q^2$  die Virtualität des ausgetauschten Photons,  $W$  die Photon-Proton-Schwerpunktsenergie,  $z$  den Anteil der Photon Energie, die vom  $J/\psi$ -Meson im Ruhesystem des Protons getragen wird und  $Y_{lab}$  die Rapidität des  $J/\psi$  im Laborsystem. Die gemessenen Wirkungsquerschnitte werden mit theoretischen Vorhersagen der nicht-relativistischen QCD, unter Berücksichtigung von Farb-Singulett- und Farb-Oktett-Beiträgen, wie auch mit Vorhersagen des  $k_T$ -Faktorisierungsansatzes verglichen. Berechnungen des Farb-Singulett-Prozesses stimmen im Allgemeinen mit den Daten überein, während mit Einbeziehen von Farb-Oktett-Termen keine Übereinstimmung erreicht wird.

Als technischer Teil dieser Arbeit wurde die Straw-Tube-Tracker (STT) GEANT-Simulation und Spurrekonstruktionssoftware entwickelt. Es werden Studien der STT-Leistung mit MC-Daten und echten Daten vorgestellt.



## **Contents**

---

# Contents

## Contents

<b>List of Figures</b>	<b>iii</b>
<b>1 Introduction</b>	<b>1</b>
<b>2 Phenomenology of Charmonium Production</b>	<b>5</b>
2.1 Charmonium . . . . .	5
2.2 Deep Inelastic Scattering . . . . .	8
2.3 DIS Kinematics . . . . .	9
2.4 Structure Functions . . . . .	11
2.5 Quark Parton Model . . . . .	12
2.6 Quantum Chromodynamics . . . . .	13
2.7 QCD factorization and parton densities . . . . .	14
2.8 Parton Evolution . . . . .	15
2.8.1 DGLAP evolution . . . . .	16
2.8.2 BFKL evolution and $k_T$ factorization . . . . .	18
2.8.3 CCFM equation . . . . .	19
2.9 Charm Production in DIS . . . . .	19
2.9.1 Boson-Gluon-Fusion . . . . .	20
2.10 Inelastic Charmonium production in DIS . . . . .	21
2.10.1 The Color Evaporation Model . . . . .	21
2.10.2 The Color Singlet Model . . . . .	22
2.10.3 Non-relativistic QCD factorization method . . . . .	23

<b>3</b>	<b>The ZEUS detector at HERA</b>	<b>27</b>
3.1	The HERA collider . . . . .	27
3.2	The ZEUS Detector . . . . .	30
3.2.1	The Central Tracking Detector (CTD) . . . . .	33
3.2.2	The Uranium–scintillator Calorimeter (UCAL) . . . . .	36
3.2.3	The Muon Detectors . . . . .	39
3.2.4	The Small Angle Tracking Detector (SRTD) . . . . .	44
3.2.5	The Hadron Electron Separator (HES) . . . . .	44
3.2.6	The Luminosity Measurement . . . . .	44
3.2.7	The ZEUS trigger system . . . . .	46
3.3	ZEUS Detector Simulation . . . . .	51
<b>4</b>	<b>Event reconstruction and data selection</b>	<b>53</b>
4.1	Kinematic reconstruction . . . . .	53
4.1.1	Electron method . . . . .	55
4.1.2	Jacquet-Blondel method [94] . . . . .	55
4.1.3	Double angle method [95] . . . . .	56
4.1.4	The $\Sigma$ method [96] . . . . .	56
4.1.5	The $J/\psi$ kinematic variables reconstruction . . . . .	57
4.1.6	For this analysis . . . . .	57
4.2	Event reconstruction . . . . .	58
4.2.1	Track and vertex reconstruction . . . . .	58
4.3	Reconstruction of the hadronic system . . . . .	59
4.3.1	Hadronic energy flow reconstruction . . . . .	60
4.3.2	Corrections for the presence of muons . . . . .	62
4.4	Identification and reconstruction of the scattered lepton . . . . .	64
4.4.1	Electron identification . . . . .	64
4.4.2	Electron position reconstruction . . . . .	64
4.5	Muon reconstruction . . . . .	67
4.5.1	The BREMAT matching package . . . . .	67
4.5.2	The MV muon finder . . . . .	70
4.6	$E - p_z$ cut . . . . .	72
4.7	Trigger chain for online data selection . . . . .	73
4.7.1	First and second level trigger . . . . .	73
4.7.2	Third level trigger . . . . .	75
4.7.3	The data samples . . . . .	76
4.8	Offline data selection . . . . .	76

---

4.8.1	Selection of the neutral current DIS event sample . . . . .	76
4.8.2	$J/\psi$ reconstruction . . . . .	78
4.8.3	Kinematic cuts . . . . .	80
4.8.4	Further inelastic events selection . . . . .	82
4.8.5	Summary of the offline selection cuts and $J/\psi$ signal . . . . .	83
4.9	Monte Carlo models . . . . .	86
4.9.1	Control plots and resolutions . . . . .	88
<b>5</b>	<b>Inelastic <math>J/\psi</math> Production in DIS</b>	<b>93</b>
5.1	Cross section measurement . . . . .	93
5.2	Systematic uncertainties . . . . .	99
5.3	Results . . . . .	100
5.4	Conclusions . . . . .	101
<b>6</b>	<b>HERA II and the ZEUS Straw-Tube Tracker</b>	<b>107</b>
6.1	The HERA luminosity upgrade . . . . .	107
6.2	The ZEUS upgrade . . . . .	108
6.3	The ZEUS Straw-Tube Tracker . . . . .	111
6.3.1	The STT detector . . . . .	111
6.3.2	The STT readout electronics . . . . .	113
6.3.3	The STT Monte-Carlo simulation . . . . .	114
6.3.4	The STT pattern recognition program STRECON . . . . .	120
6.3.5	Study of the STT performance with real data . . . . .	127
6.3.6	Conclusions . . . . .	133
<b>7</b>	<b>Summary and outlook</b>	<b>139</b>
<b>A</b>	<b>Values of the cross sections</b>	<b>143</b>



# List of Figures

2.1	Discovery of the $J/\psi$ at BNL and SLAC. On the left the invariant $e^+e^-$ mass spectrum in the reaction $p\text{ Be} \rightarrow e^+e^- + X$ , on the right the energy dependence of the $e^+e^-$ cross section. . . . .	6
2.2	Level diagram of the Charmonium family. . . . .	7
2.3	Diagrams for the a) strong decay of the $J/\psi$ into two mesons consisting of light quarks $q_1, q_2$ and b) the electromagnetic decay into two leptons $l^+, l^-$ . . . . .	8
2.4	Neutral Current ( <i>left</i> ) and Charged Current ( <i>right</i> ) DIS. . . . .	9
2.5	Kinematics of Neutral Current DIS. . . . .	10
2.6	Altarelli-Parisi splitting functions. . . . .	15
2.7	Gluon ladder showing the effect of several gluons radiated from the parton which interacts with the virtual photon. . . . .	17
2.8	BGF diagrams at the leading (left), next-to-leading order (center) and in the $k_T$ -factorization (right). In the latter case, the gluon entering the hard process (dot-dashed box) is free to be off-shell .	19
2.9	Boson Gluon Fusion in DIS. . . . .	20
2.10	A leading order graph for $J/\psi$ production in the Colour Singlet Model. . . . .	23
2.11	Generic diagrams of Charmonium production mechanisms: photon-gluon fusion via a “ $2 \rightarrow 1$ ” process (top left) and “ $2 \rightarrow 2$ ” processes (remaining diagrams). All the diagrams contribute via color-octet mechanisms, while the top right diagram can also contribute via color-singlet mechanism. Additional soft gluons emitted during the hadronizations process are not shown. . . . .	25
3.1	The HERA storage ring with its pre-accelerators system. . . . .	28
3.2	Integrated luminosity delivered by HERA (left) and usable for ZEUS physics analyses (right) in the 1993–2000 running period. .	30

3.3	The ZEUS coordinate system. . . . .	31
3.4	Cross section of the ZEUS detector along the beam axis. . . . .	32
3.5	$x - y$ cross section of one octant of the CTD. The sense wires are indicated with dots. . . . .	34
3.6	Hits coming from a genuine track (solid rectangles) tend to cross the cell boundaries within a superlayer. The open rectangles are ghost hits. . . . .	35
3.7	The track helix in the $xy$ plane. . . . .	36
3.8	Schematic view of the UCAL along the beam axis. . . . .	38
3.9	A FCAL module. . . . .	39
3.10	Schematic view of the forward muon detector along the beam axis	40
3.11	Layout of the barrel and rear muon detector . . . . .	42
3.12	SRTD layout . . . . .	43
3.13	Schematic view of the lumi monitor system . . . . .	45
3.14	Schematic diagram of the ZEUS trigger and data acquisition system.	50
4.1	A schematic view of a DIS-Event. The initial state is, apart from initial state radiation, completely determined by the HERA-beam parameters. . . . .	54
4.2	CTD and CAL resolutions . . . . .	59
4.3	The different types of energy flow objects which can be formed using a combination of calorimeter and CTD information. . . . .	60
4.4	Left: Schematic diagram of the cell-island algorithm in two dimensions. Right: Schematic diagram of cell-islands combination to cone islands. . . . .	61
4.5	Muonic energy in the CAL as a function of $\theta$ . . . . .	63
4.6	Angular MC resolution (in rad) for the scattered electron as determined with different detector components. . . . .	65
4.7	The fraction of events reconstructed using the SRTD, HES or RCAL. . . . .	67
4.8	The energy deposition and the number of cells with a signal in muon cluster for different sections of CAL. [100] . . . . .	71
4.9	Comparison of the $(E - p_Z)$ distributions after all selection cuts for the data and the EPJPSI MC. The vertical lines show the range selected for this analysis. The MC sample was normalized to the number of events in data between $(E - p_Z)$ values of 50 and 60 GeV.	77

4.10	Comparison of the $Z_{vertex}$ distributions after all selection cuts for the data and the EPJPSI MC. The symbols are the same as in Figure 4.9. . . . .	78
4.11	A candidate event for inelastic $J/\psi$ production in DIS, shown in the side view (left), radial view(right) of the ZEUS detector. The invariant mass of the $\mu^+\mu^-$ pair is 3.08 GeV, $Q^2 = 20.7 \text{ GeV}^2$ , $W = 208 \text{ GeV}$ , $z = 0.45$ . . . . .	79
4.12	Distribution of the kinematic variables $Q^2$ and $W$ for the event sample after all selection cuts, compared to the Monte-Carlo simulation. . . . .	81
4.13	Distributions of the $N_{tracks}$ for diffractive (EPSOFT) and non diffractive (EPJPSI) Monte-Carlo simulations after all selection cuts. . . . .	82
4.14	Invariant mass spectrum after all selection cuts in the kinematic region $2 < Q^2 < 80 \text{ GeV}^2$ , $50 < W < 250 \text{ GeV}$ , $0.2 < z < 0.9$ and $-1.6 < Y_{lab} < 1.3$ . The curve is the result of the fit with a modified Gaussian for the signal (see text) and a linear function (P1) for the non-resonant background. . . . .	84
4.15	Invariant mass spectrum after all selection cuts in the kinematic region $2 < Q^2 < 100 \text{ GeV}^2$ , $50 < W < 225 \text{ GeV}$ , $0.3 < z < 0.9$ and $p_T^{*2} > 1 \text{ GeV}^2$ defined in the H1 published paper [33]. The curve is the result of the fit with a modified Gaussian (see Eq. 4.21) for the signal and a linear function (P1) for the non-resonant background. . . . .	85
4.16	Resolution of $Q^2$ and $W$ in the kinematic region $2 < Q^2 < 80 \text{ GeV}^2$ , $50 < W < 250 \text{ GeV}$ , $0.2 < z < 0.9$ and $-1.6 < Y_{lab} < 1.3$ : the relative difference of reconstructed and generated values, the profile histogram of the ratio of reconstructed and generated values versus reconstructed value shown with the spread option. . . . .	89
4.17	Resolution of $z$ in the kinematic region $2 < Q^2 < 80 \text{ GeV}^2$ , $50 < W < 250 \text{ GeV}$ , $0.2 < z < 0.9$ and $-1.6 < Y_{lab} < 1.3$ shown as the relative difference, the profile histogram of the ratio (spread option) and the correlation of reconstructed and generated values. . . . .	90
4.18	Shape comparison between the data (dots) and the EPJPSI MC (after bin-by-bin reweighting in $Q^2$ and $p_T^{*2}$ ) in the kinematic region $2 < Q^2 < 80 \text{ GeV}^2$ , $50 < W < 250 \text{ GeV}$ , $0.2 < z < 0.9$ and $-1.6 < Y_{lab} < 1.3$ . Number of reconstructed $J/\psi$ mesons is shown as a function of $Y_X$ , track multiplicity, polar angle of the scattered lepton, $\delta$ , pseudorapidity of decay muons and energy deposit in a cone of $35^\circ$ . . . . .	91

5.1	Mixture of two MC samples fitted to the multiplicity distribution in the kinematic region $2 < Q^2 < 80 \text{ GeV}^2$ , $50 < W < 250 \text{ GeV}$ , $0.2 < z < 0.9$ and $-1.6 < Y_{lab} < 1.3$ without multiplicity cut. The data are shown as crosses, CASCADE as dotted line and EPSOFT as dash-dotted line. The sum CASCADE (70%) + EPSOFT (30%) is shown as dashed line. . . . .	94
5.2	Shape comparison between the data (dots) and the EPJPSI MC (after bin-by-bin reweighting in $Q^2$ and $p_T^{*2}$ ) in the kinematic region $2 < Q^2 < 80 \text{ GeV}^2$ , $50 < W < 250 \text{ GeV}$ , $0.2 < z < 0.9$ and $-1.6 < Y_{lab} < 1.3$ . Number of reconstructed $J/\psi$ mesons is shown as a function of $z$ , $Q^2$ , $W$ , $p_T^{*2}$ , $Y^*$ , $M_X^2$ . . . . .	95
5.3	Shape comparison between the data (dots) and the EPJPSI MC (after bin-by-bin reweighting in $Q^2$ and $p_T^{*2}$ ) in the kinematic region $2 < Q^2 < 100 \text{ GeV}^2$ , $50 < W < 225 \text{ GeV}$ , $0.3 < z < 0.9$ and $p_T^{*2} > 1 \text{ GeV}^2$ . Number of reconstructed $J/\psi$ mesons is shown as a function of $z$ , $Q^2$ , $W$ , $p_T^{*2}$ , $Y^*$ and $\log M_X^2$ . . . . .	96
5.4	Radiative (LO electroweak) corrections obtained using RAPGAP+HERACLES. in a $W - Q^2$ grid. The grid is made of 8 equidistant bins in $W$ and 4 nominal analysis bins in $Q^2$ : $2 < Q^2 < 4 \text{ GeV}^2$ , $4 < Q^2 < 8 \text{ GeV}^2$ , $8 < Q^2 < 16 \text{ GeV}^2$ , $2 < Q^2 < 80 \text{ GeV}^2$ (right plot) or $2 < Q^2 < 100 \text{ GeV}^2$ (left plot). The correction is the ratio $\sigma_{Born}/\sigma_{obs}$ , where $\sigma_{Born}$ is the Born-level cross section and $\sigma_{obs}$ is the cross section measured in the data. . . . .	98
5.5	Differential cross sections for the reaction $ep \rightarrow eJ/\psi X$ in the kinematic region $2 < Q^2 < 80 \text{ GeV}^2$ , $50 < W < 250 \text{ GeV}$ , $0.2 < z < 0.9$ and $-1.6 < Y_{lab} < 1.3$ as a function of (a) $z$ , (c) $Q^2$ and (e) $W$ . The inner error bars of the data points show the statistical uncertainty; the outer bars show statistical and systematic uncertainties added in quadrature. The data are compared to LO NRQCD predictions, a LO CS calculation, a prediction in the $k_T$ -factorisation approach within the CSM and the CASCADE MC predictions. (b), (d) and (f) show the data and the theoretical predictions normalised to unit area. . . . .	102

5.6 Differential cross sections for the reaction  $ep \rightarrow eJ/\psi X$  in the kinematic region  $2 < Q^2 < 80 \text{ GeV}^2$ ,  $50 < W < 250 \text{ GeV}$ ,  $0.2 < z < 0.9$  and  $-1.6 < Y_{lab} < 1.3$  as a function of (a)  $p_T^{*2}$  and (c)  $Y^*$ . The inner error bars of the data points show the statistical uncertainty; the outer bars show statistical and systematic uncertainties added in quadrature. The data are compared to LO NRQCD predictions, a LO CS calculation, a prediction in the  $k_T$ -factorisation approach within the CSM and the CASCADE MC predictions. (b), (d) show the data and the theoretical predictions normalised to unit area. . . . . 103

5.7 Differential cross sections for the reaction  $ep \rightarrow eJ/\psi X$  in the kinematic region  $2 < Q^2 < 80 \text{ GeV}^2$ ,  $50 < W < 250 \text{ GeV}$ ,  $0.2 < z < 0.9$  and  $-1.6 < Y_{lab} < 1.3$  as a function of (a)  $\log M_X^2$  and (c)  $Y_X$ . The inner error bars of the data points show the statistical uncertainty; the outer bars show statistical and systematic uncertainties added in quadrature. The data are compared to LO NRQCD predictions, a LO CS calculation, a prediction in the  $k_T$ -factorisation approach within the CSM and the CASCADE MC predictions. (b), (d) show the data and the theoretical predictions normalised to unit area. . . . . 104

5.8 Differential cross sections for the reaction  $ep \rightarrow eJ/\psi X$  in the kinematic region  $2 < Q^2 < 100 \text{ GeV}^2$ ,  $50 < W < 225 \text{ GeV}$ ,  $0.3 < z < 0.9$  and  $p_T^{*2} > 1 \text{ GeV}^2$  as a function of (a)  $z$ , (c)  $p_T^{*2}$  and (e)  $Y^*$ . The inner error bars of the data points show the statistical uncertainty; the outer bars show statistical and systematic uncertainties added in quadrature. The ZEUS and H1 data are compared to LO NRQCD predictions, a LO CS calculation, a prediction in the  $k_T$ -factorisation approach within the CSM and the CASCADE MC predictions. The H1 data points are plotted at the mean value of the data in each interval [33]. The ZEUS data for the  $p_T^{*2}$  differential cross section are plotted at the weighted mean, for each bin, of the EPJPSI MC prediction. (b), (d) and (f) show the data and the theoretical predictions normalised to unit area. . . . . 105

6.1 Integrated luminosity delivered by HERA (a) and collected by ZEUS (b) in the 2002-2007 years. . . . . 108

6.2	Location of the spin rotators on the HERA ring. . . . .	109
6.3	Schematic view of the upgraded ZEUS detector. . . . .	109
6.4	The polar angle distribution of charm quarks and hadrons for different values of $Q^2$ . Solid line $Q^2 = 1 \text{ GeV}^2$ , dashed line $Q^2 = 10 \text{ GeV}^2$ , dot-dashed line $Q^2 = 100 \text{ GeV}^2$ , short dashed line $Q^2 = 1000 \text{ GeV}^2$ . The cross sections have all been normalised to the same area. . . . .	110
6.5	The complete straw tube tracker. STT1 is in the TRD1-2 gap, while STT2 is in the TRD3-4 gap. Each TRD gap contains 2 super-layers and each super-layer contains two planes rotated by $30^\circ$ with respect to each other. The super-layers are rotated by $15^\circ$ with respect to each other. In the figure pairs of superlayers in each gap are artificially separated for clarity. . . . .	111
6.6	Single STT sector and arrangement of straws in it. . . . .	112
6.7	The STT readout. . . . .	114
6.8	The average signal from monitor analog output ASDQ using $^{55}\text{Fe}$ source. The gas mixture is Ar/CO <sub>2</sub> 80/20, HV=1850 V. . . . .	115
6.9	The STT geometry structure in the GEANT simulation. Parts of a sector(top left) the STT half with a support structure(bottom left) and the STT geometry tree in GEANT. . . . .	116
6.10	Full STT detector and new magnets in GEANT. . . . .	117
6.11	Simulation of the electrons drift for the STT straw tube. . . . .	118
6.12	Drift time vs drift distance, Monte Carlo (left) and test beam data (right) using 1 ns clock TDC. . . . .	119
6.13	Drift time vs drift distance distribution for MC data and 2004 data data taking, using 104 MHz FADC . . . . .	119
6.14	Single straw efficiency for different Lorentz factor of ionising particle MC data (solid) and the test beam data (dashed). . . . .	120
6.15	Number of straws used in STRECON track candidate for real data (left) and MC data (right). . . . .	120
6.16	Single straw drift radius measurement resolution for test beam data(left) and the STT GEANT simulation (right). . . . .	121
6.17	Wire orientations in the ZEUS straw-tube tracker. In this representation, the beam is oriented vertical to the page, displaced towards the bottom of the page. . . . .	122
6.18	Hough transform of a single simulated track in the ZEUS straw-tube tracker. . . . .	122

6.19	Hough transform of a set of simulated tracks in the ZEUS straw-tube tracker. . . . .	123
6.20	Schematic view of the STT1 and STT2 candidates matching. . .	124
6.21	The STRECON resolution of primary vertex Z position. . . . .	125
6.22	The STREON efficiency dependence on polar angle (left) and generated momentum (right) for MC DIS sample. . . . .	126
6.23	The occupancy distribution in the STT (MC DIS sample) as a function of straw Z and R positions (left) and single electron track GEANT simulation (right). . . . .	127
6.24	Amount of material collected on a forward track from vertex to FCAL surface. . . . .	128
6.25	The STREON efficiency dependence on number of fiducial tracks in event for MC DIS sample. Open circles is an efficiency for the MC sample with all processes of particles interaction with material switched off in GEANT. Reconstruction efficiency with all processes simulated in GEANT is indicated by filled squares. Points at zero show an average efficiency. . . . .	129
6.26	Example of STT reconstruction for data taken in a year 2004. Number of fired STT straws per event (left), number of found STT candidates per event (middle) and pseudorapidity of found STT candidates (right). . . . .	129
6.27	The STRECON CPU time consumption for one event. . . . .	130
6.28	The STT FADC pulstrain example for data taken in a year 2004. Pulstrain contains drift time spectra of 6 straws combined in one read-out channel. . . . .	131
6.29	The STT average T0 for 2004 (right) and 2006 (left). The error bars indicates an RMS of T0 distribution. . . . .	131
6.30	The mean values of residuals between STRECON fit and drift radius measurement. for all STT sectors without alignment (left) and with alignment (right). The error bars indicates an RMS of residuals distribution. . . . .	132
6.31	Distribution of residuals between the STRECON track fit position and a straw drift radius measurement. Left and central figures present the residuals before and after alignment applied. Comparison of 2004 data and MC (right) sigmas of residuals over all STT sectors. . . . .	132
6.32	Number of dead straws in the STT during 2004–2006 data taking.	134

6.33 Reconstructed tracks in forward detector as seen at ZEUS event display. . . . .	135
6.34 A muon from a decaying $J/\psi$ has been measured in the STT. . .	136
6.35 ZEUS event display with forward track reconstructed only in STT and FTD's. . . . .	136
6.36 The effect of inactive material in forward region of the ZEUS detector. GEANT simulated display of the same DIS event with all processes of interactions with material switched off (left) and on (right). . . . .	137
6.37 An event with two jets in forward region as seen at ZEUS event display. . . . .	137

# List of Tables

3.1	Main design parameters of HERA [63]. . . . .	29
3.2	Overview of the luminosity delivered by HERA from 1992 to 2000.	29
3.3	Angular coverage of the CAL parts and dimensions of the cells .	37
4.1	HERA running conditions and ZEUS gated luminosities . . . . .	76
4.2	Summary of the main offline selection cuts . . . . .	83
6.1	The overall specification of the straw-tube tracker . . . . .	113
6.2	Pattern finding efficiency using STT alone determined using MC simulation. . . . .	124
6.3	CTD/MVD to STT matching probability for DATA and MC. . .	133
A.1	Differential cross sections and normalised differential cross sections in the kinematic region $2 < Q^2 < 80 \text{ GeV}^2$ , $50 < W < 250 \text{ GeV}$ , $0.2 < z < 0.9$ and $-1.6 < Y_{lab} < 1.3$ as a function of $z$ and $W$ . The first uncertainty is statistical and the second is systematic. Overall normalisation uncertainties due to the luminosity measurement ( $\pm 2\%$ ) and to the $J/\psi$ decay branching ratio (1.7%) are not included in the systematic error. . . . .	143
A.2	Differential cross sections and normalised differential cross sections in the kinematic region $2 < Q^2 < 80 \text{ GeV}^2$ , $50 < W < 250 \text{ GeV}$ , $0.2 < z < 0.9$ and $-1.6 < Y_{lab} < 1.3$ as a function of $Q^2$ , $p_T^{*2}$ and $Y^*$ . The first uncertainty is statistical and the second is systematic. Overall normalisation uncertainties due to the luminosity measurement ( $\pm 2\%$ ) and to the $J/\psi$ decay branching ratio (1.7%) are not included in the systematic error. . . . .	144

- A.3 Differential cross sections and normalised differential cross sections in the kinematic region  $2 < Q^2 < 80 \text{ GeV}^2$ ,  $50 < W < 250 \text{ GeV}$ ,  $0.2 < z < 0.9$  and  $-1.6 < Y_{lab} < 1.3$  as a function of  $\log(M_X^2/\text{GeV}^2)$  and  $Y_X$ . The first uncertainty is statistical and the second is systematic. Overall normalisation uncertainties due to the luminosity measurement ( $\pm 2\%$ ) and to the  $J/\psi$  decay branching ratio (1.7%) are not included in the systematic error. . . . . 144
- A.4 Differential cross sections and normalised differential cross sections in the kinematic region  $2 < Q^2 < 100 \text{ GeV}^2$ ,  $50 < W < 225 \text{ GeV}$ ,  $0.3 < z < 0.9$  and  $p_T^{*2} > 1 \text{ GeV}^2$  as a function of  $z$ ,  $p_T^{*2}$  and  $Y^*$ . The first uncertainty is statistical and the second is systematic. Overall normalisation uncertainties due to the luminosity measurement ( $\pm 2\%$ ) and to the  $J/\psi$  decay branching ratio (1.7%) are not included in the systematic error. . . . . 145

# Chapter 1

## Introduction

The goal of high energy physics is the understanding of the fundamental interactions between the elementary constituents of matter. The *Standard Model* has provided over the last twenty years a satisfactory description of the strong, weak and electromagnetic interactions of all known elementary particles. In the numerous comparisons between experiment and theory only a few discrepancies have been found, and these are at the level of few standard deviations or less.

Given this success, one should expect that the description of a bound state of two reasonably heavy quarks, namely *Charmonium*, can be incorporated rather easily into the model.

Inelastic production of charmonium can be described in two steps. The first step is the creation of a  $c\bar{c}$  quark pair, a process which can be calculated in perturbative Quantum Chromodynamics (QCD). The second step is the formation of the  $J/\psi$  bound state, which occurs at long distances and is described by phenomenological models. When charmonium production was first investigated at CERN [1–3] and Fermilab [4] it was hoped that the production cross section could be used to determine the gluon density in the proton, because the gluon density directly enters the cross section calculation. This idea was encouraged by the qualitative agreement of the data with the predictions of LO QCD within the framework of the colour–singlet model (CSM) [5] in which the  $c\bar{c}$  pair is formed in a CS state identified with the  $J/\psi$ .

Later data from  $p\bar{p}$  collisions at Fermilab [6, 7] indicated that the CSM is not able to describe  $J/\psi$  production at large  $J/\psi$  transverse momenta, and hence that there may be significant contributions from higher orders in QCD or from the production of  $c\bar{c}$  pairs in colour–octet (CO) states, which evolve into  $J/\psi$  mesons via radiation of soft gluons.

Following these results in 1992, the calculations of the production of Charmonium states have been put on a formal basis by the work of Bowin, Braaten and Lepage. In the framework of non-relativistic QCD (NRQCD) [8] in which CS and CO contributions coexist. The transition of the coloured  $c\bar{c}$  pair, with a given angular momentum, into a  $J/\psi$  is described in terms of long-distance matrix elements tuned to experimental data (hadroproduction of  $J/\psi$  mesons or  $B$ -meson decays to  $J/\psi$ ). As well as describing high- $p_T$  charmonium production in  $p\bar{p}$  collisions [6, 7], NRQCD calculations including CS and CO contributions are also consistent with the data on production of  $J/\psi$  mesons in  $\gamma\gamma$  interactions at LEP2 [9]. However,  $J/\psi$  polarisation data from CDF [10] are inconsistent with NRQCD predictions. Comparisons with the decay angular distributions measured in  $e^+e^-$  collisions at BaBar [11] and Belle [12] are inconclusive. Cross sections and momentum spectra of  $J/\psi$  mesons measured by these collaborations can be described neither within the CSM nor within the NRQCD and hence indicate that there is a need to introduce additional resummation procedures important at phase space boundaries (soft gluon emission control) [13, 14].

Models in the framework of the semi-hard or  $k_T$ -factorisation approach [15–22] are also available. In these models, based on non-collinear parton dynamics governed by the BFKL [23–25] or CCFM [51, 52] evolution equations, effects of non-zero gluon transverse momentum are taken into account. Cross sections are then calculated as the convolution of unintegrated (transverse-momentum dependent) gluon densities and LO off-shell matrix elements. These models [28–30] succeed in describing the  $p_T$  spectra of different quarkonium states at Fermilab and  $J/\psi$  meson production at HERA, as well as the quarkonium polarisation properties measured both at Fermilab and HERA.

The production of  $J/\psi$  mesons in  $ep$  collisions at HERA is sensitive to both CS and CO contributions. The CS mechanism is expected to be the dominant contribution at intermediate values of the inelasticity variable,  $z \lesssim 0.7$ . In the proton rest frame,  $z$  is the fraction of the virtual photon energy transferred to the  $J/\psi$ . The CO mechanism is expected to be dominant at high  $z$ . However, large contributions from the elastic and diffractive proton-dissociative  $J/\psi$  production processes are also present at  $z \approx 1$ .

Inelastic  $J/\psi$  production at HERA was studied previously in the photoproduction regime (photon virtuality  $Q^2 \approx 0$ ) by the H1 [31] and ZEUS [32] collaborations. The leading-order (LO) NRQCD calculations and the next-to-leading-order (NLO) CSM predictions are both consistent with the data. Inelastic  $J/\psi$

production in the deep inelastic scattering (DIS) regime ( $Q^2 \gtrsim 1 \text{ GeV}^2$ ) has been studied by the H1 collaboration [33]. In this case, the LO NRQCD predictions overestimate the data, whereas the LO CSM expectations underestimate them. The shape of the differential cross sections are reasonably well reproduced by both models, except for the inelasticity distribution in the case of LO NRQCD and for the distribution of the  $J/\psi$  transverse-momentum squared in the photon-proton centre-of-mass system in the case of the LO CSM. NLO CSM predictions are not available in the DIS regime.

Thus, the applicability of nonrelativistic QCD to the inclusive production of Charmonium and the classification of octet contributions in the relative velocities of product quarks are still open problems. At the same time, the octet contributions are expected to be much smaller in the semi-hard approach than in the collinear approximation. However, theoretical results involve significant uncertainties associated with the behavior of unintegrated gluon distributions, the dependence of the coupling constant on the energy scale, higher order perturbative corrections, and nonperturbative effects.

The subject of this thesis is the analysis of inelastic Charmonium electroproduction at HERA collider, using data taken with the ZEUS experiment in the years 1996 to 2000. Electroproduction means here that  $Q^2$  is large enough for scattered electron to be detected in the main detector ( $Q^2 \gtrsim 1 \text{ GeV}^2$ ), as opposed to photoproduction ( $Q^2 \simeq 0$ ).

The reaction  $ep \rightarrow e J/\psi X$  is studied for  $Q^2 > 2 \text{ GeV}^2$  and results compared with NRQCD and models in the  $k_T$ -factorisation approach.

A study of the  $J/\psi$  production in a new type of interaction is a way to check the universality of the long-distance matrix elements and unintegrated gluon densities.

In general the production process at large  $Q^2$  has a number of interesting features. Due to the presence of the hard scale in the interaction theoretical predictions should be more accurate. Diffractive background as well as contributions from resolved photon processes are known to be suppressed at high  $Q^2$ . However, contributions coming from  $\psi'$  and  $B$  mesons with subsequent decay into  $J/\psi$  mesons can be sizable.

The measurements presented here are in a larger kinematic range than those previously published by H1. A measurement of the hadronic final state,  $X$ , is presented for the first time.

We performed a second or parallel analysis of the process to confirm our results.

To improve the existing measurements of heavy quark production, and more generally the tracking capabilities of the experiment, the ZEUS detector was equipped with Straw-Tube Tracker (STT). This detector will allow for improved studies of charm production in the forward direction. We developed the GEANT simulation and track reconstruction software for the STT. Studies of the STT performance with MC data and real data presented.

This thesis starts in **chapter two** by outlining some of the phenomenological background to the subjects under discussion. This begins with an introduction to deep inelastic scattering, and moves on to a discussion of Charmonium production within this regime. Different models for Charmonium production are discussed.

**Chapter three** consider the ZEUS experiment. An overview of the HERA collider and the ZEUS detector is given here.

The remaining chapters focus on the analysis of Charmonium production in the ZEUS experiment, using the leptonic decay channel  $J/\psi \rightarrow \mu^+\mu^-$ . Chapter 4-5 presents the analysis of inelastic Charmonium production in deep inelastic scattering from the trigger and event selection through to the results and study of systematic errors.

**Chapter four** specifically details the triggering and reconstruction of events. It moves on to introduce the analysis of  $J/\psi$  mesons themselves, and the cuts used to extract the signal. Furthermore a description of the Monte Carlo data sets which have been used for acceptance corrections is given.

In **chapter five**, the determination of the total and differential cross sections for inelastic  $J/\psi$  production and the determination of the corresponding systematic errors is described. Comparisons of the data to predictions from NRQCD and models in the  $k_T$ -factorisation approach are shown. The luminosity upgrade of the HERA collider and the ZEUS detector is presented in **chapter six**. In this chapter we describe the Straw-Tube Tracker (STT). Studies of the STT performance with MC simulation and real data as well as development of the STT tracking reconstruction presented here. A summary and outlook concludes the thesis in **chapter seven**.

# Chapter 2

## Phenomenology of Charmonium Production

Since its discovery in 1974, the  $J/\psi$  meson has provided a useful laboratory for quantitative tests of quantum chromodynamics (QCD) and, in particular, of the interplay of perturbative and nonperturbative phenomena.

A significant amount of theoretical work has been carried out in the last twenty years to understand Charmonium in the framework of QCD.

However, despite the recent theoretical and experimental developments the range of applicability of the different approaches is still subject to debate. In this chapter a brief introduction to Deep Inelastic Scattering and the kinematics used to describe the process are given. The expression for the cross section in terms of structure functions is introduced. The discussion then moves on to the form of these structure functions, and their evolution. The chapter finishes by description of most important models for inelastic Charmonium production.

### 2.1 Charmonium

In what was later to become the November Revolution of particle physics, two groups discovered in 1974 simultaneously the particle today known as the  $J/\psi$  meson. Aubert et al. [34] observed at Brookhaven an enhancement in the  $e^+e^-$  mass spectrum in the reaction

$$p \text{ Be} \rightarrow e^+e^- + X, \tag{2.1}$$

naming it “ $J$ ”, while the second group, Augustin et al. [35] measured the  $e^+e^-$  annihilation cross section

$$e^+e^- \rightarrow \text{hadrons} \quad (2.2)$$

at the SPEAR machine at SLAC and named the new particle “ $\psi$ ” (see Fig. 2.1) The discovery was awarded with the 1976 nobel prize in physics for Samuel C. C. Ting and Burton Richter. The mass of the  $J/\psi$  is most precisely

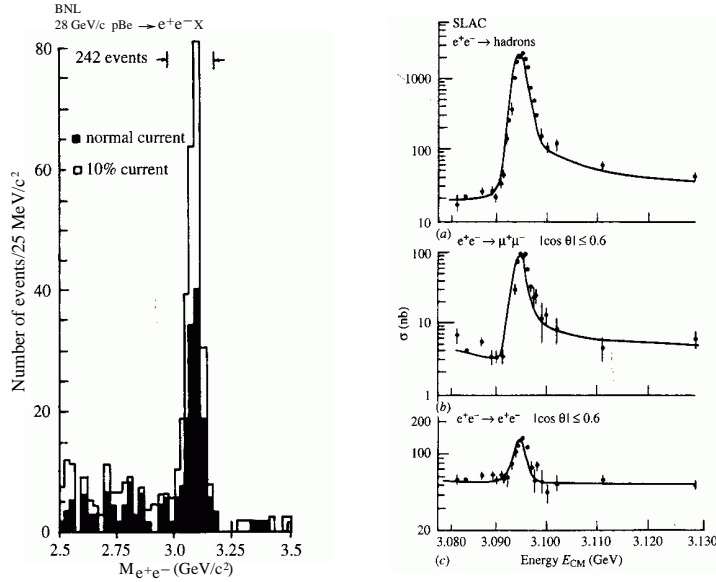


**Figure 2.1:** Discovery of the  $J/\psi$  at BNL and SLAC. On the left the invariant  $e^+e^-$  mass spectrum in the reaction  $p\text{Be} \rightarrow e^+e^- + X$  [34], on the right the energy dependence of the  $e^+e^-$  cross section [35].

determined using a depolarization method [36] that gives results one order of magnitude better than the direct mass determination in  $e^+e^-$  storage rings which is limited by the uncertainty of the absolute beam energy scale.

$$m_{J/\psi} = 3096.916 \pm 0.011 \text{ MeV}. \quad (2.3)$$

Since the  $J/\psi$  is produced in large numbers in  $e^+e^-$  annihilation, it is very plausible that it has the same quantum numbers as the photon,  $J^{PC} = 1^{--}$ . It turns out that the  $J/\psi$  is the lightest vector meson in the *Charmonium* family (see Fig. 2.2) that is interpreted as consisting of bound states of a

*charm* and *anti-charm* quark. The only lighter  $c\bar{c}$  meson is the pseudoscalar ( $J^{PC} = 0^{-+}$ )  $\eta_c$  with mass  $m_{\eta_c} \simeq 2.98$  GeV. The first radial excitation of the  $J/\psi$ , the  $\psi(2S)$ , has a mass of [37]

$$m_{\psi(2S)} = 3686.00 \pm 0.09 \text{ MeV}. \quad (2.4)$$

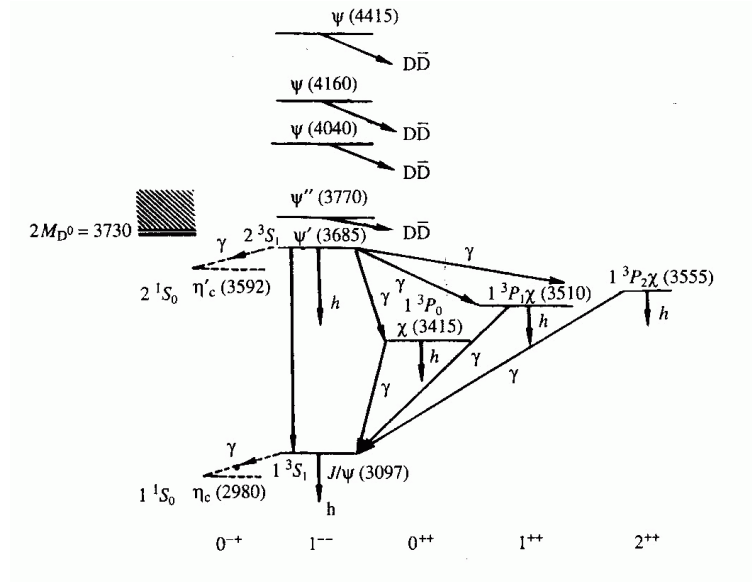


**Figure 2.2:** Level diagram of the Charmonium family [109]

The most interesting property of the  $J/\psi$  and the  $\psi(2S)$  mesons is their extremely small width [37]:

$$\Gamma_{J/\psi} = 87 \pm 5 \text{ keV}. \quad (2.5)$$

$$\Gamma_{\psi} = 277 \pm 31 \text{ keV}. \quad (2.6)$$

This is about three orders of magnitude below that of typical hadronic decays. The reason for this is that the  $J/\psi$  has very few options for decaying via the strong force. The most obvious decay mode would be the decay into two charmed mesons ( $D$  mesons) – but both the  $J/\psi$  and the  $\psi(2S)$  have masses below the threshold of  $\bar{D}D$  production,<sup>1</sup> since the mass of the lightest  $D$  meson, the  $D^0$ , is  $m_{D^0} \simeq 1.86$  GeV. Other hadronic decays can only proceed via diagrams which

<sup>1</sup>All Charmonium states above the  $\psi(2S)$  can decay in charmed mesons, resulting in a much larger width.

are forbidden by the OZI rule [38], and thus strongly suppressed.<sup>2</sup> In addition, the decays via a single gluon and via two gluons are not possible due to color and  $C$ -parity conservation, such that at least three gluons are needed for the hadronic decay of the  $J/\psi$  (see Fig. 2.3a)

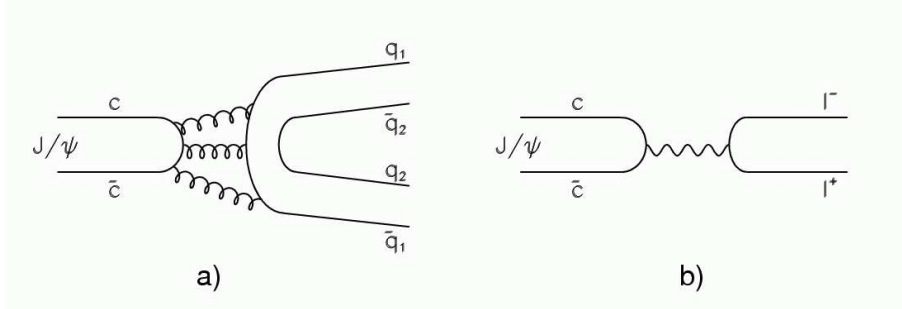


**Figure 2.3:** Diagrams for the a) strong decay of the  $J/\psi$  into two mesons consisting of light quarks  $q_1, q_2$  and b) the electromagnetic decay into two leptons  $l^+, l^-$

Of importance for this thesis is the electromagnetic decay of the  $J/\psi$  meson (Fig. 2.3b), with rather large branching fractions due to above reasons. Lepton universality implies almost identical branching ratios for decay into  $\mu^+\mu^-$  and  $e^+e^-$ ; the measured values are [109]

$$BR(J/\psi \rightarrow \mu^+\mu^-) = (5.88 \pm 0.11) \% ; \quad (2.7)$$

$$BR(J/\psi \rightarrow e^+e^-) = (5.93 \pm 0.10) \% ; \quad (2.8)$$

This analysis only analyses the muon channel.

## 2.2 Deep Inelastic Scattering

Deep Inelastic Scattering (DIS) is the scattering of a lepton off a hadron, through the exchange of a virtual vector boson, a  $\gamma^0$  or  $Z^0$ , or via the exchange of a virtual  $W^\pm$  boson. In the case of HERA, the lepton is an electron or positron, and the hadron a proton. The lepton can be considered as being a probe of the proton. Hence the processes of interest are

$$e^\pm p \rightarrow e^\pm X \quad (2.9)$$

<sup>2</sup>The OZI rule states that diagrams containing disconnected quark lines are suppressed relative to those with connected ones.

for the Neutral Current (NC) exchange of a  $\gamma^0$  or  $Z^0$ , and

$$e^\pm p \rightarrow \nu(\bar{\nu})X \quad (2.10)$$

for the Charged Current (CC) exchange of a  $W^\pm$ . These two types of exchanges are shown in figure 2.4.

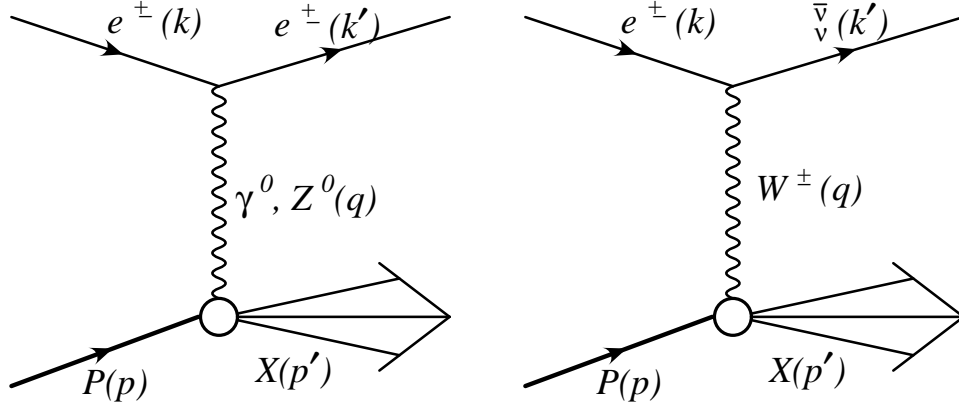


**Figure 2.4:** Neutral Current (*left*) and Charged Current (*right*) DIS.

The CC and NC cross sections become approximately equal with high virtuality of the exchanged boson - above the  $Z^0$  and  $W^\pm$  masses. However, where the exchanged boson has relatively low virtuality ( $\leq 100 \text{ GeV}^2$ ), which is the region of phase space which dominates the cross section, both the  $Z^0$  and  $W^\pm$  exchanges are suppressed by their large masses. As this is the area of phase space examined in this thesis, only the exchange of the  $\gamma^0$  is considered.

## 2.3 DIS Kinematics

In figure 2.5 a representation of a NC interaction via  $\gamma$  exchange is shown. The four-momenta of the incoming ( $e$ ) and outgoing lepton ( $e$  or  $\nu_e$ ) are  $k = (E_e; \vec{k})$  and  $k' = (E_{e'}; \vec{k}')$ , and those of the incoming proton ( $P$ ) and the hadronic final state ( $X$ )  $p = (E_p; \vec{p})$  and  $p' = (E_{p'}; \vec{p}')$ .

The centre of mass energy squared of the  $ep$  collisions,  $s$ , is

$$s = (k + p)^2 \approx 4E_e E_p \quad (2.11)$$

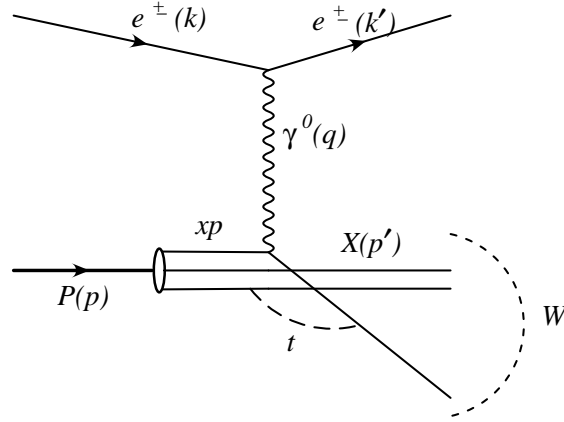


**Figure 2.5:** Kinematics of Neutral Current DIS.

The spacelike virtuality of the exchanged photon,  $Q^2$  is

$$Q^2 = -q^2 = -(k - k')^2 \quad (2.12)$$

and ranges from 0 to  $s$ . The smallest size that the photon can resolve depends upon its wavelength,  $\lambda \approx \hbar c / \sqrt{Q^2}$ , so as  $Q^2$  increases, the structure of the proton is probed at a finer scale.

It is useful to define two dimensionless Lorentz invariant quantities,  $x$  and  $y$ . These quantities range from 0 to 1. The Bjorken variable  $x$  is defined as

$$x = \frac{Q^2}{2p \cdot q} \quad (2.13)$$

and is equal to the momentum fraction carried by the struck parton in the Leading Order<sup>3</sup> parton model.

$y$  is a measure of the amount of energy transferred between the lepton and hadron systems, and is defined by:

$$y = \frac{p \cdot q}{p \cdot k} \quad (2.14)$$

<sup>3</sup>Throughout this thesis, *Leading Order* is often denoted by LO, and similarly *Next-to-leading Order* by NLO.

The centre of mass energy of the hadronic ( $\gamma^*p$ ) system is given by:

$$W^2 = (p')^2 = (p + q)^2 \quad (2.15)$$

which can be approximated, assuming that the proton and lepton masses can be ignored, by

$$W^2 = Q^2 \left( \frac{1}{x} - 1 \right) = sy - Q^2 \quad (2.16)$$

Only two of the three variables  $x$ ,  $y$ , and  $Q^2$  are independent, and all three are related by

$$Q^2 = -(k - k')^2 = -q^2 = sxy \quad (2.17)$$

assuming that the proton and lepton masses are negligible.

A powerful variable in discriminating different  $J/\psi$  production mechanisms is the Lorenz invariant

$$z := \frac{p_\psi \cdot p}{q \cdot p} \quad (2.18)$$

where  $p_\psi$ ,  $q$  and  $p$  denote the four-momenta of the  $J/\psi$ , the exchanged photon and the incoming proton.

HERA processes are distinguished by the virtuality of the exchanged boson  $Q^2$  and the invariant mass of the virtual photon-proton system  $W^2$ . An interaction where the boson virtuality is larger than the proton mass ( $Q^2 \gg M_p^2$ ) is denoted as *deep* and an interaction where the invariant mass of the virtual photon-proton system is larger than the proton mass ( $W^2 \gg M_p^2$ ) is denoted as *inelastic*, an interaction with both  $Q^2 \gg M_p^2$  and  $W^2 \gg M_p^2$  therefore *deep inelastic scattering* (DIS) in the case of the exchange of a  $\gamma$ ,  $Z_0$  or  $W^\pm$  boson. The case of a quasi-real exchanged boson which can only be a photon due to the available energy content of the exchange is named *photoproduction* (PHP).

## 2.4 Structure Functions

The DIS cross section can be expressed in terms of  $F_1$ ,  $F_2$  and  $F_3$ , which are the proton structure functions. The double differential cross section for  $e^+p$  NC DIS

scattering <sup>4</sup> in terms of the structure functions  $F_1$ ,  $F_2$  and  $F_3$  is

$$\frac{d^2\sigma}{dx dQ^2} = \frac{4\pi\alpha^2}{xQ^4} \left( \frac{y^2}{2} 2xF_1(x, Q^2) + (1-y)F_2(x, Q^2) - \left(y - \frac{y^2}{2}\right)x F_3(x, Q^2) \right) \quad (2.19)$$

where  $\alpha = \alpha_{em} \sim \frac{1}{137}$ . These structure functions cannot be calculated in perturbative QCD, but must be derived from experimental results.

Using the relation

$$F_L = F_2 - 2xF_1 \quad (2.20)$$

the expression for the NC DIS cross section reduces to

$$\frac{d^2\sigma}{dx dQ^2} = \frac{2\pi\alpha^2}{xQ^4} [Y_+ F_2(x, Q^2) - y^2 F_L(x, Q^2) - Y_- x F_3(x, Q^2)] \quad (2.21)$$

where the helicity dependence of the electroweak interactions is contained within

$$Y_{\pm} = 1 \pm (1-y)^2 \quad (2.22)$$

$F_2$  is the generalised structure function of  $\gamma$  and  $Z^0$  exchange, and  $F_L$  is the longitudinal structure function.

$F_3$  is the parity-violating contribution coming from both, the pure exchange of the massive propagator  $Z^0$  and from the quantum mechanical interference between  $\gamma - Z$ , and is small for  $Q^2 \ll M_Z^2$ . It is important at large  $x$  and  $Q^2$ , where it substantially reduces (increases) the  $e^+p$  ( $e^-p$ ) cross section. A detailed derivation of all these terms is given, for example in [39].

## 2.5 Quark Parton Model

The Quark Parton Model (QPM) describes DIS as the incoherent sum of elastic scattering processes of the lepton from effectively point-like constituents within the proton. In this model, the DIS process is described as the quasi-elastic scattering of the exchanged gauge boson off a single quark in the proton. In QPM, the Bjorken scaling variable,  $x$ , represents the fraction of the proton's momentum carried by the struck quark. If the quarks are assumed to be non-interacting, free particles within the proton, then the structure functions can be

---

<sup>4</sup>For  $e^-p$  NC DIS scattering, the sign of the last term in equation 2.19 and 2.21 changes.

expected to be a function of  $x$  but not of  $Q^2$ , since changes in  $Q^2$  correspond to changes in the scale probed by the exchanged boson, which will be irrelevant for point-like constituents; i.e.  $F_i(x, Q^2) = F_i(x)$ . This behavior, originally proposed by Bjorken in the limit  $Q^2 \rightarrow \infty$  and finite  $x$ , is known as *scale invariance*.

In the QPM, the structure function  $F_2$  can be expressed in terms of the parton density functions  $f_i$  as

$$F_2(x) = x \sum_i e_i^2 f_i(x) , \quad (2.23)$$

where  $e_i$  is the charge of parton  $i$  and  $f_i(x)dx$  is the probability of finding a parton of type  $i$  in the momentum range between  $x$  and  $x + dx$ . For point like spin- $\frac{1}{2}$  Dirac particles the Callan-Gross relation [40],

$$F_2(x) = 2xF_1(x) \quad \Rightarrow \quad F_L = 0 , \quad (2.24)$$

holds. Furthermore, experiments show that [41]

$$\sum_i \int_0^1 x f_i(x) dx \approx 0.5 , \quad (2.25)$$

implying that only half of the proton's momentum is carried by charged quarks. The other half is carried by neutral partons which are identified with gluons. Direct experimental evidence for the existence of gluons was found in 1979 at DESY via the observation of three-jet events in  $e^+e^-$  annihilation [42].

## 2.6 Quantum Chromodynamics

The QPM, as described in the previous section, has been quite successful in kinematic regions where the effects of gluons can be neglected. However, the QPM is not enough to describe the effects observed at HERA. In this kinematic region, the QPM needs to be modified in order to include coupling of quarks to gluons - as required by QCD.

Quantum Chromodynamics (QCD) is a field theory developed in the 1970's to describe the strong interaction between quarks. It is a non-abelian gauge theory based on the SU(3) symmetry group. Quarks carry one of three possible 'color charges' (red (r), green (g) or blue (b)). As a consequence of the non-abelian structure the mediating gauge bosons in QCD called gluons also carry color charge and thus couple to each other.

In contrast to QED the QCD coupling constant  $\alpha_S$  increases at large distances (low  $Q^2$ ) and is small at small distances (large  $Q^2$ ), which is known as asymptotic freedom. The scale dependence in leading order perturbation theory is given by [43]

$$\alpha_S(Q^2) = \frac{12\pi}{(33 - 2n_f) \ln(Q^2/\Lambda^2)}, \quad (2.26)$$

where  $n_f$  is the number of active quark flavors. The QCD scale parameter  $\Lambda$  determines the energy scale at which  $\alpha_S$  becomes small and has been measured to be (100 - 300) MeV. At large  $Q^2$  values  $\alpha_S$  decreases logarithmically and when  $\Lambda^2 \ll Q^2$  perturbative QCD (pQCD) can be applied. In QCD the naive QPM model as described in the previous section needs to be modified due to the coupling of quarks to gluons. This means that quarks can radiate gluons which in turn can split into  $q\bar{q}$ -pairs. (Such quarks are called “sea” quarks). In such a case, the number of partons increases while the average momentum per parton decreases. With increasing  $Q^2$ , more and more of these fluctuations can be resolved.

In the low  $Q^2$  region the valence quarks which have relatively large  $x$  values dominate. At large  $Q^2$  values gluon radiation leads to an increase in the number of quarks with low  $x$  values and correspondingly to a depletion of the high  $x$  region. In fact, at low  $x$  a rapid increase of  $F_2$  with increasing  $Q^2$  has been observed [44, 45] while  $F_2$  decreases at large values of  $x$ . This logarithmic  $Q^2$  dependence of  $F_2$  for fixed  $x$  is known as scaling violations.

Gluon radiation also results in a transverse momentum component of the quarks which can consequently couple to longitudinally polarized photons. The Callan-Gross relation is thus no longer satisfied exactly and  $F_L$  is different from zero.

## 2.7 QCD factorization and parton densities

The distribution of partons in hadrons cannot be calculated from first principles within perturbation theory. However, the *factorization* theorem of QCD allows the separation of the non-perturbative long-range contribution (soft process) from the short-range contribution (hard process) which is calculable in perturbative QCD:

$$\sigma_{ep}(x, Q^2) = \sum_{i \in \text{partons}} f_{i/p}(x, \mu_F^2) \otimes \sigma_{ei}(x, Q^2, \mu_F^2). \quad (2.27)$$

The parton density functions (PDFs),  $f_{i/p}$ , give the probability of finding a quark,  $q$ , with momentum fraction  $x$  at a given  $Q^2$ , and the  $\sigma_{ei}$  are the hard-scattering cross sections describing the short-range interactions. The PDFs have to be determined by global fits to measured experimental data sets. The factorization scale,  $\mu_F$ , defines the scale at which the gluon radiation is absorbed into the PDFs or into the hard scattering cross section, hence it determines the line of separation between what is considered to be the long-range inner dynamics of the proton ( $f_{i/p}$ ) and the dynamics of the hard lepton-parton interaction ( $\sigma_{ei}$ ). Since  $\sigma_{ei}(\mu_F^2)$  can be calculated perturbatively in QCD for any scale and the physical observable  $\sigma_{ei}$  must be independent of the arbitrarily chosen scale  $\mu_F^2$  the change of the PDFs with changing scale can also be calculated. This leads to the so called evolution equations. In the perturbative calculation of  $\sigma_{ei}$  approximations have to be applied which are valid in certain regions of  $x$  and  $Q^2$ .

## 2.8 Parton Evolution

The idea of parton evolution is needed to describe the variation of the structure function with  $Q^2$ . The essential idea here is that the parton being probed may not be the original constituent of the proton. The quark or gluon probed may radiate another parton before the interaction with the photon.

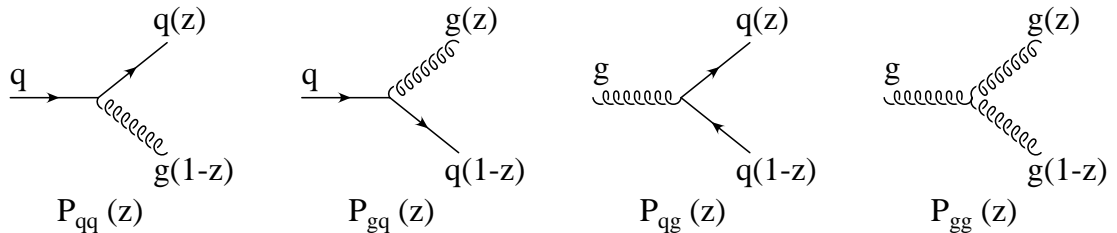


**Figure 2.6:** Altarelli-Parisi splitting functions.

The Altarelli-Parisi splitting functions [46],  $\mathcal{P}_{ij}(z)$  give the probability of a parton  $j$  emitting parton  $i$  which carries momentum fraction  $z$  of the original parton. At leading order there are 4 splitting functions. These correspond to gluon radiation from the quark,  $q \rightarrow qg$ , to a quark and a gluon,  $q \rightarrow gp$ , a gluon splitting to a quark-antiquark pair,  $g \rightarrow q\bar{q}$ , and a gluon splitting into two gluons,

$g \rightarrow gg$ . The four splitting functions are illustrated in figure 2.6, and are given at leading order by,

$$\mathcal{P}_{qq}^0(z) = \frac{4}{3} \frac{1+z^2}{1-z} \quad (2.28)$$

$$\mathcal{P}_{qg}^0(z) = \frac{1}{2} (z^2 + (1-z^2)^2) \quad (2.29)$$

$$\mathcal{P}_{gq}^0(z) = \frac{4}{3} \frac{1+(1-z)^2}{z} \quad (2.30)$$

$$\mathcal{P}_{gg}^0(z) = 6 \left( \frac{z}{1-z} + \frac{1-z}{z} + z(1-z) \right) \quad (2.31)$$

### 2.8.1 DGLAP evolution

The evolution of both the quark and gluon densities with  $Q^2$  can be expressed in terms of splitting functions, within the DGLAP equations [46]. In the context of pQCD, two types of terms can become large, and hence dominant in the perturbative series - those in  $\ln Q^2$ , and those in  $\ln \frac{1}{x}$ . Terms of the form  $(\alpha_s \ln Q^2)^n$  are formally first order in any perturbative expansion as can be seen from equation 2.26, and therefore need to be resummed to ensure the convergence of the perturbative series. Therefore, the derivation of the DGLAP equation uses the Leading Log Approximation (LLA), where the terms  $(\alpha_s \ln Q^2)^n$  are resummed. These terms give the dominant contributions at large  $Q^2$  and large  $x$  only, as terms of the form  $\ln \frac{1}{x}$  are neglected, unless they are accompanied by a large  $\ln Q^2$  term. A more detailed discussion of the derivations of these equations is given in [47]. The quark distributions functions evolve via gluon radiation from quarks and by gluon splitting, where the original gluon splits into a  $q\bar{q}$  pair, i.e.

$$\frac{dq_i(x, Q^2)}{d \ln(Q^2)} = \frac{\alpha_s(Q^2)}{2\pi} \int_x^1 \frac{dy}{y} \left[ \sum_j q_j(y, Q^2) P_{q_i q_j} \left( \frac{x}{y} \right) + g(y, Q^2) P_{q_i g} \left( \frac{x}{y} \right) \right] \quad (2.32)$$

Similarly, the evolution of the gluon distribution functions is given by

$$\frac{dg_i(x, Q^2)}{d \ln(Q^2)} = \frac{\alpha_s(Q^2)}{2\pi} \int_x^1 \frac{dy}{y} \left[ \sum_j q_j(y, Q^2) P_{g q_j} \left( \frac{x}{y} \right) + g(y, Q^2) P_{g g} \left( \frac{x}{y} \right) \right] \quad (2.33)$$

where the first term describes a gluon being the parton within a quark, and the second where a gluon splits into two gluons.

In equation 2.32 and 2.33,  $yp$  is the fractional momentum of the parton extracted from the proton,  $xp$  the fractional momentum of the parton which

interacts with the photon, which means that  $(y-x)p$  is the fractional momentum of the radiated parton, and  $xp+q$  the momentum of the scattered parton in the final state.

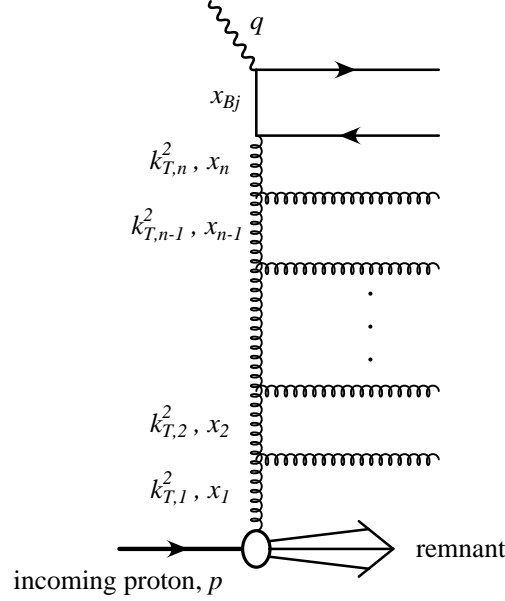


**Figure 2.7:** Gluon ladder showing the effect of several gluons radiated from the parton which interacts with the virtual photon.

The overall effect of several emissions is shown in figure 2.7, and is to increase the density of low  $x$  partons. The cross section of the DIS process is given by summing all the ladder gluons of the consecutive gluon emissions - i.e. summing over all diagrams with 0 to  $\infty$  gluon emissions. The consecutive gluon emissions are ordered in both longitudinal momentum, and in transverse momentum,  $k_T$ . If the rungs are numbered from 1 (nearest to the proton), to  $n$  (nearest to the photon), then the fraction of longitudinal momentum  $x_i$  carried by the emitted gluons is ordered such that,

$$x_1 > x_2 > \dots > x_n \quad (2.34)$$

At the same time, the transverse momenta of the emitted gluons,  $k_{T,i}$ , increases strongly going up the ladder,

$$k_{T,1}^2 \ll k_{T,2}^2 \ll \dots \ll k_{T,n}^2 \ll Q^2 \quad (2.35)$$

The solutions of the DGLAP equations give the parton distributions as a function of  $x$  at any scale  $Q^2$ , provided their  $x$  dependence at an input scale  $Q_0^2$  is known. The parton densities at  $Q_0^2$  are determined from experiment as they are not predicted by the perturbation theory.

### 2.8.2 BFKL evolution and $k_T$ factorization

The DGLAP equations, as discussed above, are expected to fail at very low  $x$  (or at high center-of-mass energies of the virtual photon-proton system), as they only describe strongly ordered ladder diagrams, and neglect terms of the form  $\ln \frac{1}{x}$  which may become large as  $x$  becomes small. Summation of such contributions leads to unintegrated gluon distributions (dependent of the transverse momentum  $k_T$ ), which obey the Balitsky-Fadin-Kuraev-Lipatov(BFKL) equation [48]. In the framework of the unintegrated gluon distribution, predictions for the measured cross sections are calculated using the  $k_T$ -factorization theorem [49]. Cross sections are factorized into an off-shell ( $k_T$  dependant) partonic cross section and a  $k_T$ -unintegrated parton distribution.

$$\sigma = \int \frac{d\xi}{\xi} dk_T^2 \hat{\sigma} \left( \frac{x}{\xi}, k_T^2 \right) f(\xi, k_T^2) \quad (2.36)$$

In the  $k_T$ -factorization the partons entering the hard scattering matrix element are free to be off-shell, in contrast to the collinear approach which treat all incoming partons as massless. This has some additional advantages. In the conventional approach a process with an additional gluon in the final state, in which the transverse momentum of the gluon is of the order of that of the quarks, requires the calculation of the full NLO matrix element. Using the  $k_T$ -factorization such processes are naturally included to the leading logarithmic accuracy, since  $k_T$  of the incoming gluon is only restricted by kinematics and therefore can acquire a virtuality similar to the ones in a complete fixed order calculation [50]. In relation to what is obtained in the standard parton model (that is, collinear approach), the calculation of the cross sections within the  $k_T$ -factorization approach leads to a number of observable effects – such as the broadening of transverse-momentum spectra and to characteristic polarization properties of charmonium, this being due to the fact that the primary gluon is off the mass shell [28–30].

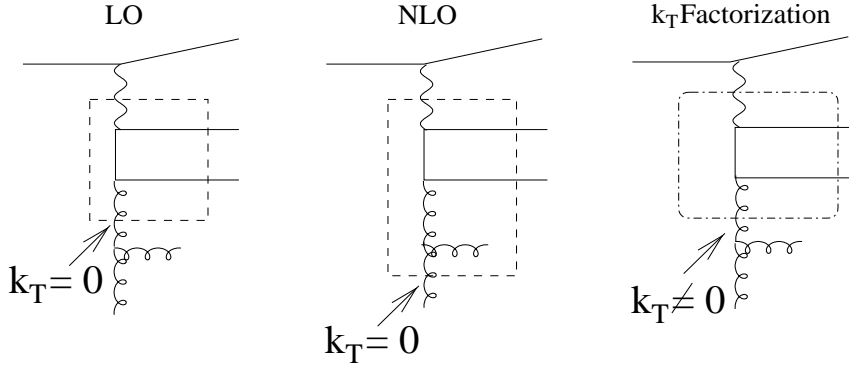


**Figure 2.8:** BGF diagrams at the leading (left), next-to-leading order (center) and in the  $k_T$ -factorization (right). In the latter case, the gluon entering the hard process (dot-dashed box) is free to be off-shell

### 2.8.3 CCFM equation

Both the DGLAP and the BFKL methods only sum over one particular leading behavior of the evolution problem to obtain their results. A complete (infinite order) calculation should take both the terms in  $\ln(Q^2)$  and  $\ln(1/x)$  and sum over them. To accomplish this, Ciafaloni [51] and Catani, Fiorani and Marchesini [52] introduced angular ordering for the emitted gluons. The maximum allowed angle is defined by the hard scattering, where the quark pair is produced. This is combined with the unintegrated gluon densities and off-shell partons, like in BFKL. This method seems very promising, as it can (approximately) reproduce the DGLAP and BFKL equations when taking the appropriate limits. These evolution also allow a reformulation in a form suitable for implementation in a Monte Carlo program like CASCADE [110]

## 2.9 Charm Production in DIS

The study of charm production in DIS is partly motivated from the expectation that it is calculable in perturbative QCD (pQCD). This arises since

$$m_c \gg \Lambda_{QCD} \quad (2.37)$$

and therefore there is always a hard scale available in charm production, allowing pQCD calculations. The perturbative nature of charm production makes charm

in DIS a good test of the perturbative description of DIS. Charm production also has the potential to constrain parton densities in the small  $x$  region, where the gluon and sea parton densities are expected to be dominant, although this is however hampered by the poorly known value of the charm mass.

### 2.9.1 Boson-Gluon-Fusion

Heavy quark production at HERA is dominated by gluon driven production. In particular, the main production mechanism is Boson-Gluon Fusion (BGF), where a gluon from the proton couples to the photon, at leading order, by the gluon splitting to a  $c\bar{c}$  pair. Figure 2.9 shows a diagram of the leading order BGF process. The model of charm production being dominated by BGF gives a good description of the previous measurements of charm at HERA [53].

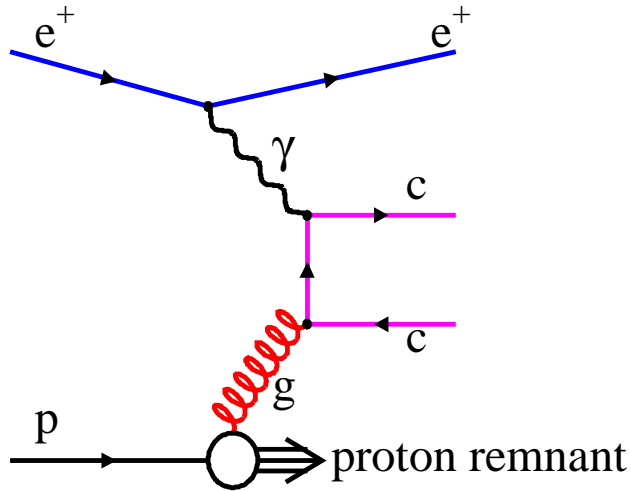


**Figure 2.9:** Boson Gluon Fusion in DIS.

As charm production in DIS is mostly driven by the gluon, measuring charm gives a direct handle on the gluon density in the proton, which is at present a poorly measured quantity. Although there have been measurements of the gluon density using charm production from HERA data [54], it is a non-trivial process. The large uncertainty in the cross section due to the charm mass, especially in the low  $Q^2$  region, where charm production is especially sensitive to the gluon density,

means that the extraction of the gluon density from inclusive measurements of charm production is problematic.

## 2.10 Inelastic Charmonium production in DIS

In the present section, the three main models for inelastic Charmonium production will be presented in their historical order. In all models, the production of the  $c\bar{c}$  pair is treated separately from its evolution into a bound state (factorization); factorization is considered to be legitimate because the production of the  $c\bar{c}$  pair proceeds on a short time scale of order  $1/m_c$ , while the formation of the bound state is a non-perturbative long distance process on a time scale longer than  $1/\Lambda_{QCD}$ . The dominant process by which heavy quark pairs are produced at HERA is the photon gluon fusion graph (depicted in figure 2.9), but all models are equally well applicable to other processes, e.g. hadroproduction of Charmonium via gluon gluon fusion.

### 2.10.1 The Color Evaporation Model

The Color Evaporation Model – also referred to as the “local duality approach” – has been developed in the late seventies by Fritzsche et al. [55–57]. In this approach, the sum of the cross sections of all  $c\bar{c}$  bound states is given by the integral of the cross section for  $c\bar{c}$  production,  $\sigma_{c\bar{c}}$ , from the lower threshold  $2m_c$  up to the threshold for the production of a pair of heavy–light mesons,  $2m_D$ :

$$\sigma_{onium} = \frac{1}{9} \int_{2m_c}^{2m_D} dm \frac{d\sigma_{c\bar{c}}}{dm} \quad (2.38)$$

where  $\sigma_{c\bar{c}}$  is calculated in perturbation theory. The factor  $1/9$  represents the statistical probability for the quark pair to be asymptotically in the color singlet state. This transition is thought to proceed via multiple soft–gluon interactions, implying a statistical treatment of colour. Due to the multiple soft–gluon exchanges, Charmonium produced via the colour evaporation mechanism is predicted to be unpolarized [58], which is a very distinct feature compared to other models for inelastic Charmonium production.

To obtain the cross section for a specific Charmonium state such as  $J/\psi$ , the factor  $\rho_\psi$  is introduced:

$$\sigma_\psi = \rho_\psi \times \sigma_{onium} \quad (2.39)$$

The factor  $\rho_\psi$  is of the order of  $1/N_{onium}$ , where  $N_{onium}$  is the number of Charmonium states with mass between  $2m_c$  and  $2m_D$ . Since  $\rho_\psi$  can depend on the specific state, the production process, the centre of mass energy, the transverse momentum of the Charmonium,  $m_c$  and the gluon density in the target(s), absolute predictions in the Color Evaporation Model are difficult. A comparison to the recent experimental data is given in [58]. Although qualitative agreement with the data is observed, the Color Evaporation Model receives rather little interest in the literature due to its weak predictive power.

### 2.10.2 The Color Singlet Model

The Color Singlet Model (CSM) [5], developed since 1980, was the first to provide quantitative predictions for Charmonium production in a wide variety of environments: in hadron collisions, photoproduction and  $e^+e^-$  collisions. The  $J/\psi$  production is thought to proceed in two steps: in the first step, a  $c\bar{c}$  pair with the same quantum numbers – spin, angular momentum and C-parity – as Charmonium state is produced in a colour singlet state; the second step contains the binding of the  $c\bar{c}$  into Charmonium state. The cross section can then be factorized into a short distance matrix element describing the  $c\bar{c}$  production in a region of size  $1/m_c$ , and a long distance factor that describes the non-perturbative dynamics of the bound state formation. The differential cross section for e.g.  $\gamma p \rightarrow J/\psi X$  can be written as

$$d\sigma(J/\psi + X) = d\hat{\sigma}(c\bar{c}(\underline{1}, S_1) + X) |R_\psi(0)|^2, \quad (2.40)$$

where  $R_\psi(0)$  is the  $J/\psi$  wave function at the origin, and the notation “ $\underline{1}$ ” is used to denote that  $c\bar{c}$  pair is in colour singlet state.

The short distance part  $d\hat{\sigma}$  can be calculated using a perturbative expansion in  $\alpha_s(m_c)$ , while the long distance part is related to the electronic width  $\Gamma_{ee}$  of the Charmonium:

$$\Gamma(J/\psi + X) \simeq \frac{4\alpha^2}{9m_c^2} |R_\psi(0)|^2 \quad (\text{leading order}). \quad (2.41)$$

Applied to  $J/\psi$  production at HERA, the leading contribution in the photon gluon fusion process is of order  $(\alpha, \alpha_s^2)$  since at least one additional gluon is needed to produce a  $c\bar{c}$  pair with the quantum numbers of the  $J/\psi$  (see fig. 2.10.2). In order to ensure the applicability of the perturbative expansion, the additional gluon has to be hard.

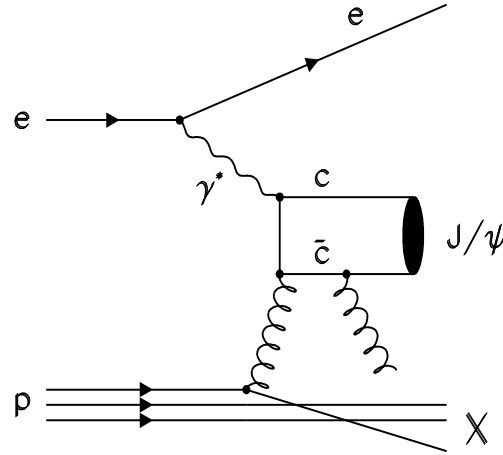


**Figure 2.10:** A leading order graph for  $J/\psi$  production in the Colour Singlet Model.

### 2.10.3 Non-relativistic QCD factorization method

The approach discussed here was first applied for the prediction of decay rates of  $P$ -wave Charmonium states by Bodwin, Braaten and Lepage (BBL) [59]. It was later developed into a complete theory [8], and received much attention due to the ability to describe the large production rates for high  $p_t$  hadroproduction of  $J/\psi$  at the Tevatron [60]. In the BBL formalism, the production cross section for Charmonium states, e.g.  $A + B \rightarrow J/\psi + X$ , can be expressed as

$$\sigma(J/\psi + X) = \sum_n c_n(A + B \rightarrow c\bar{c} + X) \langle 0 | O_n^{J/\psi} | 0 \rangle, \quad (2.42)$$

where  $n$  denotes an on-shell  $c\bar{c}$  pair in a definite colour, spin and angular momentum state. For each  $n$ , the cross section factorizes into a short distance part  $c_n$  calculable in a perturbative QCD expansion in  $\alpha_s(m_c)$  and a long distance matrix element  $\langle O_n^{J/\psi} \rangle$  giving the probability for the  $c\bar{c}$  pair to form a  $J/\psi$  meson. The  $\langle O_n^{J/\psi} \rangle$  describe the evolution of the  $c\bar{c}$  pair into a  $J/\psi$  plus additional soft gluons. While in the Colour Singlet Model all  $c_n$  not corresponding to a colour singlet  $c\bar{c}$  are set to zero, the BBL formalism includes states where the  $c\bar{c}$  system is a colour octet.

The major ingredient in the theory besides factorization is the introduction of non-relativistic QCD (NRQCD [61]) velocity scaling rules that make the application of equation 2.42 possible. NRQCD is an effective field theory in which the heavy quark and antiquark are treated non-relativistically. At first sight, the equation 2.42 is not particularly useful since it involves an infinite number of non-perturbative factors  $\langle O_n^{J/\psi} \rangle$ . However, it can be deduced from NRQCD that the matrix elements  $\langle O_n^{J/\psi} \rangle$  scale with powers of the square of the typical velocity  $v$  of the heavy quark in the Charmonium state. If  $v^2$  is a small quantity – and this is indeed the case, with  $v^2 \simeq 0.3$  for the  $J/\psi$  – the Charmonium production cross section can be calculated to arbitrary precision with a double expansion in powers of  $\alpha_s(2m_c)$  and  $v^2$ .

Note that in the limit  $v \rightarrow 0$  the Colour Singlet Model is restored. Colour octet contributions are suppressed by powers of  $v^2$ , and can only become important when the corresponding short distance coefficients  $c_n$  for colour octet states are larger.

An important property of the matrix elements, which greatly increases the predictive power of NRQCD, is the fact that they are universal, i.e., process independent.

The proof of the factorization formula in Eq.(2.42) relies both on NRQCD and on the all-orders perturbative machinery for proving hard-scattering factorization. A detailed proof does not yet exist, but work is in progress. At a small transverse momentum  $p_t$  of order  $m_c v$  or smaller, the presence of soft gluons in the Charmonium binding process makes the application of the standard factorization techniques problematic.

Inelastic lepton production of  $J/\psi$  mesons at HERA is dominated by virtual-photon-gluon fusion. At high  $Q^2$ , theoretical uncertainties in the models decrease. The cross section for  $J/\psi$  production in deep-inelastic  $ep$  scattering at HERA was calculated in the NRQCD factorization approach at leading order in  $\alpha_s$  by Kniehl and Zwirner [131], taking into account diagrams shown in figure 2.10.3

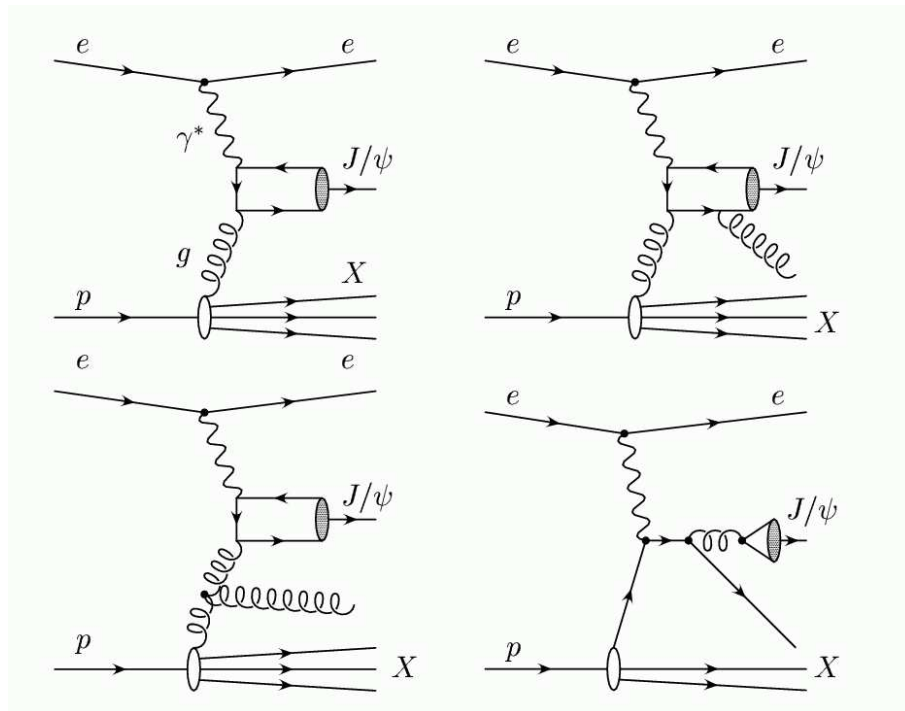


**Figure 2.11:** Generic diagrams of Charmonium production mechanisms: photon–gluon fusion via a “ $2 \rightarrow 1$ ” process (top left) and “ $2 \rightarrow 2$ ” processes (remaining diagrams). All the diagrams contribute via color–octet mechanisms, while the top right diagram can also contribute via color–singlet mechanism. Additional soft gluons emitted during the hadronizations process are not shown.



# Chapter 3

## The ZEUS detector at HERA

This chapter gives a brief introduction to the HERA collider and the ZEUS experiment. Detector components relevant for this analysis are described in more detail. A detailed description of the ZEUS detector can be found in [62].

### 3.1 The HERA collider

HERA (Hadron Electron Ring Anlage) [63] is the only high energy elementary particle accelerator in the world which collides electrons or positrons and protons. It is located at the DESY (Deutsches Elektronen SYNchrotron) laboratory, in Hamburg, northern Germany, and operates since autumn 1991. The HERA machine collides electrons or positrons, accelerated to an energy of 27.5 GeV, with 820(920) GeV protons (the energy of the proton beam was changed at the beginning of 1998 from 820 to 920 GeV). The resulting centre-of-mass energy is 300(318) GeV, more than an order of magnitude higher than the previous fixed-target experiments. As a consequence a new and wider kinematic region is accessible at HERA.

The HERA tunnel is 6.3 km long and it is located 15–30 m under the ground level. Electrons (positrons) and protons are accelerated in two different rings. The magnetic system of the lepton ring consists of conventional magnets with maximum field of 0.165 T, while the proton beam is made of superconducting magnets with a maximum field of 4.65 T.

Four experiments are located in four experimental halls along the HERA ring.  $ep$  collisions occur in two interaction points, one in the North Hall where the H1 experiment is located, the other in the South Hall where the ZEUS experiment

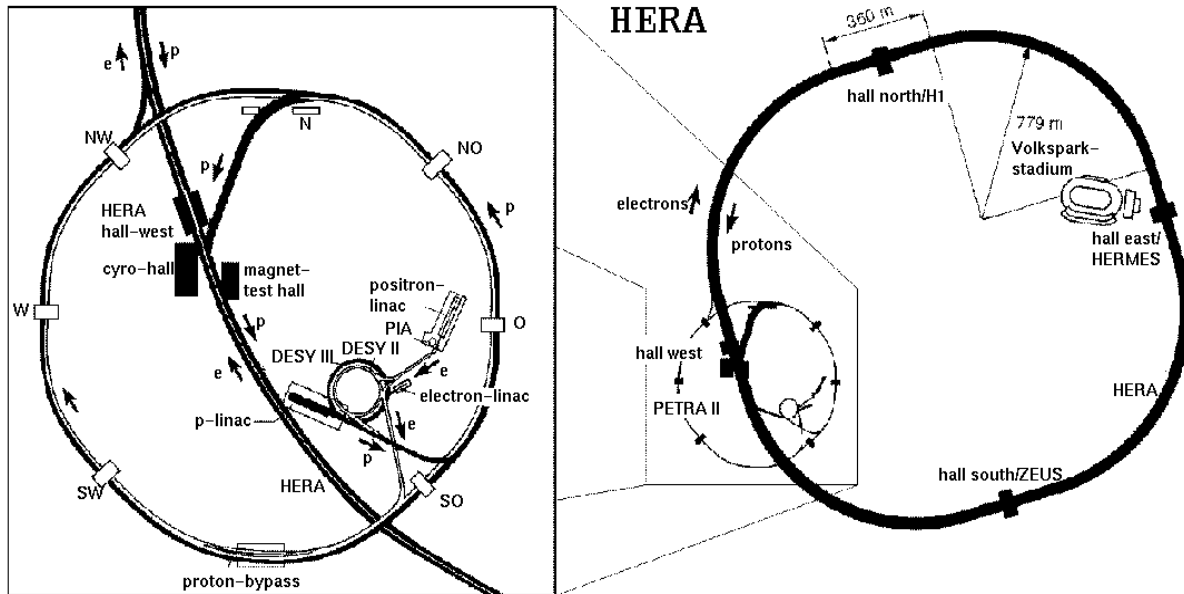


Figure 3.1: The HERA storage ring with its pre-accelerators system.

is placed. In the East Hall the HERMES experiment is located, which studies the spin structure of the nucleon using the collisions of polarized leptons on an internal polarized gas target. The HERA-B experiment, located in the West Hall, was built to use collisions of the proton beam halo with a wire target to produce  $B$ -mesons for the study of  $\mathcal{CP}$  violation in the  $B - \bar{B}$  system.

Fig. 3.1 shows a layout of the HERA facility and of its pre-accelerators system. The proton acceleration chain starts with negative hydrogen ions ( $\text{H}^-$ ) accelerated in a LINAC to 50 MeV. The electrons are then stripped off the  $\text{H}^-$  ions to obtain protons, which are injected into the proton synchrotron DESY III, accelerated up to 7.5 GeV, and then transferred to PETRA, where they are accelerated to 40 GeV. Finally they are injected into the HERA proton storage ring, where they reach the nominal beam energy of 920 GeV.

The electron (positron) pre-acceleration chain starts in a linear accelerator, LINAC I (LINAC II), where the leptons are accelerated up to 450 MeV. The leptons are then injected into DESY II, accelerated to 7 GeV and then transferred to PETRA II, where they reach an energy of 14 GeV. They are then injected into

HERA design parameters

Running period	1993 - 1997		1998 - 2000	
Luminosity	$1.6 \cdot 10^{31} \text{ cm}^{-1}\text{s}^{-1}$		$1.6 \cdot 10^{31} \text{ cm}^{-1}\text{s}^{-1}$	
Center-of-mass energy (actual)	300 GeV		318 GeV	
	Lepton	Proton	Lepton	Proton
Energy (actual)	27.5 GeV	820 GeV	27.5 GeV	920 GeV
Max. number of bunches	210	210	210	210
Beam current	58	163	58	163
Particles per bunch	$3.65 \cdot 10^{10}$	$10^{11}$	$3.65 \cdot 10^{10}$	$10^{11}$
Beam width ( $\sigma_x$ )	0.286 mm	0.280 mm	0.286 mm	0.280 mm
Beam height ( $\sigma_y$ )	0.060 mm	0.058 mm	0.060 mm	0.058 mm

**Table 3.1:** Main design parameters of HERA [63].

Year	HERA Luminosity ( $pb^{-1}$ )
$e^-$ 92 – 94	2.19
$e^-$ 94 – 97	70.92
$e^-$ 98 – 99	25.20
$e^-$ 99 – 00	94.95

**Table 3.2:** Overview of the luminosity delivered by HERA from 1992 to 2000.

HERA where they reach the nominal lepton beam energy of 27.5 GeV. HERA can be filled with a maximum of 210 bunches of each leptons and protons spaced by 96 ns. Some of these bunches are kept empty (*pilot* bunches) in order to study the background conditions. When either the lepton or the proton bunch is empty, the beam-related background, originating from the interaction of the lepton or the proton beam with the residual gas in the beam pipe, can be studied, whereas when both the bunches are empty the non-beam-related background can be estimated, as the rates of cosmic rays.

In Fig. 3.2 and in Table 3.2 the performance of HERA in the last years is shown. The running operations began in 1992 with an electron beam, but in 1994 it was realized that the electron beam current was limited by positively ionized dust particles getting in the beam pipe through the pumps, reducing the lifetime of the beam. For this reason HERA switched to positrons in July 1994, achieving a more stable lepton beam and a significant increase in the integrated luminosity of the collected data. During the 1997–98 shutdown period, new pumps were installed in the lepton beam to improve the electron beam lifetime, and therefore

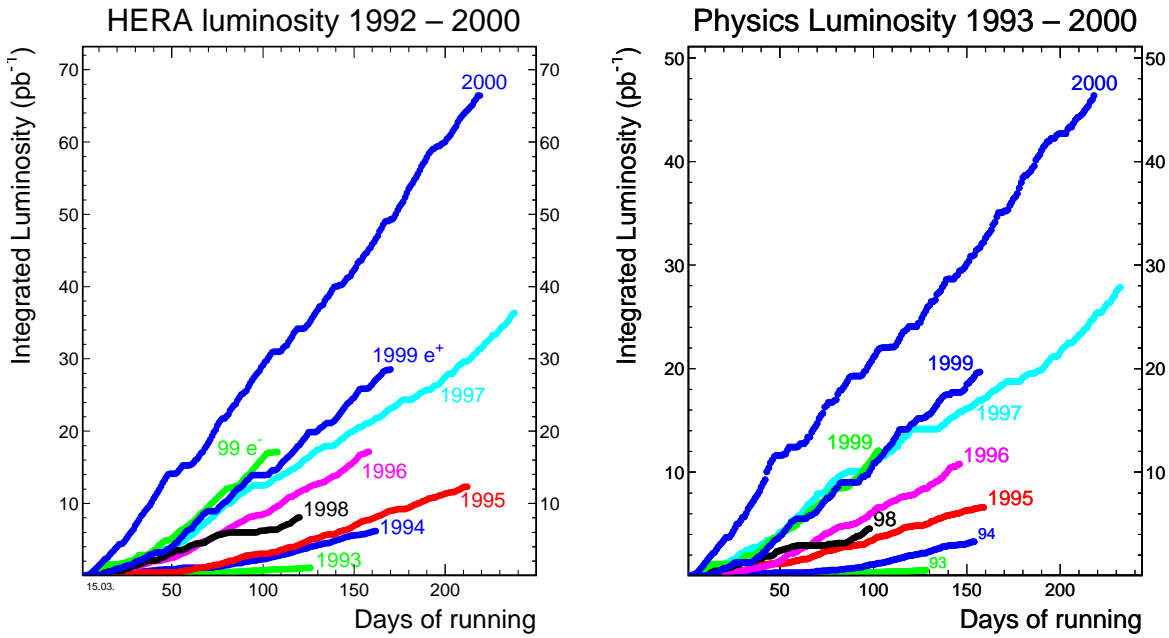


**Figure 3.2:** Integrated luminosity delivered by HERA (left) and usable for ZEUS physics analyses (right) in the 1993–2000 running period.

during 1998 and part of 1999 HERA was running again with electrons. It was also in 1998 that the energy of the proton beam was raised from 820 to 920 GeV.

Although a lot of interesting measurements have already been performed at HERA, the desire was expressed by the experiments for an increase in the luminosity. The motivations for this increase were studied in a one-year workshop held between 1995 and 1996, when it was concluded that having  $1 \text{ fb}^{-1}$  of integrated luminosity would have opened the possibility for new interesting measurements. The luminosity upgrade [64] of the machine, done between the end of 2000 and 2001 shutdown period, should bring a significant increase in the luminosity (around a factor 5).

## 3.2 The ZEUS Detector

The ZEUS detector [62] is a general purpose detector designed to study various aspects of lepton–proton scattering at HERA. It is a quasi hermetic detector since

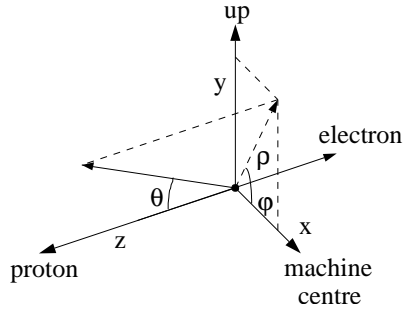


**Figure 3.3:** The ZEUS coordinate system.

it covers most of the  $4\pi$  solid angle with the exception of small regions around the beam pipe. Most of the final state particles are boosted to the forward direction because of the large momentum imbalance between the lepton and the proton beam.

The layout of the detector was dictated by the topology of the processes to be studied at HERA. The detector can measure energies from few tens of MeV to hundreds of GeV in the forward region. For low momentum particles the tracking in the magnetic field is very precise (resolution:  $\sigma(p_T)/p_T \sim p_T$ ), while high energy particles are well measured by the calorimetric system (resolution:  $\sigma(E)/E \sim \sqrt{E}/E$ ).

The ZEUS coordinate system is shown in Fig. 3.3. It is a right-handed, orthogonal system with the origin at the nominal interaction point (IP), the  $z$  axis pointing in the proton direction (also referred to as the *forward* direction), the  $x$  axis pointing toward the center of HERA and the  $y$  axis pointing upward. The polar angle  $\theta$  and the azimuth angle  $\phi$  are measured relative to the  $z$  and  $x$  axes respectively. The pseudorapidity,  $\eta$ , which is defined as

$$\eta = -\ln\left(\tan\frac{\theta}{2}\right) \quad (3.1)$$

is often used instead of  $\theta$ .

The ZEUS sub-detectors are arranged coaxially but asymmetrically around the interaction point to accommodate the boost of the centre-of-mass system in the proton beam direction with respect to the laboratory frame due to the large energy asymmetry between the lepton and the proton beams. A cross

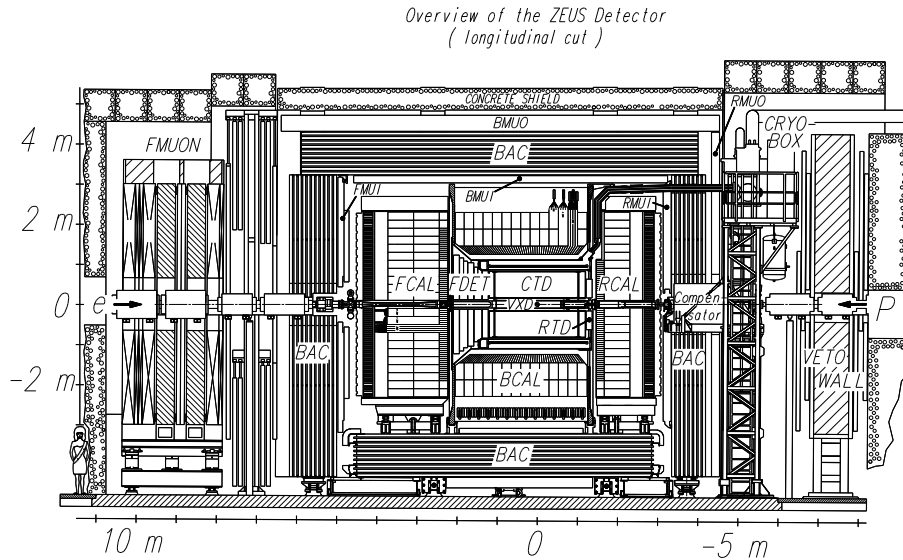


**Figure 3.4:** Cross section of the ZEUS detector along the beam axis.

section of the detector layout along the beam axis is shown in Fig. 3.4. The main detector is approximately 20 m long, 12 m wide and 11 m high and weighs around 3600 t. A short description of the main components of the detector is given in the following. A more detailed description of the sub-detectors of particular interest for the analysis reported here will be given later in this Chapter. The innermost detector that can be seen in Fig. 3.4 is the Vertex Detector (VXD), that was removed during the 1995–96 shutdown. Therefore during 1996–2000 data-taking the detector closest to the interaction point was the central tracking detector (CTD, see 3.2.1) which is a cylindrical drift chamber. It is enclosed by a superconducting solenoid providing a magnetic field of 1.43 T for the determination of charge and momentum of charged particles. The CTD is supplemented in the forward direction by three sets of planar drift chambers (FTD) with interleaved Transition Radiation Detectors (TRD) (labeled FDET in Fig. 3.4). The rear direction is supplemented by one planar drift chamber consisting of three layers (RTD).

The tracking system is surrounded by a compensating high resolution uranium–scintillator calorimeter (CAL, see 3.2.2) which is used as the main device for energy measurements. It is divided into forward, barrel and rear sections (respectively FCAL, BCAL and RCAL) with different thicknesses. The calorimeter is enclosed by an iron yoke that provides the return path for the

solenoidal magnetic field flux, and serves as absorber for the BAcKing Calorimeter (BAC), which measures energy that escapes detection from the main calorimeter. Dedicated muon identification detectors (see 3.2.3) are located inside (FMUI, BMUI and RMUI) and outside (FMUO, BMUO and RMUO) the iron yoke.

Other detectors are located several meters away from the main detector along the beam pipe. The VETO wall is located in the rear direction at about  $z = -7.5$  m from the interaction point. It consists of an iron wall supporting scintillator hodoscopes and is used to reject background from beam gas interactions. The LUMI detector (see 3.2.6) is made of a small lead-scintillator calorimeter at  $z = -107$  m and detects photons from bremsstrahlung events for the luminosity measurement.

### 3.2.1 The Central Tracking Detector (CTD)

The Central Tracking Detector (CTD) [65] is a cylindrical wire drift chamber used to measure the directions and momenta of the charged particles and to estimate the energy loss  $dE/dx$  to provide information for particle identification. The inner radius of the chamber is 18.2 cm, the outer is 79.4 cm, and its active region covers the longitudinal interval from  $z = -100$  cm to  $z = 104$  cm, resulting in a polar angle coverage of  $15^\circ < \theta < 164^\circ$ . The CTD is filled with a mixture of argon (Ar), carbon dioxide (CO<sub>2</sub>) and ethane (C<sub>2</sub>H<sub>6</sub>) in the proportion 85:5:1. The CTD consists of 72 radial layers of sense wires, divided in groups of eight into nine *superlayers* (SL). A group of eight radial sense wires with associated field wires in one superlayer makes up a *cell*. The drift cells in each superlayer are similar. The sense wires are 30  $\mu\text{m}$  thick while the field wires have different diameters. A total of 4608 sense wires and 19584 field wires is contained in the CTD. The CTD is designed to operate in a magnetic field. The 8 sense wires are in a plane, at  $45^\circ$  to the radial line from the chamber axis. The drift field is at a Lorentz angle of  $45^\circ$  to the radial axis, which helps in left - right ambiguity breaking. One octant of the CTD is shown in Fig. 3.5.

A charged particle crossing the CTD produces ionization of the gas in the chamber. The electrons from the ionization drift toward the sense wires (positive), whereas the positively charged ions drift toward the negative field wires. The drift velocity of the electron is approximately constant and equal to  $50\mu\text{m}/\text{ns}$ ; during the drift an avalanche effect occurs, giving an amplification factor on the electrons of  $\sim 10^4$ , so that a readable pulse is induced on the sense wires.

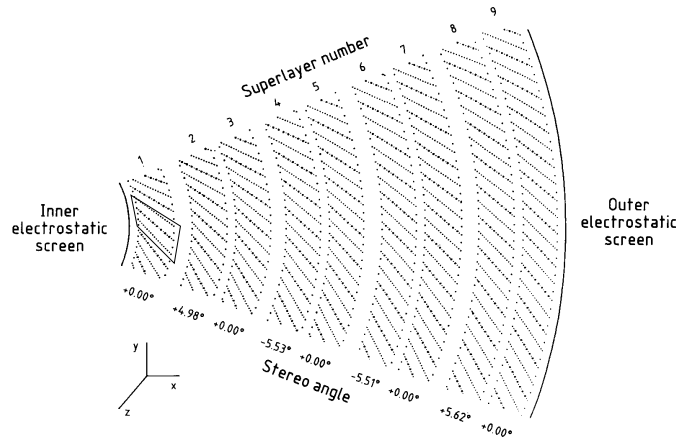


**Figure 3.5:**  $x - y$  cross section of one octant of the CTD. The sense wires are indicated with dots.

The superlayers are numbered so that the number 1 is the innermost SL, whereas the outermost is number 9. For trigger purposes, the three inner axial superlayers (SL1, SL3, SL5) are equipped with a system that determines the  $z$  positions using the time difference between the arrival times of the signal from the opposite ends of the CTD ( $z$ -by-timing system). The resolution achieved on the  $z$  coordinate with this system is  $\sim 4$  cm.

Odd numbered SLs have wires parallel to the  $z$  direction (axial superlayers), while wires in even numbered SLs are at a small stereo angle of  $\pm 5^\circ$  (stereo superlayers) to achieve a better resolution in  $z$ . The achieved resolution is  $\sim 200 \mu\text{m}$  in the  $r - \phi$  plane and  $\sim 2$  mm in the  $z$  coordinate.

The resolution on  $p_T$ , for tracks fitted to the interaction vertex and passing at least three CTD superlayers, and with  $p_T > 150$  MeV, is given by:

$$\frac{\sigma(p_T)}{p_T} = 0.0058 \cdot p_T \oplus 0.0065 \oplus \frac{0.0014}{p_T} \quad (3.2)$$

where the symbol  $\oplus$  indicates the quadratic sum. The first term is the hit position resolution, while the second and the third depend on the multiple scattering inside and before the volume of the chamber, respectively.

### 3.2.1.1 Track reconstruction

The information used to determine the spatial position of a particle, needed for the track reconstruction, come from the time of arrival of the ionization electrons

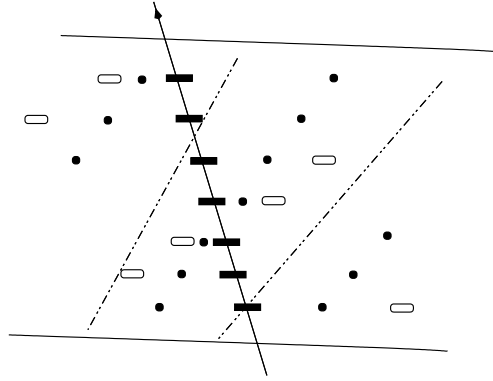


**Figure 3.6:** Hits coming from a genuine track (solid rectangles) tend to cross the cell boundaries within a superlayer. The open rectangles are ghost hits.

on the sense wire. If the drift velocity is approximately constant and equal to  $u_d$ , the relation between the drift time,  $t_d$ , and the distance from the sense wire,  $d_s$ , is given by:

$$d_s \simeq u_d \cdot t_d \quad (3.3)$$

where  $t_d$  is defined as the difference between the time  $t_f$  at which the pulse appears on the sense wire, and the time  $t_i$  of passage of the charged particle, calibrated for every wire,  $t_d = t_f - t_i$ . However, this kind of information is not sufficient to determine from which side of the wire the particle comes, therefore a left–right ambiguity is still present. The  $45^\circ$  tilt of the sense wires can solve this ambiguity, since tracks coming from the interaction point tend to pass the boundary of adjacent cells within a superlayer, as shown in Fig. 3.6.

The pattern recognition of the track begins looking for a *seed*, a group of hits in the outermost superlayer (SL9). To these hits a virtual hit at  $x = y = 0$  is added, taking into account the transverse dimension of the beam as an error on this hit. The two hits are enveloped with a circle arc, and inner hits on the axial superlayers are added on the way, updating the circle parameters and refining the trajectory determination. Once the trajectory spans several axial superlayers, the arc in the  $XY$  plane is used for the stereo pattern recognition: stereo hits are selected that match with the arc after being rotated. The pattern recognition begins with the longest tracks, those going from SL9 to SL1, then continues with shorter tracks, reaching inner superlayers (SL7, SL5...), and finally includes tracks

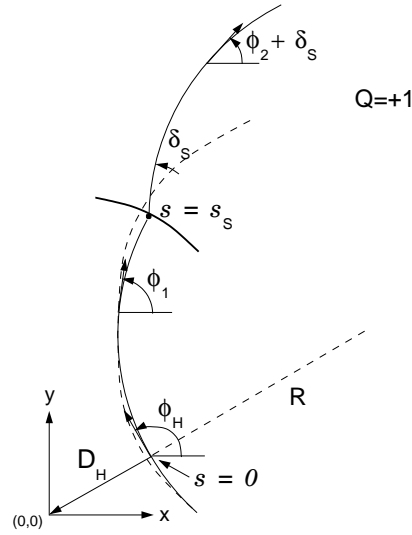


**Figure 3.7:** The track helix in the  $xy$  plane.

with no hits in the innermost superlayer, that can come from the decay of long lived particles.

When the pattern recognition is done, all the candidate tracks are fitted with a helix, starting with the innermost superlayer and adding the outer ones on the way. The five helix parameters are (Fig.3.7):

- $a_1 = \phi_H$ , the angle tangent to the helix in the  $xy$  plane;
- $a_2 = Q/R$ , where  $Q$  is the charge and  $R$  the radius of the helix;
- $a_3 = QD_H$ , where  $D_H$  is the distance of the helix from the reference point;
- $a_4 = z_H$ , the  $z$  position of the point of closest approach;
- $a_5 = \cot\theta$ , where  $\theta$  is the polar angle.

The event vertex is then reconstructed from the information on the fitted tracks. Tracks too far from the determined vertex are discarded, the surviving tracks are constrained to the vertex and the fit parameters recalculated.

### 3.2.2 The Uranium–scintillator Calorimeter (UCAL)

The ZEUS calorimeter (UCAL) [66] is a high–resolution compensating calorimeter. It completely surrounds the tracking devices and the solenoid, and covers

99.7% of the  $4\pi$  solid angle. It consists of 3.3 mm thick depleted uranium plates (98.1%  $U^{238}$ , 1.7% Nb, 0.2%  $U^{235}$ ) as absorber alternated with 2.6 mm thick organic scintillators (SCSN-38 polystyrene) as active material. The thickness of the absorber and of the active material have been chosen in order to have the same response for an electron or a hadron of the same energy ( $e/h = 1.00 \pm 0.02$ ) passing through the detector. This mechanism is called *compensation*, and allows to achieve good resolution in the determination of both the electromagnetic and the hadronic energy. The achieved electromagnetic resolution is

$$\frac{\sigma(E)}{E} = \frac{18\%}{\sqrt{E}} \oplus 2\%, \quad (3.4)$$

while the hadronic resolution is

$$\frac{\sigma(E)}{E} = \frac{35\%}{\sqrt{E}} \oplus 1\% \quad (3.5)$$

where  $E$  is the particle energy, measured in GeV.

The UCAL is divided into three parts: the forward (FCAL), barrel (BCAL) and rear (RCAL) calorimeter (Fig. 3.8). Since most of the final state particles in a lepton-proton interaction at HERA are boosted in the forward (proton) direction, the three parts are of different thickness, the thickest one being the FCAL ( $\sim 7 \lambda$ ), then the BCAL ( $\sim 5 \lambda$ ) and finally the RCAL ( $\sim 4 \lambda$ ), where  $\lambda$  is the interaction length. Each part of the calorimeter is divided into *modules*, and

CAL Part	Angular coverage	EMC	HAC
FCAL	$2.5^\circ - 39.9^\circ$	$20 \times 5 \text{ cm}^2$	$20 \times 20 \text{ cm}^2$
BCAL	$36.7^\circ - 129.2^\circ$	$20 \times 5 \text{ cm}^2$	$20 \times 20 \text{ cm}^2$
RCAL	$128.1^\circ - 178.4^\circ$	$20 \times 10 \text{ cm}^2$	$20 \times 20 \text{ cm}^2$

**Table 3.3:** Angular coverage of the CAL parts and dimensions of the cells.

each module is divided into one electromagnetic (EMC) and two (one in RCAL) hadronic (HAC) sections. These sections are made up of *cells*, whose sizes depend on the type (EMC or HAC) and position (in FCAL, BCAL or RCAL) of the cell, as reported in Table 3.3.

The FCAL consists of one EMC (first 25 uranium-scintillator layers) and two HAC (remaining 160 uranium-scintillator layers) sections. The electromagnetic



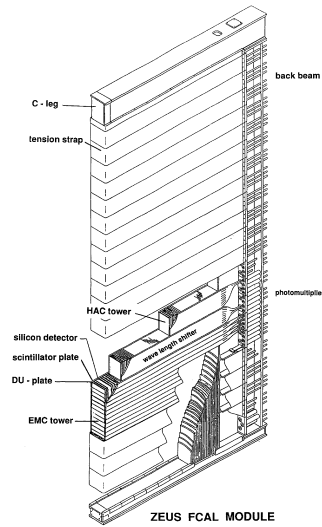


**Figure 3.9:** A FCAL module.

it is very useful for trigger purposes in order to reject background events, as it will be illustrated later, in the trigger Section.

The stability of the PMTs and of the electronics is monitored with lasers and charge pulses. In addition, the small signal coming from the natural radioactivity of the depleted uranium gives a very stable signal, also used for the calibration. The achieved accuracy is better than 1%.

### 3.2.3 The Muon Detectors

Muons can traverse large amounts of material without being absorbed since they lose energy mainly by ionisation. The muon detectors have to measure tracks produced in the interaction region which cross the whole calorimeter thickness and the iron yoke.

The momenta of the muons can be very different depending on their polar angle due to the boosted system to the forward region. Muons with more than 10 GeV momentum are frequently produced in this region. In the barrel and rear regions the average momentum of the muons is expected to be much smaller. Therefore the muon detection system is split into two sub-detectors, the forward muon detector (FMUON, see 3.2.3.1) and the barrel and rear muon detector (BMUON and RMUON respectively, see 3.2.3.2).

### 3.2.3.1 The Forward Muon Detector

The forward muon detector [62] is divided into two regions (see Figure 3.10). The inner region is located between the FCAL and the BAC (FMUI), the other is positioned outside the BAC (FMUO). The FMUON detector consists of:

- a system of four planes of limited streamer tubes [67] trigger planes (LST1 - LST4) with digital  $\rho$  and  $\phi$  readout;
- two coverage planes of limited streamer tubes with digital ( $\rho, \phi$ ) and analog ( $\rho$ ) readout in the large polar angle region (LW1, LW2);
- four planes of drift chambers (DC1 - DC4);
- two large toroidal iron magnets providing a magnetic field of 1.7 T for the momentum separation and measurement in the angular region  $5^\circ < \theta < 16^\circ$ .

The first plane of LST and drift chambers make up the FMUI detector while the rest of the system is placed outside the iron yoke.

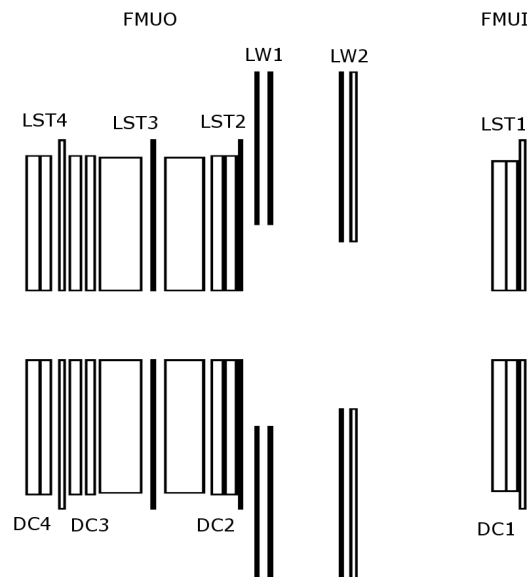


**Figure 3.10:** Schematic view of the forward muon detector along the beam axis.

The individual components of the FMUON detector are described in the following.

**The limited streamer tube planes:** The aim of the limited streamer tube (LST) planes is to trigger on muon candidates and to reconstruct their position in terms of the azimuthal and radial coordinates of the track. A trigger plane is made of four LST chambers grouped in two half-planes. A quadrant consists of two layers of LST positioned horizontally inside a plastic sheet. The tubes of the two planes are slightly displaced (0.5 cm) in order to achieve a complete geometrical acceptance. Each quadrant is contained in an air tight aluminum box. On the outer side, copper strips are glued in polar geometry. The LSTs induce a signal in the copper strips if a particle crosses the plane. The number of radial  $\rho$  strips is 132 while each strip is 1.9 cm wide. They are divided along the bisector of the quadrant so that the simplest unit of the trigger plane to be read out is the octant. The number of  $\phi$  strips is 32 per octant. Each strip covers an interval of  $1.4^\circ$  in the azimuthal angle.

**The drift chambers:** The drift chambers are needed in order to obtain a good momentum resolution. Each plane consists of four chambers grouped two by two in two half planes fixed on a support panel. The basic element of the chamber is the *cell* made of four sense wires and of the layers needed to generate the appropriate electric field. The four sense wires measure the radial coordinate. The information gathered by the wires are sent to a TDC which converts them into a time interval related to the drift distance by a known relation.

**The large angle coverage planes:** The two large angle coverage planes (LW) are needed in order to achieve the desired geometrical acceptance also in the region left uncovered by the toroids ( $16^\circ < \theta < 32^\circ$ ). Each plane consists of eight air tight aluminum wrappings that contain a LST layer. The LST signal is induced on copper strips with radial geometry spaced of  $0.7^\circ$  in the  $\phi$  coordinate and of 1.8 cm in the  $\rho$  coordinate. The number of  $\phi$  strips is 64 per octant while the  $\rho$  strips are 192 per octant. The achieved resolution in the  $\rho$  coordinate, using a center of gravity algorithm, is  $\sim 1$  mm.

### 3.2.3.2 The Barrel and Rear Muon Detector

The barrel and rear muon detector [68] covers a very large area ( $\sim 2000$  m<sup>2</sup>) and consist of LST *chambers* as the basic structure. The chambers covering the

inner barrel part between the CAL and the iron yoke are called BMUI while the chambers situated outside the yoke are denoted as BMUO. The rear region is divided into RMUI and RMUO chambers in a similar way (see Fig. 3.11).

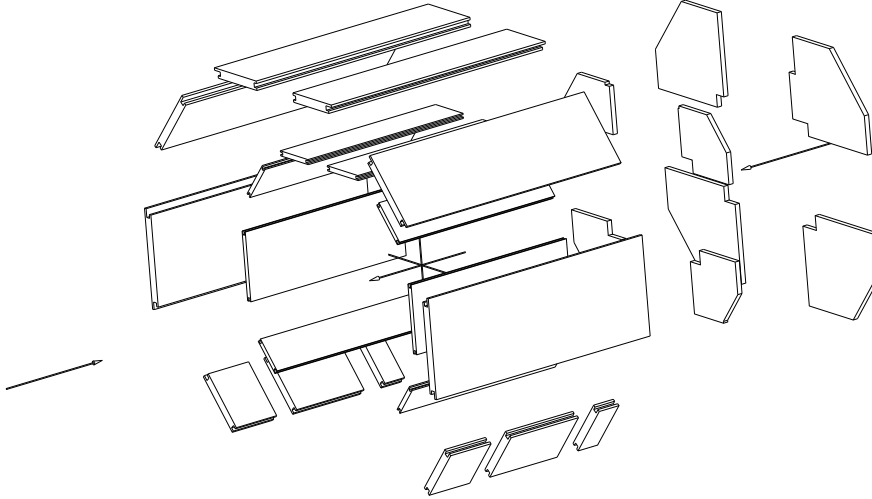


**Figure 3.11:** Layout of the barrel and rear muon detector.

The chambers have different shapes and dimensions depending on their location, but their internal structure is always the same. The supporting structure of each chamber is an aluminum honeycomb frame 20 cm thick in the rear chambers and 40 cm in the barrel ones. Two planes of LST are placed on both sides of the honeycomb. The two layers on the same side of the chamber are displaced by 8.3 mm in order to minimize dead areas for particles traversing at  $90^\circ$  with respect to the wire plane. Each LST is made of a plastic profile with eight cells. In each cell a copper-beryllium wire of  $100 \mu\text{m}$  diameter is located. The distance between two sense wires is 1 cm.

Each LST plane is equipped on one side by 13 mm wide readout strips with 15 mm pitch that run orthogonal to the wires. In the BMUI and BMUO chambers the LSTs are parallel to the beam direction while in RMUI and RMUO they are horizontal (parallel to the ZEUS  $x$  direction). With the analog strip readout the achievable spatial resolution on the coordinate orthogonal to the wires is  $200 \mu\text{m}$  while it is  $700 \mu\text{m}$  for the coordinate parallel to the wires.

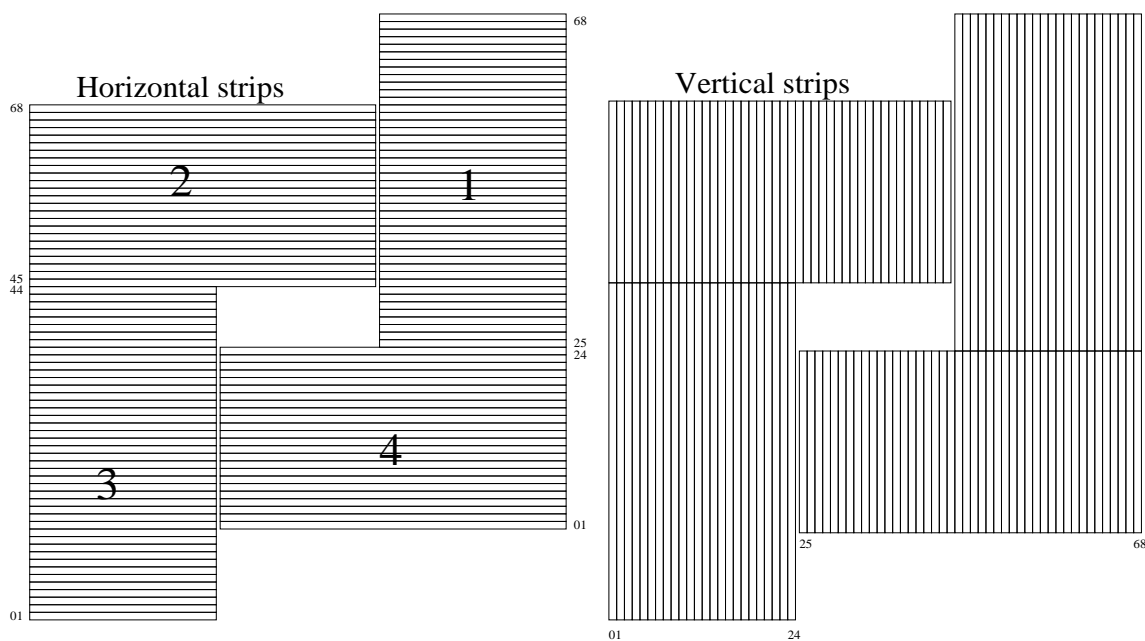


**Figure 3.12:** Orientation and numbering scheme of the strips of the two SRTD planes. The strip size is 0.98 cm × 24(44) cm.

### 3.2.4 The Small Angle Tracking Detector (SRTD)

In order to improve the measurement of the energy and angle of the scattered electron for low  $Q^2$  events, a Small Angle Tracking Detector (SRTD) has been installed in 1994 [71]. It is attached to the front face of the RCAL and covers approximately an area of 34 cm radius around the beam pipe (Fig. 3.12). The SRTD consists of a horizontal and a vertical layer of 1 cm wide and 0.5 cm thick scintillator strips. Position and pulse height information is provided via optical fiber and photomultiplier readout. The SRTD is used to measure the electron impact position as described in section 4.4.2. The position resolution was determined from the data using DIS electrons with impact position near the boundary between two calorimeter cells [71]. In this restricted region, selected using the energy imbalance between two neighboring cells, the calorimeter position resolution is better than 0.1 cm although the average resolution is only 1 cm. The measured SRTD position resolution is approximately 0.3 cm in both coordinates.

### 3.2.5 The Hadron Electron Separator (HES)

The Hadron Electron Separator (HES) [72] consists of a layer of pad detectors of  $3 \times 3.3$  cm<sup>2</sup> silicon diodes, providing a spatial resolution of about 9 mm for a single hit pad. It has been installed in RCAL (and FCAL) at a longitudinal depth of 3.3 radiation lengths  $X_0$  which corresponds to the approximate position of the electromagnetic shower maximum. Because the hadronic interaction length is 20 times larger than the electromagnetic radiation lengths and thus hadrons have a smaller HES signal compared with electromagnetic particles. If more than one adjacent pad is hit by a shower, a cluster consisting of at most  $3 \times 3$  pads around the most energetic pad is considered, which allows reconstruction of the incident particle position with the improved resolution of 5 mm.

### 3.2.6 The Luminosity Measurement

The luminosity measurement at ZEUS [73] is made using a particle reaction with a well known cross section  $\sigma_{proc}$  and the corresponding observed number of events corrected for acceptance and efficiency to calculate the luminosity by the following formula:

$$\mathcal{L} = \frac{N_{proc}}{\sigma_{proc}} \quad (3.6)$$

Lepton-proton bremsstrahlung  $ep \rightarrow e'p\gamma$  where the lepton and the photon are scattered at very small angles is chosen for the luminosity measurement at ZEUS. This process has a large cross section ( $\sigma_{BH} \geq 20$  mb) yielding sufficient statistics. The differential cross section as function of the photon energy of this

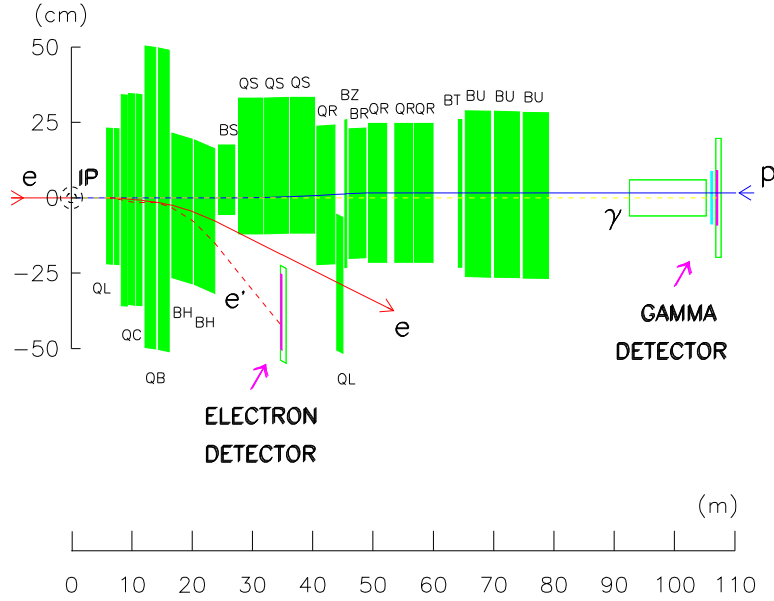


**Figure 3.13:** Schematic view of the lumi monitor system.

process is described by the Bethe–Heitler formula [74] and is known with an accuracy of  $\sim 0.5\%$ :

$$\frac{d\sigma}{dk} = 4\alpha r_e^2 \frac{E'}{kE} \left( \frac{E}{E'} + \frac{E'}{E} - \frac{2}{3} \right) \left( \ln \frac{4E_p E E'}{m_e m_p k} - \frac{1}{2} \right) \quad (3.7)$$

where  $\alpha$  is the fine structure constant,  $r_e$  the classical electron radius,  $k$ ,  $E$  and  $E'$  the energies of the photon, the incoming and outgoing electron, respectively. Bremsstrahlung photons emitted at an angle  $\theta_\gamma < 0.5$  mrad with respect to the beam axis leave the beampipe through a Cu-Be window of a thickness of  $0.095 X_0$  at  $Z = -92.5$  m. They are detected by a lead/scintillator sampling calorimeter (LUMIG) at  $z = -107$  m (Fig. 3.13).

The detector is shielded from synchrotron radiation by a graphite block with a thickness of  $2 X_0$  resulting in an energy resolution of  $\sigma(E)/E = 23\%/\sqrt{E}$  ( $E$  measured in GeV). The impact position of the photons can be reconstructed with a resolution of 3 mm making use of the embedded layers of scintillator fingers.

The bremsstrahlung event rate is determined by counting the number of photons above a fixed energy threshold. The luminosity is then calculated by dividing the evaluated rate by the bremsstrahlung cross section corrected for the detector acceptance.

The main contribution to the background is given by the bremsstrahlung of leptons on the residual gas in the beam pipe. This can be measured using *pilot* bunches, i.e. lepton bunches with no associated proton bunch, evaluating for these the rate of bremsstrahlung events. The statistical uncertainties are negligible due to the sufficiently large recorded Bethe-Heitler rates. The systematic uncertainty of the luminosity measurement originates mainly from the background subtraction, pile-up effects and the energy calibration, linearity and acceptance of the photon calorimeter. The achieved precision is of the order of 1.5 – 2%.

### 3.2.7 The ZEUS trigger system

The HERA beam bunch structure leads to a beam crossing every 96 ns corresponding to a rate of potentially interesting events of 10.4 MHz. The rate of  $ep$  events ranges from less than 0.1 Hz for NC DIS events with  $Q^2 > 100 \text{ GeV}^2$  to 250 Hz for soft photoproduction (for an instantaneous luminosity of  $2 \cdot 10^{31} \text{ cm}^{-2}\text{s}^{-1}$ ). The rate of background events, on the other hand, can exceed the rate of physics events by several orders of magnitude. It is coming mainly from interactions of protons with the residual gas nuclei or elements of the beamline (beam gas events). Beam gas events occur typically at a rate of 10 kHz. In addition, cosmic muons traversing the detector contribute to the background rate. The total data size per event is 150 kB and the writing speed is limited to  $\sim 1.5 \text{ MB/s}$ . Hence a significant reduction of the data rate and size is required.

A three level trigger system [75] with increasing complexity of the decision making algorithm and decreasing throughput rate is used to select events online.

### 3.2.7.1 The First Level Trigger (FLT)

The First Level Trigger has to strongly suppress the following background events, in order to pass a cleaner sample to the other trigger components:

- events coming from interactions of leptons or protons with the residual gas in the beam pipe, near the interaction point. The estimated rate of this kind of events, assuming a sensitive region of 100 m before and after the interaction point, with the nominal beam currents and with a vacuum of  $10^{-9}$  Torr, is 50 kHz;
- events coming from interactions of the protons in the beam halo with the collimators, that can produce secondary hadrons decaying into high energy muons, crossing all the detector; these events, however, have a typical topology (the muons are typically parallel to the proton beam direction) and usually can easily be distinguished from  $ep$  events;
- cosmic ray muons, with a rate of the order of 1 kHz.

The First Level Trigger has to deal with the HERA bunch crossing so it has to handle events at a rate of 10 MHz, giving as output events at a rate of the order of 1 kHz, the design rate of the Second Level Trigger. The FLT is a hardware trigger, designed to analyse every bunch crossing. The data of each bunch crossing are stored into pipelines, that are 46 bunch crossing deep and allows the FLT a time of  $4.4 \mu\text{s}$  to accept or discard an event. The FLT operates on a subset of the full data coming from an event, based essentially on the calculation of crude event observables (regional energy sums, number of tracks, timing information...).

Each detector component has its own first level trigger processor, and the  $4.4 \mu\text{s}$  interval has to be shared between the components trigger and the Global First Level Trigger (GFLT). After 26 bunch crossing times ( $2.5 \mu\text{s}$ ) every component send its FLT signal to the GFLT, which uses the remaining 20 crossing times ( $1.9 \mu\text{s}$ ) to take the final decision. The components data are processed and combined in parallel in eight Trigger Logic Modules of the GFLT, and 64 individual sub-triggers (*slots*) are generated. The GFLT accepts or rejects the event looking at the OR of these 64 sub-triggers.

If the event is accepted, all the components have to digitize their data in order to send them to a system of digital CPUs for the next analyses. This operation

takes  $\sim 10 \mu\text{s}$  after the GFLT decision, and during this time no event acquisition is possible. This is the only dead-time of the GFLT chain, and is of the order of 1%.

### 3.2.7.2 The Second Level Trigger (SLT)

The Second Level Trigger (SLT) [76] further reduces the background events with respect to the  $ep$  events. The SLT, which receives events from the FLT with a rate of 1000 Hz, has an output rate of 100 Hz. The SLT is software-based and runs on a network of transputers [77]. The analysis of the events is done in parallel so that the available processing time is much larger than at the FLT, of the order of some milliseconds. As in the FLT, each detector component has its own SLT processor, and all the information from the single components are sent to the Global Second Level Trigger (GSLT) after the processing.

The information the GSLT uses to distinguish between  $ep$  and background events are based mainly on the time of arrival of the particles at the calorimeter. As was shown in section 3.2.2, the UCAL can give timing information with a resolution of the order of 1 ns. The time is calibrated so that a physics event originating from the interaction point have zero time in the whole calorimeter. A proton-gas event, originating upstream of the detector, produces particles reaching the RCAL before the FCAL, with a time differing of  $\sim 10$  ns. In the same way, events coming from lepton-gas interactions downstream the detector will produce particles arriving to the FCAL before than to the RCAL, with a time difference larger than the UCAL timing resolution. Also cosmic events and electronic noise will appear as asynchronously to the HERA time and would therefore be suppressed.

The timing information from the UCAL is available when at least one cell above threshold (200 MeV) has been read by PMTs on both sides. The times are calculated by a weighted average on all the cells above threshold, for the different regions, with a bigger weight for the more energetic cells. In more detail, the filters applied to separate  $ep$  and background events are:

- *RCAL timing*: used to reject events coming from proton beam interactions with the residual gas in the beam pipe. Events are rejected if  $|T_{RCAL}| > 8$  ns.
- *FCAL timing*: used to reject events coming from interactions of the lepton beam with residual gas in the beam pipe. Events are rejected if  $|T_{FCAL}| > 8$  ns.

- *F-RCAL timing*: events coming from real  $ep$  interactions have particles with the same time in FCAL and in RCAL, so that  $T_{FCAL} - T_{RCAL} \simeq 0$ , while beam-gas events upstream the interaction point have times in FCAL and RCAL that differs of  $\sim 10$  ns. The events are rejected if  $T_{FCAL} - T_{RCAL} > 8$  ns.
- *Up-down timing*: used to reject cosmic muon events, that reach the upper part of the BCAL before the lower. The event is rejected if both halves of the BCAL have valid timing, if there is no activity in the FCAL and RCAL, and if  $T_{up} - T_{down} < -10$  ns.
- *E and  $p_z$* : used to reject beam-gas interactions occurring near the interaction region. Since these events can essentially be thought as proton collisions on a fixed target, the produced particles have

$$\frac{\sum_i E_i \cos\theta_i}{\sum_i E_i} \sim 1 \quad (3.8)$$

where  $E_i$  is the energy of the  $i$ th cell of the calorimeter and  $\theta_i$  is its polar angle. The event is rejected if

$$\frac{\sum_i E_i \cos\theta_i}{\sum_i E_i} > 0.96. \quad (3.9)$$

- *Global timing*: if one of the calorimeter times is valid and greater than 10 ns, the event is rejected.

### 3.2.7.3 The Third Level Trigger

If the event is accepted by the GSLT, all the components send their information to the event builder (EVB), which combines their data, writes them in a standard format, and makes them accessible to the Third Level Trigger (TLT). The input rate to the TLT is of 100 Hz, while the output rate is 3 – 5 Hz, similar to the rate of the  $ep$  interactions. Therefore the aim of the TLT is not only to reject background events but also to select the particular classes of  $ep$  interactions under investigation.

The TLT consists of a serie of algorithms (those used for the analysis reported here will be described in detail later) written in FORTRAN, running on a farm

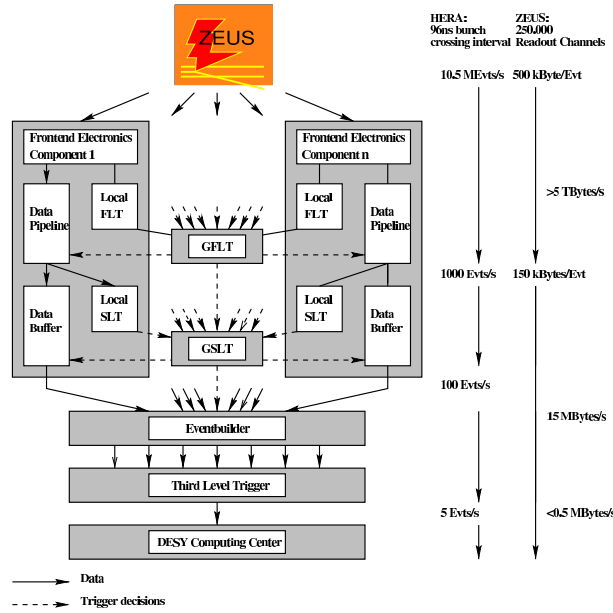


**Figure 3.14:** Schematic diagram of the ZEUS trigger and data acquisition system.

of SGI CPUs, where a partial event reconstruction is done. The analysis of the events is not parallel, but the events are distributed to all the CPUs of the farm. In addition to the reconstruction program, also some selection programs are run on the data, in order to select good *ep* events. The main information that the reconstruction program sends to the selection algorithms are the addresses and the energies of the calorimeter cells above threshold, and the parameters (momentum and position) of the tracks reconstructed by the CTD. The resolution on the energy and on the track parameters is lower than that obtained with the final reconstruction program.

After having accepted an event, the TLT sends the data via an optical link to the DESY computing centre, where the events are written to disk to be available for further offline reconstruction and data analysis.

A schematic view of the ZEUS trigger and data acquisition system is shown in Fig. 3.14.

### 3.3 ZEUS Detector Simulation

The events produced by the event generator contain the four-vectors of the final state particles. To compare simulated events to detector measurements, the influence of the individual detector components on the simulated final state has to be taken into account. The *detector simulation* takes care of this influences by tracing the hadron through the detector. The detector geometry including the sizes and materials of the different detector components and the dead material is implemented in *MOZART*<sup>1</sup> using the *GEANT* package [78]. *GEANT* takes care of simulating the detector response taking into account processes like energy loss, multiple scattering and in-flight particle decays.

The simulated detector measurements are subject to a subsequent trigger logic simulation by the *CZAR* package<sup>2</sup>.

Finally the simulated event is passed to the event reconstruction *ZEPHYR*<sup>3</sup> which is the same for simulated and recorded events.

---

<sup>1</sup>**MO**nTe Carlo for **ZEUS** Analysis **R**econstruction and **T**racking

<sup>2</sup>**C**omplete **Z**GANa Analysis **R**outine (*ZGANa*: **ZEUS** **GEANT** **AN**alysis was the first ZEUS detector simulation and was further developed to exclusively simulate the trigger logic)

<sup>3</sup>**ZEUS** **PHY**sics **R**econstruction



# Chapter 4

## Event reconstruction and data selection

In this chapter the details of the measurement are presented. The extraction of the kinematic variables  $x$ ,  $y$  and  $Q^2$  using different combinations of measured variables, such as the energies and angles of the scattered positron and hadrons, will be shown. The focus of this chapter will be on the methods used to select neutral current DIS events. First an introduction will be given on the reconstruction of the kinematic variables of the events. The chapter further explains which detector components are used to reconstruct the event. This will be followed by a discussion of the event selection criteria. This chapter ends with a comparison between the selected data and the Monte Carlo simulation results.

### 4.1 Kinematic reconstruction

The final state of a DIS event contains two distinct objects: the scattered positron and the hadronic system Fig. 4.1. The hadronic system combines everything that is not attributed to the scattered positron in one single object. The hadronic system can be further broken down into the current jet, which is the result of hadronisation of the struck quark, and the proton remnant.

The ZEUS detector is almost hermetic. This allows the measurement of four independent variables from information of the calorimeter and tracking:

- $E'_e$ , the energy of the scattered positron;

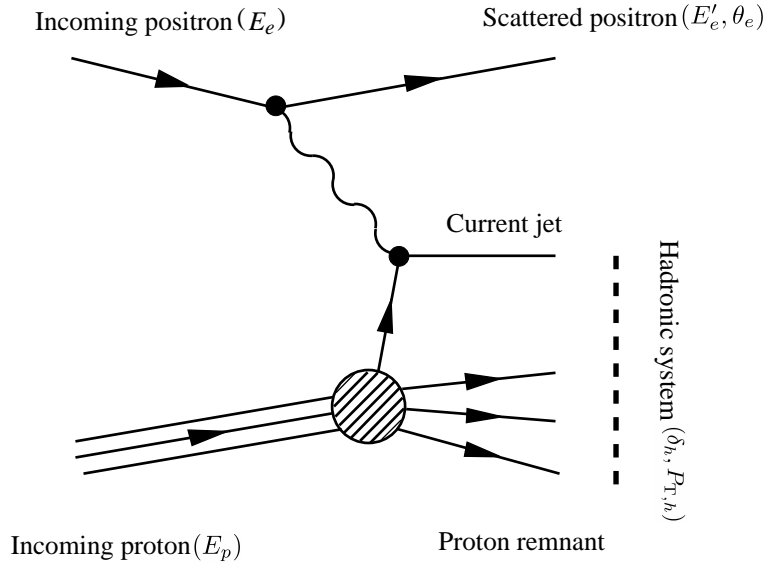


**Figure 4.1:** A schematic view of a DIS-Event. The initial state is, apart from initial state radiation, completely determined by the HERA-beam parameters.

- $\theta_e$ , the polar angle of the scattered positron;
- $\delta_h = \sum_i (E_i - p_{Z,i})$ , summed over all energy deposits in the calorimeter of the “hadronic system”, i.e. those not assigned to the scattered positron;
- $p_{T,h} = \sqrt{(\sum_i p_{X,i})^2 + (\sum_i p_{Y,i})^2}$ , the transverse momentum of the hadronic system.

Here  $p_{X,i}$ ,  $p_{Y,i}$  and  $p_{Z,i}$  are the X,Y,Z projections of the energy deposits, respectively. Together,  $\delta_h$  and  $p_{T,h}$ , provide information on the angle and energy of the hadronic system.

Two measured quantities are needed to fully reconstruct the event kinematics. This is because the interaction process is electron-quark scattering, a two body process with two degrees of freedom. Due to the ZEUS detector being almost hermetic, and therefore both the scattered positron and jet being detected, there are a number of possible choices as to which two are used. This is in contrast to fixed target experiments where it is not always possible to observe the complete final state. There are several popular choices, which are best suited to different kinematic regions. The optimal method in any one case depends on the kinematic region of interest, and upon the properties of the detector.

### 4.1.1 Electron method

The electron method reconstructs the kinematics solely from the electron information. This is the method used by most fixed target experiments, where often only the scattered lepton can be observed. The two quantities used for this are the corrected energy of the detected electron ( $E'_e$ ), and the angle of deflection that the electron undergoes ( $\theta_e$ ). In the electron method,  $x, y$  and  $Q^2$  are given by:

$$y_e = 1 - E'_e \frac{1 - \cos \theta_e}{2E_e} \quad (4.1)$$

$$Q_e^2 = 2E_e E'_e (1 + \cos \theta_e) \quad (4.2)$$

This method is used mostly for low and medium  $Q^2$  events, because it has the smallest bias and best resolution at lower  $Q^2$ . This method emphasises the importance of accurately measuring the angle and energy of the scattered electron. From this one can see the utility of the SRTD in improving the precision to which the kinematics are measured. The electron energy poses some problems due to the considerable amount of inactive material ( $1-5 X_0$ ) between the interaction region and parts of the calorimeter surface.

### 4.1.2 Jacquet-Blondel method [94]

As the UCAL is almost hermetic, most of the hadronic activity in the event is contained within the detector. This means that an analogous method to the electron method can be used for hadronic information. The hadronic angle and hadronic energy in the event is reconstructed similarly.

However the reality is not quite that simple. The struck quark does not transverse the detector as a single particle. Instead a collection of particles (termed the current jet) is observed. In addition, the separation of the current jet from the proton remnant is ambiguous due to the colour flow between them. To sidestep this tricky problem, a formula is constructed, based on inclusive event quantities, which permits the evaluation of the kinematics without separating these two contributions:

$$y_{JB} = \frac{\delta_h}{2E_e} \quad (4.3)$$

$$Q_{JB}^2 = \frac{p_{T,h}^2}{1 - y_{JB}} \quad (4.4)$$

However, as this is highly dependent on both containment of the event as well as the hadronic energy scale - both approximations - the resolution of this method is worse than the other 2 methods outlined here.  $Q_{JB}^2$  is particularly susceptible to long-range migrations. Only  $y_{JB}$  can be measured with good precision. Despite these limitations, the Jacquet-Blondel Method is of particular importance in CC ( $y_{JB}$  is also used in photoproduction) events, where the neutrino escapes detection. Here only the hadronic information is available, so there is no alternative method.

From equation 4.3,  $y_{JB}$  can also be seen to be a measure of the hadronic activity in the event.

### 4.1.3 Double angle method [95]

This method derives from the fact that angles are often measured with better accuracy than energies at HERA. This is because to first order the hadronic and electron angles are independent of the energy scale of the calorimeter. The hadronic angle, the estimate of the angle of the struck quark, is given by:

$$\cos \gamma = \frac{(\sum_h p_{X,h})^2 + (\sum_h p_{Y,h})^2 - (\sum_h (E - p_{Z,h}))^2}{(\sum_h p_{X,h})^2 + (\sum_h p_{Y,h})^2 + (\sum_h (E - p_{Z,h}))^2} = \frac{p_{T,h}^2 - \delta_h^2}{p_{T,h}^2 + \delta_h^2} \quad (4.5)$$

The kinematic variables are then given by:

$$y_{DA} = \sin \theta_e \cdot \frac{1 - \cos \gamma}{\sin \gamma + \sin \theta_e - \sin(\theta_e + \gamma)} \quad (4.6)$$

$$Q_{DA}^2 = 4E_e^2 \cdot \sin \gamma \frac{1 + \cos \theta_e}{\sin \gamma + \sin \theta_e - \sin(\theta_e + \gamma)} \quad (4.7)$$

This is in general the best reconstruction method for ZEUS, and provides very good reconstruction over a large proportion of the kinematic range accessible at HERA. However at medium  $Q^2$  and also at large  $y$ , the electron method outperforms the double angle method.

### 4.1.4 The $\Sigma$ method [96]

The  $\Sigma$  method is based on longitudinal momentum conservation,  $E - p_Z = 2E_e$ . The estimates of  $E - p_Z$  carried by the hadrons and electrons are  $\delta_{had} = E_h - p_{Z,h}$  and  $\delta_e = E'_e - p'_{Z,e}$  respectively. If some of the electron energy is lost due to Initial

State Radiation, the electron energy at the interaction is reduced to  $\tilde{E}_e = E_e - E_\gamma$ . Also  $E - p_Z$  is reduced to  $2\tilde{E}_e$  instead of  $2E_e$ .

The  $\Sigma$  method replaces the scale ( $2E_e$ ) in the calculation of  $y_{JB}$  by  $E - p_Z = E_h - p_{Z,h} + E'_e(1 - \cos\theta'_e)$ . This leads to

$$\begin{aligned} y_\Sigma &= \frac{E_h - p_{Z,h}}{E_h - p_{Z,h} + E'_e(1 - \cos\theta'_e)} \\ Q_\Sigma^2 &= \frac{E_e'^2 \sin^2\theta'_e}{1 - y_\Sigma} \end{aligned} \quad (4.8)$$

At small  $y$ , since the part of electron,  $E'_e(1 - \cos\theta'_e)$ , dominantly contributes the reconstruction by the  $\Sigma$  method, the variables are rather well measured. Though the hadronic part suffers from significant energy losses, this method corrects in part for this loss.

#### 4.1.5 The $J/\psi$ kinematic variables reconstruction

A kinematic variable specific for the studies of inelastic charmonium production is the inelasticity,  $z$ , which is the fraction of the virtual photon energy transferred to the  $J/\psi$  in the proton rest frame.

The inelasticity  $z$  was reconstructed using the expression

$$z = \frac{E_\psi - p_{Z,\psi}}{2 E_e y_\Sigma} \quad (4.9)$$

indeed from the definition  $y = (p \cdot q)/(p \cdot k)$  we have  $(p \cdot q) = y \cdot (p \cdot k)$  and hence  $z = (p_\psi \cdot p)/(q \cdot p) = 1/y(p \cdot p_\psi)/(p \cdot k) = y_\psi/y$  so we get (4.9)

if  $y_\psi$  and  $y$  are taken according to the Jacquet-Blondel method and  $\Sigma$  method respectively it is instructive also to substitute (4.8) into (4.9):

$$z = \frac{E_\psi - p_{Z,\psi}}{\frac{2E_e}{\delta} \sum_{had}(E - p_Z)}. \quad (4.10)$$

#### 4.1.6 For this analysis

The present analysis uses several of the presented reconstruction methods. The Jacquet-Blondel and electron methods are used to reject certain specific regions of phase space (see Sect. 4.8)

In the following, the electron method will be used for the reconstruction of  $Q^2$  and the  $\Sigma$  method for the reconstruction of  $y$ . This combination optimizes the  $Q^2$  resolution, while being insensitive to the initial photon radiation. The photon-proton centre-of-mass energy,  $W$ , is calculated from  $W^2 = ys - Q^2$ .

## 4.2 Event reconstruction

### 4.2.1 Track and vertex reconstruction

The CTD provides measurements of three-momenta of tracks which are also used to reconstruct the event vertex. The CTD tracks and the primary event vertex are reconstructed using the VCTRACK package [97] which is briefly described here.

At least three hits from the most outer axial superlayer are combined to form a “seed”, which is extrapolated inwards, guided by an additional “virtual hit” at  $x = y = 0$ . During the extrapolation more hits are gathered and added to the track candidate. The momentum and the direction of the track are determined at each step by fitting a helix to the hits. The entire procedure is repeated until all track seeds in the outermost superlayer are used, at which point it continues with the next inner superlayer. So the longest tracks are found first, and the shortest tracks last.

The vertex finding algorithm is described in detail in [98]. It is based on CTD tracks and can be separated in the following steps:

- Tracks that are incompatible with the intersecting beam-line are removed from the fit;
- Vertex “simple fit”: for the surviving tracks, the weighted center of gravity,  $(x, y, z)^{simple}$  is found. Tracks that contribute too much to the overall  $\chi_{simple}^2$  are discarded, one at a time, until the fit quality is acceptable. This vertex is the starting point for the full vertex fit.
- Vertex “full fit”: with the vertex from the simple fit, the final vertex position is determined. The remaining trajectories are constrained to this vertex, while at the same time, the direction and curvature are refitted. Tracks which extend into the innermost superlayer are candidates for primary-vertex tracks.

In this analysis only tracks which come from the primary vertex are used.

### 4.3 Reconstruction of the hadronic system

The reconstruction of the hadronic final state has previously relied on the energy deposits in the calorimeter. However there are circumstances when the information provided by tracking detectors is more precise, such as at low transverse momentum, or in the region around the gaps between calorimeters.

The energy resolution of the CAL (see Eqs. 3.4 and 3.5 in Sec. 3.2.2) is  $\sigma(E)/E \sim 1/\sqrt{E}$  and decreases for higher particle energies whereas at lower particle energies, the resolution of the track reconstruction (see Eqs. 3.2 in Sec. 3.2.1) gives a better energy estimate [86,87] (see Fig. 4.2).

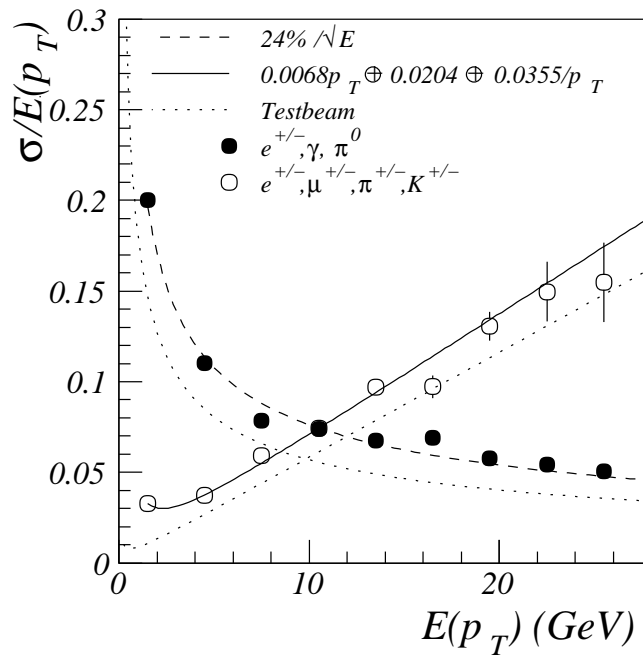


**Figure 4.2:** Resolutions from single particle MC simulations. The track transverse momentum resolution in the CTD (open markers) and the CAL energy resolution (closed markers) is shown[87].

To benefit from the most accurate energy determination in both energy ranges, the track reconstruction and the CAL energy measurement is combined to *energy flow objects* (EFO's). The track information is mainly used below 10-15 GeV and the calorimetric energy measurement above to form vectors representing the oriented energy deposition of particles traversing the detector.

### 4.3.1 Hadronic energy flow reconstruction

The philosophy of the energy flow algorithm [86, 87] is to use wherever possible the information from the tracking detectors to improve the measurement of energy deposits in the calorimeter. This is because the tracking detectors, being closer to the interaction point, suffer less from particle interactions with inactive material and also because the momentum resolution of the CTD is significantly better than the energy resolution of the calorimeter. The algorithm proceeds in three steps, calorimeter island finding, track matching and finally a detector choice between track or calorimeter information. As can be seen from figure 4.3, this ensures that all different “types” of particle are included in the reconstruction process with the highest possible accuracy.

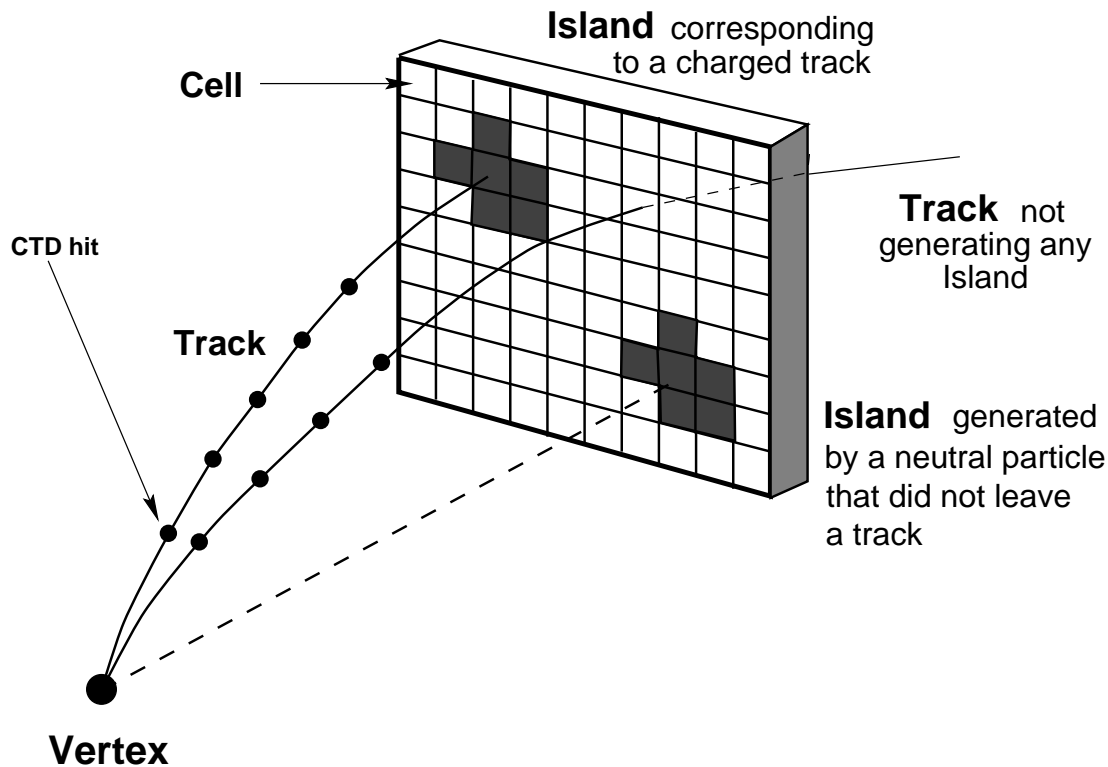


**Figure 4.3:** The different types of energy flow objects which can be formed using a combination of calorimeter and CTD information.

To ensure that the best possible quality data is used in this reconstruction method both noise suppression and calorimeter energy scale corrections must be

used before the algorithm is applied. Full details of this package can be found in [86], but an overview is given here and is referred to as the EFO (energy flow object) method. The first stage of the reconstruction process involves the formation of cell islands separately in the EMC, HAC1 and HAC2 sections of the calorimeter. Every calorimeter cell is assigned to a cell island. The position of the cell island is then determined from the logarithmically energyweighted average of the positions of all the constituent cells. Having established a set of cell islands, these are then joined to form cone islands. This is achieved by matching cell islands in the hadronic and electromagnetic sections of the calorimeter, based on their angular separation, starting from the outer hadronic sections and working inwards. EMC cell islands are then combined using a similar process. Once the linking of cell islands has taken place, the cone island information is generated by combining all calorimeter cells which point to the same EMC cell island. The algorithm implementation is shown in figure 4.4.

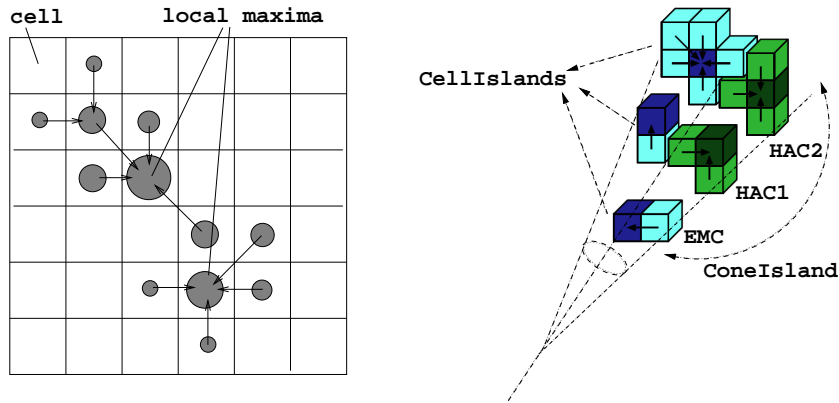


**Figure 4.4:** Left: Schematic diagram of the cell-island algorithm in two dimensions. Right: Schematic diagram of cell-islands combination to cone islands.

Once the cone islands have been formed, a set of high quality tracks must then also be selected for matching purposes. A track is considered to be of high quality if it has traversed at least three CTD superlayers and has  $0.1 < p_T < 20$  GeV. These tracks are then extrapolated to the face of the calorimeter and matched to a cone island, where possible. The distance between the track projection on the calorimeter surface and the cone island is used to determine if a track is matched to a cone island. The energy and momentum of these matched objects are then calculated using the following rules

- 1. If a track has not been matched to a cone island, then its energy is calculated using the momentum determined from the track under the assumption that the particle which produced the track was a pion.
- 2. If a cone island has not been matched to a track, then its energy and momentum are calculated by assigning a momentum vector  $\vec{p}$  to it such that  $E^2 = \vec{p}^2$ , where  $E$  is the energy measured by the calorimeter and  $\vec{p}$  has the direction from the reconstructed vertex to the cone island position.
- 3. If a cone island has more than three tracks associated to it, then its energy and momentum are calculated using the calorimeter information alone as in 2. above.

All other objects are then assessed to decide whether to use the calorimeter or CTD information associated to the object. The tracking information will be used in preference to the calorimeter information if

- $E/p < 1.0 + 1.2 \cdot \sigma(E/p)$ , where  $E$  is the calorimeter energy in GeV and  $p$  is the momentum in GeV measured by the CTD. The uncertainty is given by  $\sigma(E/p) = (E/p^2) \cdot \sigma(p) \oplus (1/p) \cdot \sigma(E)$ , where  $\sigma(p)$  and  $\sigma(E)$  are the resolutions of the momentum and the energy, respectively.
- and the resolution of the momentum measurement from the CTD is better than the resolution of the energy measurement from the calorimeter.

The first requirement ensures that the calorimeter energy is due only to the associated track ie. there are no extra neutral particles involved. The second requirement ensures that the highest possible accuracy is achieved. The objects which have been reconstructed are referred to as ZEUS Unidentified Flow Objects, or ZUFOs.

### 4.3.2 Corrections for the presence of muons

The reconstruction of the hadronic system of an event only from the CAL measurement would lead to an underestimation of the energy due to the presence of a muons. For a muon the energy loss while traversing the CAL is dominated by ionisation and therefore the measured energy is not proportional to and usually less than the momentum.

If EFO's are used to reconstruct the hadronic system, this effect is taken into account because EFO's favour the tracking information over the CAL measurement for a muonic energy signature in the CAL. This only works for semi-isolated muons.

The energy release of a muon in the CAL is parametrised as a function of the polar angle  $\theta$  using single muon MC simulations (see Fig. 4.5).

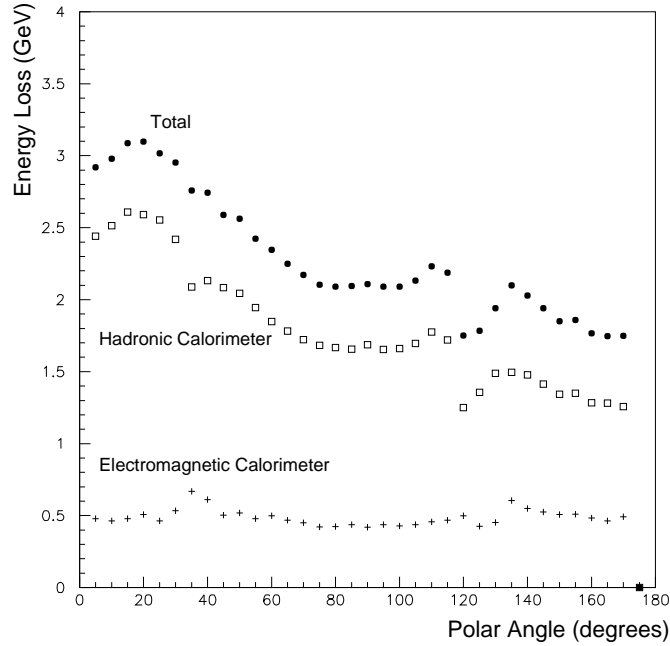


**Figure 4.5:** Energy loss of a muon in the CAL as a function of the polar angle  $\theta$  (full circles) and the energy fractions in the electromagnetic (crosses) and hadronic (open squares) calorimeter sections [88].

The hadronic system was corrected for the presence of muons in the following way: if a muon candidate track had hits in exactly three superlayers of the CTD then a muonic energy was subtracted from the hadronic four-vector and replaced with the tracking information (for a track with hits in more than three superlayers the EFO algorithm activates its own muon correction procedure). The subtracted muonic energy deposit was used either according to MV (see Sec. 4.5.2) muon finder information (when available) or from an angular dependent parametrisation (see Fig. 4.5).

## 4.4 Identification and reconstruction of the scattered lepton

### 4.4.1 Electron identification

The scattered electron is characterised by a localised energy deposition mainly in the electromagnetic part of the calorimeter with little energy leakage into the hadronic part. In contrast, hadronic showers are usually transversely much broader and longitudinally much deeper. In the analysis presented here, electron identification is done using *Sinistra95* [79–81]. This is a neural network based electron finder which has been trained on low  $Q^2$  NC data and Monte Carlo to produce the best separation between electromagnetic and hadronic clusters. The network is based on the calorimeter information using an algorithm similar to the cell island algorithm described above. It analyses the energy distribution in terms of lateral and longitudinal shower profiles.

The output from the neural network is a probability of a cluster to be the scattered electron. The probability varies from zero (cluster is of hadronic origin) to one (cluster seems from positron). According to [79] to obtain highly pure sample of scattered electrons, a cut on this probability  $P \geq 0.9$  has to be done. The identification efficiency of *Sinistra95* for electrons in the RCAL with energies above 10 GeV is greater than 90% and the purity is 98% [82]

The agreement between data and Monte Carlo is very good for an electron energy above 10 GeV. Studies of the electron finding efficiency, in data and MC, have been performed using elastic QED Compton events [86].

The main source of islands that are wrongly identified as a DIS electron are photons radiated off the initial state electron under large angles such that they hit the calorimeter. Also, electromagnetic showers from  $\pi^0 \rightarrow \gamma\gamma$  may fake an electron.

### 4.4.2 Electron position reconstruction

From the calorimeter cluster of the electron candidates, the impact position can be reconstructed. The position measurement and the event vertex are used to reconstruct the scattered electron polar angle  $\theta_e$ . In the  $Q^2$  range studied in this analysis the scattered electrons hit the RCAL under a small angle. In this region the tracks go through the RCAL and also RHES and SRTD detectors. They are

also used for position measurement. In Fig. 4.6 the resolutions of the scattering angle for SRTD, RHES and RCAL are presented.

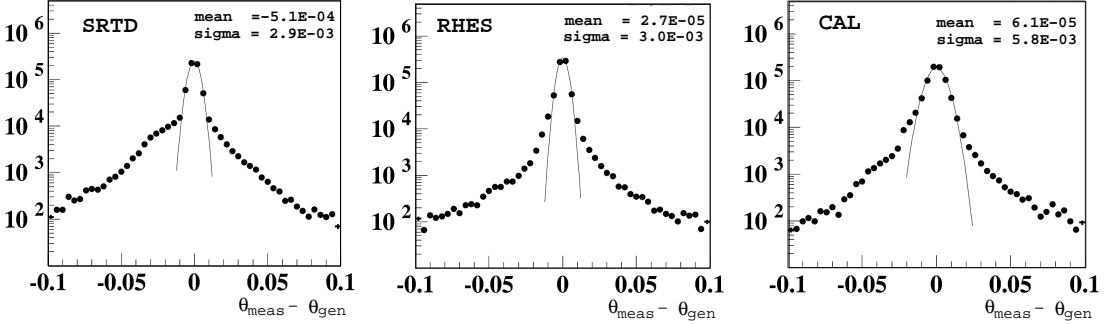


**Figure 4.6:** Angular resolution (in rad) for the scattered electron estimated with the DIS NC Monte Carlo sample as determined with different detector components [89].

A brief description of the reconstruction and the precision obtained with these detectors is given here.

- RCAL

The position of an energy deposit in a cell is determined in the  $y$  direction by the geometrical center of the cell (size  $20 \times 10 \text{ cm}^2$ ) while in  $x$  the energy imbalance measurement from the double-sided cell readout is used to correct the position (Sec. 3.2.2). Since the scattered electron shower spreads over several cells, the electron finder uses the weighted average of the positions of cells,  $\vec{r}_i = (x_i, y_i)$ , belonging to the electron deposit:

$$\vec{r} = \frac{\sum_i w_i \vec{r}_i}{\sum_i w_i} \quad (4.11)$$

where the weight  $w_i$  is proportional to the logarithm of the energy in the  $i$ -th cell,  $E_i$ . The resolution of the scattering angle for RCAL is  $\approx 5.8$  mrad (Fig. 4.6).

- RHES

The RHES has a diode size of 3 cm (see Sec. 3.2.5) which provides a better precision reconstruction [90, 91]. The reconstruction finds clusters based on a 3-by-3 diode array where the central diode has a signal  $> 5$  mips. The

position is calculated as a weighted average, using the logarithmic energy as weight. If more than one cluster is found the one which is closest to the SINISTRA position is taken. The resolution of the scattering angle for RHES is  $\approx 3$  mrad (Fig. 4.6).

- SRTD

The width of the SRTD scintillator strips is 1 cm in two layers which provides the highest precision in the position reconstruction. The reconstruction of the SRTD deposits proceeds in three steps [92]. In the first step in each layer all strips are clustered to one dimensional clusters (so-called X- or Y- cluster). The weighted sum of the positions of the strip with the highest energy and adjacent ones provides the X or Y measurement. In the second step the two layers are combined. The electron impact position is determined by the crossing of X- and Y-cluster. If more than one cluster is reconstructed in one or both layers all combinations are considered. Crossings where the vertical and horizontal cluster have similar energies are considered. In the reconstruction [93] the best electron candidate is determined by comparing the SRTD cluster position with the candidates from SINISTRA. The resolution of the scattering angle for SRTD is  $\approx 2.9$  mrad (Fig. 4.6).

#### 4.4.2.1 Choise between detectors

The scattering angle  $\theta_e$  was determined from the position measurement of the detector with best resolution.

- If SRTD has a good candidate the position measured with SRTD is used.
- If SRTD cannot provide a good candidate but RHES does, RHES determines the position of scattered electron.
- If neither SRTD nor RHES have good candidates the position determined by SINISTRA with RCAL is taken for the scattered electron

The fraction of events, where the position was determined with a specific detector is shown in Fig. 4.7 The data and Monte Carlo agree well.

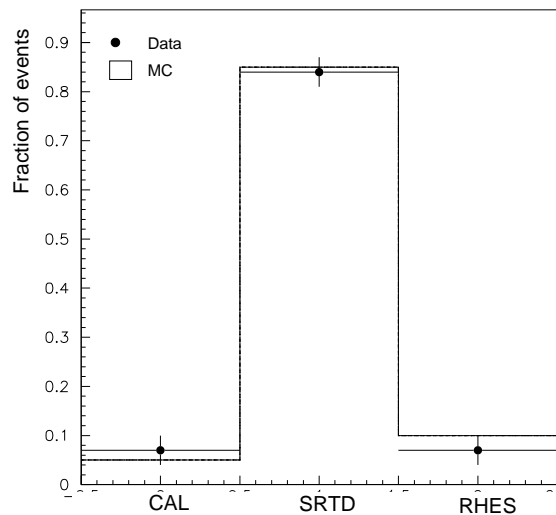


**Figure 4.7:** The fraction of events reconstructed using the SRTD, HES or RCAL.

## 4.5 Muon reconstruction

Muons, unlike electrons and hadrons, release only a small quantity of their energy in the calorimeter and are detected in the muon chambers. There are several muon finding algorithms based on the matching between the CTD track and the muon chamber track or between the CTD track and an energy deposit in the calorimeter compatible with a minimum ionizing particle (MIP).

Muons with energy greater than about 1.5 GeV can reach the ZEUS muon chambers - BRMUON detectors (see Sect. 3.2.3.2), and are identified by reconstructing tracks in the Muon Detector and linking them to tracks found in the inner tracking devices - the BREMAT[99] algorithm. For muon momenta above 0.8 GeV this method is complemented by the identification of muons as particles leaving the signature characteristic for minimum ionizing particles in the CAL(see Sect. 3.2.2) - the MV [100] algorithm.

### 4.5.1 The BREMAT matching package

The *Barrel and Rear Extrapolation MATching* package, BREMAT [99], is used to match segments reconstructed in the barrel and rear muon detectors to tracks

measured in the inner tracking detectors, mainly the CTD. The limited streamer tubes, and the associated strips, used in the BRMUON detector have a resolution of the order of  $\sim 1$  mm on both the coordinates they measure,  $x$  and  $y$  (see Sect. 3.2.3.2) but the momentum resolution for most of the muons is dominated by multiple scattering in the iron yoke placed between the inner and the outer chambers. The most powerful way to reconstruct muons in this context requires that measurement errors, multiple scattering and energy losses are correctly taken into account, and this is the technique used by BREMAT.

The main purpose of the algorithm is to find candidate muons, associating inner detector tracks to segments in the muon chambers and providing the resulting matching  $\chi^2$ . The main input to the algorithm is the MBXYSG table [101], containing the information on the reconstructed segments in the BRMUON chambers, and the VCTRHL table [97], containing the parameters of the tracks reconstructed by the inner detectors. When an entry in MBXYSG is found, i.e. a segment in the muon chambers, BREMAT looks for candidates to be associated to it in the VCTRHL table, i.e. between all the tracks reconstructed by the inner tracking devices, mainly the CTD. A loose preselection is done on VCTRHL tracks to be associated to MBXYSG segments:

- the momentum  $p$  of the track has to be  $p > 1$  GeV; this is a minimal request for tracks that have to cross all the calorimeter before being identified by the muon chambers;
- the polar angle  $\theta$  of the track has to be  $\theta > 20^\circ$  (better acceptance of the tracking detectors, mainly CTD; rejection of forward tracks);
- the track has to start from CTD superlayer 1 and to extend at least to superlayer 3 (see Sect. 3.2.1);
- the impact parameter of the track (see Sec. 3.2.1.1),  $D_H$ , has to be  $|D_H| < 10$  cm;
- the  $z$  coordinate at the point of closest approach has to be  $|z_H| < 75$  cm;
- $\chi_{\text{track}}^2/n.d.f. < 5$ ;
- $\Delta \leq 150$  cm,  $\Delta$  being the distance between a central point on the BRMUON segment and the straight line obtained by extrapolating the CTD track to the calorimeter entrance.

Tracks passing the preselection are extrapolated through the calorimeter using the GEANE [102] package. The extrapolation of the parameters and error matrix of the candidate track proceeds from the outer surface of the inner tracking devices, through the calorimeter up to a reference surface on the inner muon chambers, where matching is done. This surface is shaped as a prism, having one base on the rear chambers plane at  $z = -310.53$  cm, the other base lying on the forward end of the barrel chambers, at  $z = +450.0$  cm, and the side faces corresponding to the barrel sectors. The track extrapolation is done outward, starting from the inner region, for the best treatment of the low-momentum muons, which suffer big energy losses compared to their initial energy. With the GEANE package also tracks that completely loose their energy before reaching the chambers are simulated.

The output track parameters and error matrix at the reference surface are usually referred to as *predictions*. The predicted variables and error matrix are obtained in a convenient Cartesian parametrization, related to the local coordinate frame of each sector. The slopes of the track  $x'$  and  $y'$  are also given in order to determine the predicted direction of the particle. The fifth coordinate is the momentum of the particle  $Q/p$ , that can be measured by the BRMUON detector just in the case the muon reaches the outer chambers.

Naming  $\xi_{M_i}$  and  $\xi_{P_i}$ , respectively, the measured and the predicted track parameters at the reference surface, the residuals are defined as  $\delta_i = \xi_{M_i} - \xi_{P_i}$ . If the coordinate of the Cartesian parametrization are written as  $(x, y, x', y', Q/p)$  the matching  $\chi^2$  is given by:

$$\chi^2 = \sum_{i,j} S_{ij}^{-1} \delta_i \delta_j \quad (4.12)$$

where the sum goes from 1 to  $n = 4$  or 5, depending whether the momentum is included or not in the  $\chi^2$ , and  $S^{-1}$  is the inverse of the covariance matrix of the residuals:

$$S_{ij} = \sum_{k,l} T_{ik} (\sigma_{\text{track}}^2)_{kl} T_{lj}^T + (\sigma_{\text{random}}^2)_{ij} + (\sigma_{\text{BRMU}}^2)_{ij} \quad (4.13)$$

with  $k, l = 1, \dots, n$ ;  $T$  is the transport matrix, between the start and the stop of the swim,  $\sigma_{\text{track}}^2$  is the error matrix of the inner detector track,  $\sigma_{\text{random}}^2$  the error matrix due to multiple scattering and energy loss, and  $\sigma_{\text{BRMU}}^2$  the error matrix of the BRMUON segment from the MBXYSG table. The first two terms are

calculated by steps during the GEANE extrapolation using the detailed geometry of the ZEUS detector and the magnetic field map. BREMAT makes a loose cut on the matched tracks, considering as matching the tracks having  $\chi^2 < 100$ .

### 4.5.2 The MV muon finder

The MV algorithm uses the MIP signature of a muon in the CAL to reconstruct muons. The reconstruction depends on the combination of CAL cell patterns to *clusters* of energy depositions. A two step procedure first forms islands starting from the most energetic CAL cell (seed). All neighbouring cells with non-zero cell content are associated to the island if the direct connection between the seed and the cell crosses only adjacent cells and consists only of cells with non-zero cell content. The associated cells of the island are marked and the island combination is repeated ignoring the marked cells. The centers of the resulting islands are calculated as the energy weighted sum of the corresponding cell clusters after a correction using the imbalance of the two photomultiplier measurements per cell. For the muon identification, the islands are clustered taking into account that muons originate from the interaction vertex. A cluster contains all island cells whose centers are inside a cone of  $2\alpha$  around the connection of the primary vertex and the island center. The clustering starts from the most energetic island and is repeated for all reconstructed islands. The angle  $\alpha$  increases from  $0^\circ$  at the normal direction of the incoming particle to  $6^\circ$  when the inclination of the particle trajectory to the CAL surface is  $45^\circ$ . This interval of  $\alpha$  is caused by the geometrical structure of the CAL consisting of boxes. The clustering step also combines islands from different part of the CAL to one energy cluster.

The MV finder reconstructs muons from the CAL energy clusters using the *phase space probability function*(PSPF) method [100]. From the cluster reconstruction, eight input variables per cluster are chosen containing the polar  $\theta$  and azimuthal  $\phi$  angle of the cluster, the energy contents in the electromagnetic and hadronic sections of the CAL (Sec. 3.2.2)  $E_{EMC}, E_{HAC1}, E_{HAC2}$  and the number of associated cells in the section  $N_{EMC}, N_{HAC1}, N_{HAC2}$ . These variables form an eight-dimensional phase space which is divided into a grid of phase space regions equidistant in the eight variables.

Muons have a small probability of a big energy deposition. Fig. 4.8 shows the energy deposition distribution and the number of cells with a signal in muon

cluster for different sections of the CAL [100]. The distributions obtained using a MC muon sample with energies 1-40 GeV. The simultaneous usage of cuts  $E_{EMC} < 1.54$  GeV,  $E_{HAC1} < 3$  GeV,  $E_{HAC2} < 3$  GeV,  $N_{EMC} < 5$ ,  $N_{HAC1} < 4$ ,  $N_{HAC2} < 2$  leaves 96.0% of muons and rejects 77.4% of hadrons.

The reconstructed CAL clusters of separate MC samples of muons and hadrons are used to calculate probability density functions for each grid bin. The probability densities are later used to distinguish muon clusters from other clusters. The probability can also be used to qualify reconstructed muons.

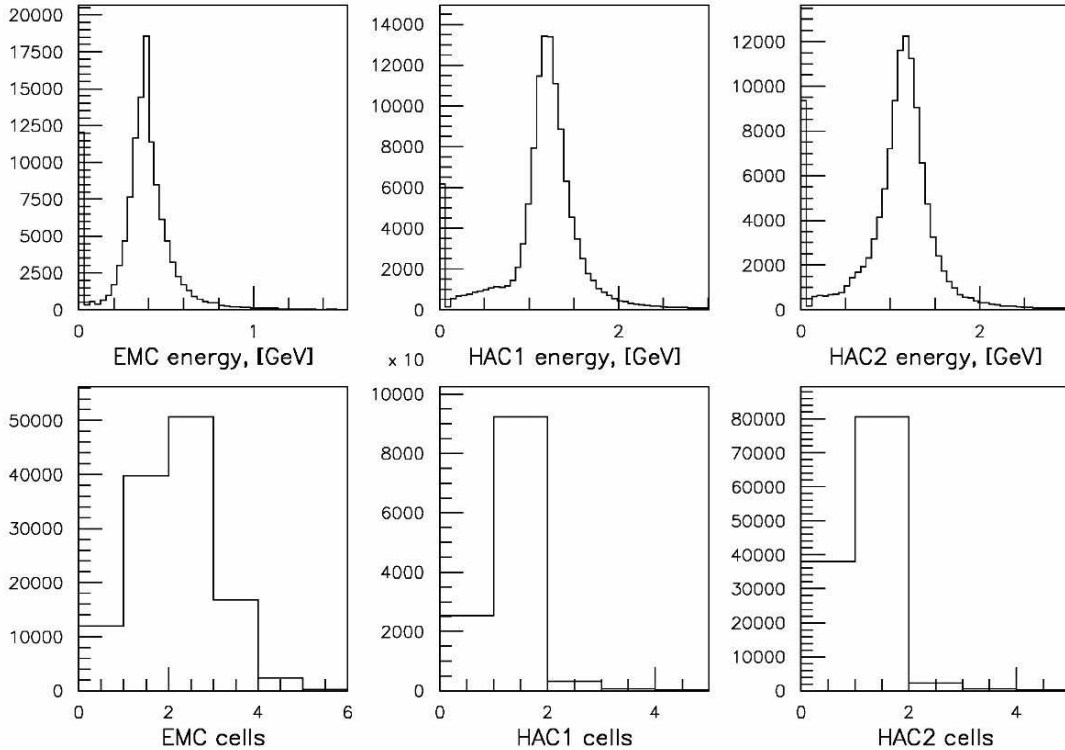


**Figure 4.8:** The energy deposition and the number of cells with a signal in muon cluster for different sections of CAL. [100]

The reconstructed muon is then matched using a *distance-of-closest-approach* (DCA) method.

MV has a good geometrical coverage and a low momentum threshold. The PSPF method results in an efficiency of 90% at purity of 97.5% but suffers from large hadronic background at low momenta.

## 4.6 $E - p_Z$ cut

One of the most useful cuts for selecting NC DIS events and rejecting backgrounds is the ‘ $\delta$ ’ or ‘ $E - p_Z$ ’ cut. The  $E - p_Z$  cut is a cut on the longitudinal energy and momentum conservation. The motivation behind this cut is to find an alternative to simply applying energy conservation to the measured quantities in the event. This cannot be used in ZEUS because generally in an event a large part of the proton remnant or the current jet disappears undetected down the beampipe. So, in any given event a fair proportion of the longitudinal momentum may be undetected. However the  $P_t$  of the lost particles is  $\approx 0$ .

The effect of this energy loss down the beampipe can be minimised by using instead the difference between the total energy and the longitudinal momentum measured in the event. This should be conserved between the initial and final states. This is a sum of the quantity,

$$\delta \equiv E - p_Z = \sum_i (E_i - p_{Zi}) \quad (4.14)$$

with  $i$  here being the sum over all final state particles detected. This is easily measurable by summing over all the energy deposits in the calorimeter.

In DIS events, where the scattered positron is detected in the main detector, this is an exactly conserved quantity. It is expected to be peaked at  $2E_e$ . This can be seen for a fully contained  $ep$  event, where  $\delta^{final\ state} = \delta^{initial\ state}$  and neglecting particle masses:

$$E - p_Z = (E - p_Z)_p + (E - p_Z)_e = (E_p - E_p) + (E_e - (-E_e)) \quad (4.15)$$

$$\approx 2E_e = 55 \text{ GeV} \quad (4.16)$$

As can be seen above, the contribution of the incoming proton and also of the outgoing remnant in the forward direction is  $\approx 0$ , because the energy is approximately equal to the momentum in the forward direction. So,  $E - p_Z$  is relatively insensitive to losses in the forward region, but very sensitive to losses in the rear direction, i.e. high  $y$  hadrons and ISR photons.

This cut is very good at rejecting photoproduction events and proton-beam gas events which are peaked at low values of  $E - p_Z$ , typically well below 30 GeV.

However ISR events, where the incoming positron has emitted a photon which is lost down the RCAL beampipe, migrate to lower values of  $E - p_Z$ . This is

because the photon is typically emitted almost parallel to the incoming positron beam and hence is undetected in the main detector. As seen from above,  $E - p_z$  is especially sensitive to losses in the rear direction. These DIS events may be lost by a tight cut on  $E - p_z$ .

## 4.7 Trigger chain for online data selection

The selection of the final event sample consists of two main steps. Events are first preselected by the three levels of the ZEUS trigger (see Sect. 3.2.7). Successively, an offline selection is applied, which benefits from higher precision after the final event reconstruction.

The trigger selection used is based upon that used in the inclusive DIS NC analysis [103] with extra muon requirement. This is highly advantageous in that this trigger chain has been extensively studied over a number of years. It is therefore well understood, and its description in the detector simulation is good.

The ZEUS three-level trigger for neutral current DIS events is mainly designed to select events with the scattered electron which is detected in the calorimeter.

### 4.7.1 First and second level trigger

Already at the FLT it is possible to select candidates of neutral current DIS interactions by checking energy thresholds in the calorimeter. Different requirements have to be fulfilled depending on the calorimeter section:

- If the electron is scattered into the RCAL, the event is accepted if the energy in the electromagnetic section is larger than 3.37 GeV. The event is also accepted if the energy deposited outside the inner calorimeter ring (60x60cm) is greater than 3.4 GeV.
- If the electron is scattered with  $36.7^\circ < \theta_e < 129.1^\circ$  it is detected by deposition in the BCAL section. In this case events are accepted if one of the energy electromagnetic section is larger than 2.78 GeV. Since the electron always traverses more than 3 superlayers of the CTD a track is required in addition. This requirement reduces the background from beam halo muons characterized by energy deposits in the BCAL without a track in the CTD.

- The trigger strategy for electrons scattered in the FCAL is based on transverse energy requirements. This allows to achieve a high trigger efficiency in a section which has to cope with high background due to large energy deposits in the forward region. The latter are caused by the proton remnant or the color flow between the proton and particles produced in the hard scattering. This section corresponds to events at very high  $Q^2$ .

By the help of the timing information of upstream veto counters and the SRTD, the background events from the interaction of protons outside the detector are rejected.

At the second level trigger (SLT) the background is further reduced by requiring cuts on the energy and timing of the calorimeter. In DIS events particles are emitted from the interaction point and arrive at FCAL and RCAL at times defined as  $t \approx 0$ . Proton beam related background events, however, deposit energy in the RCAL about 10 ns earlier. This provides an effective handle to reject background events. The time difference between the energy deposit in the upper and the lower half of the calorimeter is used to reject cosmic muon events which in contrast to  $ep$  interaction events deposit energy in the upper half of the detector first.

At the SLT level,  $E - p_Z = \sum_i^{all} (E_i - p_{Z,i})$  is calculated as a sum over all calorimeter cells assuming a nominal interaction point at  $X = Y = Z = 0$ . If the detector fully contains all information after interaction and has a perfect resolution, it could be estimated using the initial beam energy as  $E - p_Z = (E - p_Z)_p + (E - p_Z)_e = E_p - E_p + E_e - (-E_e) = 2E_e$  due to the momentum conservation (see Sect. 4.6). While particles escaping through the forward beam hole do not affect  $E - p_Z$  due to  $p_T \sim 0$ , any particle lost by the rear beam hole makes  $E - p_Z$  decrease by two times its energy. An example is photoproduction events which lose the scattered electron in the rear beam hole and therefore  $E - p_Z = 2E_e - 2E'_e$ . Thus a cut on  $(E - p_Z)$  can be used to suppress photoproduction background.

In order to keep DIS events with an ISR photon escaping through the rear beam hole and hitting the LUMI photon detector the cut on the SLT level is

$$E - p_Z + 2E_\gamma > 29 \text{ GeV} \quad (4.17)$$

where  $E_\gamma$  is the energy measured in the LUMI photon detector.

### 4.7.2 Third level trigger

The third level trigger (TLT) takes events, if the electron energy measured by any of the 4 electron finders, SINISTRA [79–81], EMILLE [104], LOCAL and ELEC5 [105, 106] is more than 4 GeV.

The energy of electrons hitting the calorimeter very close to the RCAL beam hole cannot reliably be measured since the electromagnetic shower is not fully contained in the calorimeter. Due to the  $Q^{-4}$  dependence of the cross section the rate of such events is very high. Therefore, the electron is required to hit the calorimeter outside the region  $|X| < 12$  cm and  $|Y| < 6$  cm.

At the TLT level,  $E - p_Z$  is re-calculated using the vertex measured by the CTD and the following cut is imposed

$$E - p_Z + 2E_\gamma > 30 \text{ GeV} . \quad (4.18)$$

In addition tighter timing cuts as well as sophisticated algorithms in order to reject beam-halo and cosmic muons are applied.

In this analysis a dedicated TLT algorithm has been used in order to select NC DIS events with a muon. The algorithm implements a fast muon finder based on the matching of CTD tracks and BRMUON segments. It requires a reconstructed vertex, at least one segment in the internal muon chambers and at least one track in the CTD satisfying the following requirements:

- $p_{track} > 1$  GeV;
- $\theta_{track} < 20^\circ$ ;
- the track must traverse at least the first three superlayers of the CTD;
- the distance of closest approach with respect to the beam line must be smaller than 10 cm;
- the distance between the point of closest approach and the primary vertex along the z-axis must be smaller than 10 cm.

The last two requirements reject cosmic muons traversing the detector far away from the reconstructed primary vertex. The matching between the muon segment and the CTD track is obtained if the distance between the extrapolated CTD track from the CTD exit point to the muon chambers and the muon segment is less than 200 cm.

### 4.7.3 The data samples

The data sample used in the analysis corresponds to an integrated luminosity of  $108.8 \pm 2.2 \text{ pb}^{-1}$  out of overall  $121.2 \text{ pb}^{-1}$  [107] collected in the years 1996–2000. Runs with bad performance of barrel and rear muon chambers (see Sect. 3.2.3.2) were excluded from the sample according to the MBTAKE utility[108]. The sample includes two subsamples (1996–1997 and 1998–2000) with different centre-of-mass energies,  $\sqrt{s} = 300 \text{ GeV}$  ( $\mathcal{L}_{300} = 32.7 \pm 0.6 \text{ pb}^{-1}$ ) and  $318 \text{ GeV}$  ( $\mathcal{L}_{318} = 76.1 \pm 1.6 \text{ pb}^{-1}$ ) and both positron- and electron-beam data.

running period	hadron	lepton	luminosity [ $\text{pb}^{-1}$ ]
1996-1997	$p$	$e^+$	32.70
1998-1999	$p$	$e^-$	15.89
1999-2000	$p$	$e^+$	60.17

**Table 4.1:** HERA running conditions and integrated luminosities taken with ZEUS and considered in this analysis.

## 4.8 Offline data selection

The event sample selected by the trigger still contains a fraction of background processes which are removed by applying tighter offline cuts. In addition, a precise reconstruction of the final state is only possible at the offline level. Further selection cuts are applied offline to the sample resulting from the online trigger selection. First a set of general cuts is applied to ensure a deep inelastic electron-proton scattering event has taken place. In addition a reconstructed  $J/\psi$  meson is required.

### 4.8.1 Selection of the neutral current DIS event sample

The following cuts are applied to select the sample of neutral current DIS events:

- The quantity  $(E - p_z)$  introduced in Section 4.6 is required to be within the range of  $40 < (E - p_z) < 65 \text{ GeV}$ . Figure 4.9 shows the comparison of data and MC simulation for the  $(E - p_z)$  variable. The vertical lines indicates the cut on this variable. The lower cut removes photoproduction

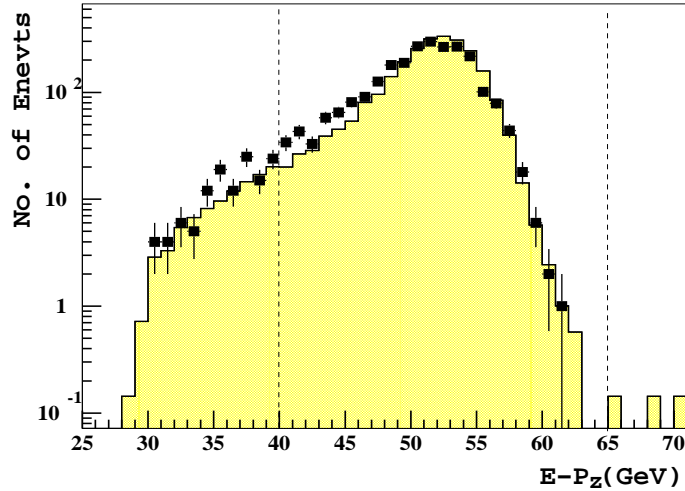


**Figure 4.9:** Comparison of the  $(E - p_z)$  distributions after all selection cuts for the data and the EPJPSI MC. The vertical lines show the range selected for this analysis. The MC sample was normalized to the number of events in data between  $(E - p_z)$  values of 50 and 60 GeV.

events which have a lower value of  $E - p_z$  compared to that of DIS events because the scattered electron escapes in the beam-pipe hole of the rear calorimeter; the lower cut also removes proton beam-gas interactions. The upper cut removes cosmic events superimposed on normal  $ep$  events;

- $|Z_{\text{vertex}}| \leq 50$  cm: the reconstructed  $z$ -position is restricted. The main reason is that the acceptance of the CTD and the calorimeter is best understood for events occurring in the central region of the detector. Furthermore, the vertex determination is more precise in the central region. A minor aspect is that beamgas events are randomly distributed in  $Z$  with the consequence that the fraction of beamgas events is larger outside the main vertex peak. Figure 4.10 shows the comparison of data and Monte-Carlo simulation for the  $z$  vertex position after all selection cuts except the cut on the vertex position.
- To ensure a high purity the electron candidate is required to have an energy of at least 10 GeV (see Section 4.4.1). For lower electron energies the efficiency drops to 50%. In addition a fiducial cut is applied to the electron position. The impact position of the scattered lepton on the inner

face of the rear calorimeter (RCAL) had to lie outside the box defined as  $|X| < 13$  cm and  $|Y| < 7$  cm (“box cut”) to ensure full containment of the electromagnetic shower (Detailed studies are done in [87]);

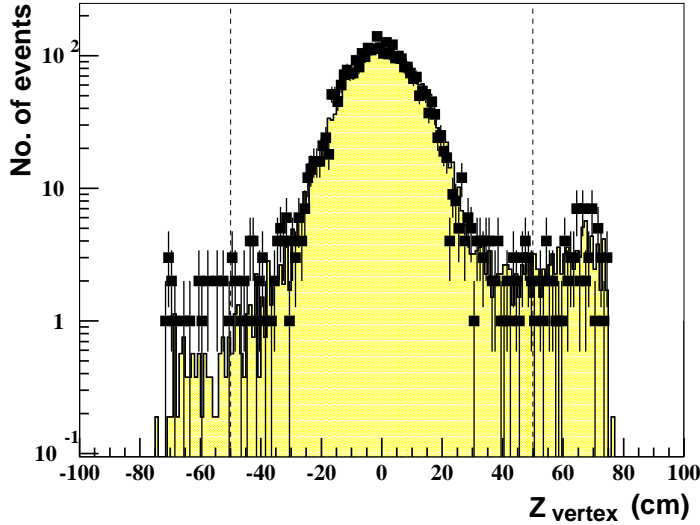


**Figure 4.10:** Comparison of the  $Z_{vertex}$  distributions after all selection cuts for the data and the EPJPSI MC. The symbols are the same as in Figure 4.9.

### 4.8.2 $J/\psi$ reconstruction

$J/\psi$  mesons are detected via the decay  $J/\psi \rightarrow \mu^+ \mu^-$  (branching fraction of  $5.88 \pm 0.1\%$  [109]). The muons from the  $J/\psi$  decays are reconstructed as two oppositely charged particles in the CTD. The correct identification of the muons is essential as the muon mass is used in the invariant mass calculation according to the formula:

$$M_{inv} = \sqrt{(E_{\mu^+} + E_{\mu^-})^2 - (\vec{p}_{\mu^+} + \vec{p}_{\mu^-})^2} \quad (4.19)$$

where  $\vec{p}_i$  and  $E_i$  are the momentum vectors and energies of the muons  $i = \mu^+$  or  $i = \mu^-$ . The energy is calculated using the momentum of the track:  $E_i = \sqrt{\vec{p}_i^2 + m_\mu^2}$

Each track considered in the analysis was required to be fitted to the event vertex, to reach at least the third superlayer of the CTD (this roughly corresponds

to the polar angle cut  $17^\circ < \theta < 163^\circ$  or pseudorapidity range  $|\eta| < 1.75$ ) and to have the transverse momentum  $p_T > 100\text{MeV}$  ; this guarantees good reconstruction quality.

One of the  $J/\psi$  decay tracks had to match a segment in the inner muon chambers . The BREMAT package [99] was used to perform the match using an extrapolation technique to trace a track reconstructed in the CTD through the CAL volume up to the surface of the inner muon chambers (B/RMUI). The 4-degrees-of-freedom probability calculated with BREMAT was required to be  $\mathcal{P}(4\text{-dof}) > 0.01$ .

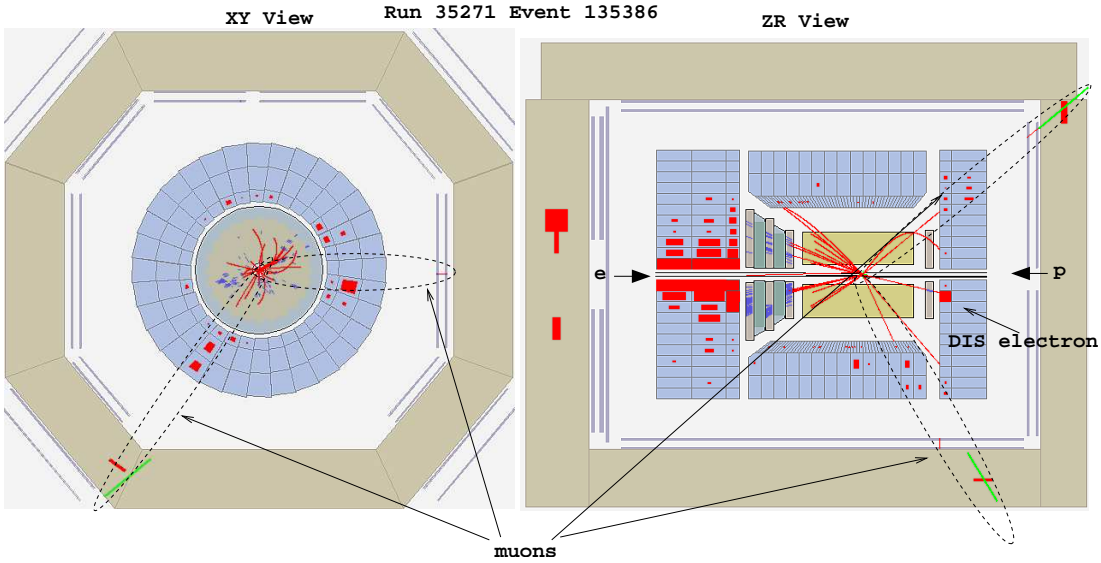


**Figure 4.11:** A candidate event for inelastic  $J/\psi$  production in DIS, shown in the side view (left), radial view (right) of the ZEUS detector. The invariant mass of the  $\mu^+\mu^-$  pair is  $3.08\text{ GeV}$ ,  $Q^2 = 20.7\text{ GeV}^2$ ,  $W = 208\text{ GeV}$ ,  $z = 0.45$ .

To ensure high muon-identification efficiency and purity, the track matched with the segment in the barrel (rear) inner muon chambers was required to have  $p_T > 1.4\text{ GeV}$  ( $p > 1.8\text{ GeV}$ , where  $p$  is the track momentum) [119]. Another  $J/\psi$  decay track had to match a cluster in the calorimeter (CAL) with an energy deposit consistent with the passage of a minimum ionising particle (m.i.p.). This is done using the MV muon finder which implements the phase space probability method [100]. The probability (so called ‘‘CAL probability’’, i.e. no information from the muon chambers was accounted for in its calculation) calculated with MV

was required to be  $\mathcal{P}(\text{CAL}) > 0.4$ . The cut on the momentum of the matched track was  $p > 1 \text{ GeV}$ .

Figure 4.11 shows an inelastic  $J/\psi$  production candidate in the ZEUS event display.

### 4.8.3 Kinematic cuts

The kinematic cuts determine the kinematic range analyzed and can be directly reconstructed from the four-momentum of the virtual photon.

- $y_{el} \leq 0.95$ : an upper cut on Bjorken  $y$ , reconstructed with the electron method, removes fake electron candidates (mostly highly energetic pions in the FCAL decaying into two photons). It also improves the electron finding efficiency for low energy electrons;
- $y_{JB} \geq 0.02$ : a lower cut on the Bjorken  $y$ , reconstructed with the Jacquet-Blondel method, ensures sufficient energy in the hadronic system. (Reconstructed with hadronic variables, it scales directly with the hadronic  $E - p_z$ ). The cuts serve preselection purposes. They are superseded by harder cuts that define the kinematic region of the analysis (for example cuts on  $E'_e$  and  $Q^2$  restrict  $y_e$ );
- The photon virtuality,  $Q^2$ , was reconstructed from the polar angle and energy of the scattered electron and was required to be in the range  $2 < Q^2 < 80 \text{ GeV}^2$ . The lower cut is applied because of the steeply falling acceptance for low values of  $Q^2$  due to the beam-pipe hole in the RCAL. The upper cut introduced because of the decreasing statistics for  $Q^2 > 80 \text{ GeV}^2$ .
- The Bjorken variable,  $y = (p \cdot q)/(p \cdot k)$ , where  $p$ ,  $q$  and  $k$  are the four-momenta of the incoming proton, exchanged photon and incoming electron, respectively, was reconstructed with the  $\Sigma$  method. Monte Carlo studies showed this method to be the most precise in the selected phase space region. The photon-proton centre-of-mass energy,  $W$ , calculated from  $W^2 = y s - Q^2$ , was restricted to the range  $50 < W < 250 \text{ GeV}$ .

The kinematic region accessible to the analysis is mainly restricted by the requirement of a reasonably high acceptance. Figure 4.12 shows the distributions

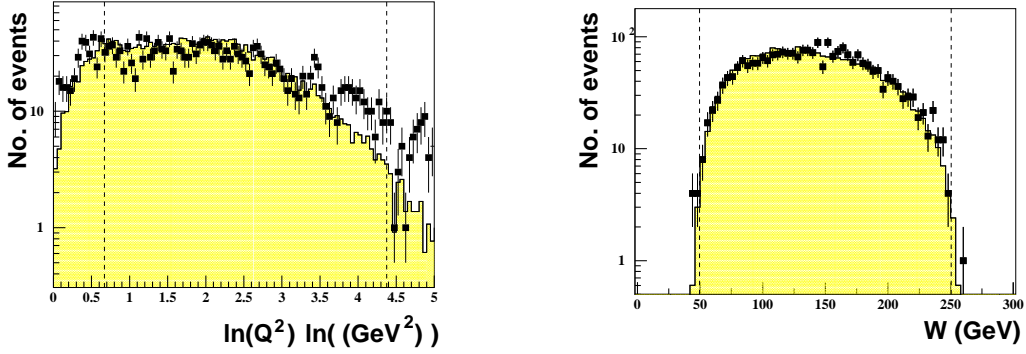


**Figure 4.12:** Distribution of the kinematic variables  $Q^2$  and  $W$  for the event sample after all selection cuts, compared to the Monte-Carlo simulation.

for the kinematic variables  $Q^2$  and  $W$  after all selection cuts. The analysis is restricted to the kinematical ranges indicated by the vertical lines in Figure 4.12.

The  $J/\psi$  rapidity in the laboratory frame, defined as

$$Y_{lab} = 1/2 \ln[(E_{\psi} + p_{Z,\psi})/(E_{\psi} - p_{Z,\psi})] \quad (4.20)$$

where  $E_{\psi}$  and  $p_{Z,\psi}$  are the energy and longitudinal momentum of the  $J/\psi$  meson, was limited to the region  $-1.6 < Y_{lab} < 1.3$ , where the acceptance is high.

A kinematic variable specific for the studies of inelastic charmonium production is the inelasticity,  $z = (p_{\psi} \cdot p)/(q \cdot p)$ , which is the fraction of the virtual photon energy transferred to the  $J/\psi$  in the proton rest frame. It is sensitive to the various production mechanisms. Color singlet (CS) processes are expected to contribute to the region of medium  $z$  values, whereas color octet (CO) (and diffractive) processes populate the high- $z$  region [122].

Previous HERA data [31, 32] have shown that the diffractive process populates the high- $z$  region,  $z > 0.9$ . The direct and resolved photon processes are expected to dominate in the regions  $0.2 \lesssim z < 0.9$  and  $z \lesssim 0.2$ , respectively [123]. At low (and medium)  $z$  contributions from  $B$ -decays ( $b \rightarrow J/\psi + X$ ) and cascade decays of higher mass charmonium states are also expected. In DIS the resolved-photon and diffractive processes are expected to be suppressed [123], but still they may provide significant contributions in some regions of phase space. So the inelasticity of  $J/\psi$  was restricted to the range  $0.2 < z < 0.9$ . The lower  $z$  cut removes the region of high non-resonant background due to fake muons and

(marginal) resolved-photon contributions. The upper  $z$  cut removes elastic and suppresses proton dissociative events.

#### 4.8.4 Further inelastic events selection

In order to further suppress the proton dissociative admixture the following cuts were applied:

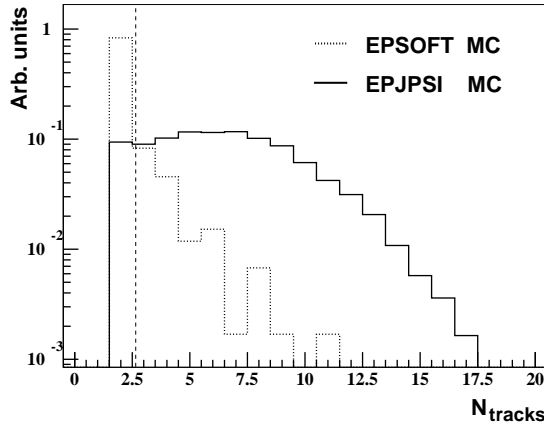


**Figure 4.13:** Distributions of the  $N_{\text{tracks}}$  for diffractive (EPSOFT) and non diffractive (EPJPSI) Monte-Carlo simulations after all selection cuts.

- the analysis was restricted to events with an energy deposit greater than 1 GeV in a cone of  $35^\circ$  along the outgoing proton direction (excluding calorimeter deposits due to the decay muons) [119]. This is because only diffractive events with a high enough invariant mass of the final state hadronic system have a visible energy deposit along the outgoing proton direction while the diffractive cross section is sharply peaked towards low invariant mass values (see Eqs. 4.22 )
- in addition to the tracks associated to the two muons and the track associated to the scattered lepton (if any), the event was required to have at least one track (“track multiplicity” cut). Figure 4.13 shows the comparison of “track multiplicity” distributions for EPSOFT and EPJPSI Monte-Carlo.

The residual contribution of the diffractive background was estimated using the Monte Carlo (MC) simulation (see Section 5.1).

Sample	Cut
DIS neutral current	$ Z_{\text{vertex}}  \leq 50$ cm $40 < \delta < 65$ GeV $E'_e > 10$ GeV box cut 13x7 cm
kinematic region	$y_{el} \leq 0.95, y_{JB} \geq 0.02$ $2 < Q^2 < 80$ GeV <sup>2</sup> $50 < W < 250$ GeV
$J/\psi$	$-1.6 < Y_{\text{lab}} < 1.3$ $0.2 < z < 0.9$
inelastic events selection	$E_{\text{CAL}}(\theta < 35^\circ) > 1$ GeV $N_{\text{tracks}} \geq 3$

**Table 4.2:** Summary of the main offline selection cuts

#### 4.8.5 Summary of the offline selection cuts and $J/\psi$ signal

In this section we have described the selection cuts applied in this analysis. The main cuts are summarized in the table 4.2

Figure 4.14 shows the invariant mass,  $M_{\mu^+\mu^-}$ , distribution of all selected muon pairs. The distribution was fitted in the intervals  $2.5 < M_{\mu^+\mu^-} < 3.6$  GeV and  $3.8 < M_{\mu^+\mu^-} < 4.5$  GeV with a function taken to be the sum of a “modified” Gaussian, to describe the signal, and a linear function, to describe the non-resonant background. The range  $3.6 < M_{\mu^+\mu^-} < 3.8$  GeV was excluded to avoid any overestimation of the background due to the  $\psi'$  state. The modified Gaussian function had the form:

$$\text{Gauss}^{\text{mod}} \propto \exp[-0.5 \cdot x^{1+1/(1+0.5 \cdot x)}] \quad (4.21)$$

where  $x = |(M_{\mu^+\mu^-} - M_0)/\sigma|$ . This function was introduced to take into account the non-Gaussian tails of the resonant signal. This functional form describes both data and MC signals well. The position of the Gaussian,  $M_0$ , the signal width,  $\sigma$ , as well as the number of signal events were free parameters of the fit. The fit yielded a peak position of  $M_0 = 3098 \pm 3$  MeV, in agreement with the PDG value [109], and a width of  $\sigma = 35 \pm 3$  MeV, in agreement with the MC estimation of the detector resolution. The number of  $J/\psi$  mesons was  $334 \pm 25$ .

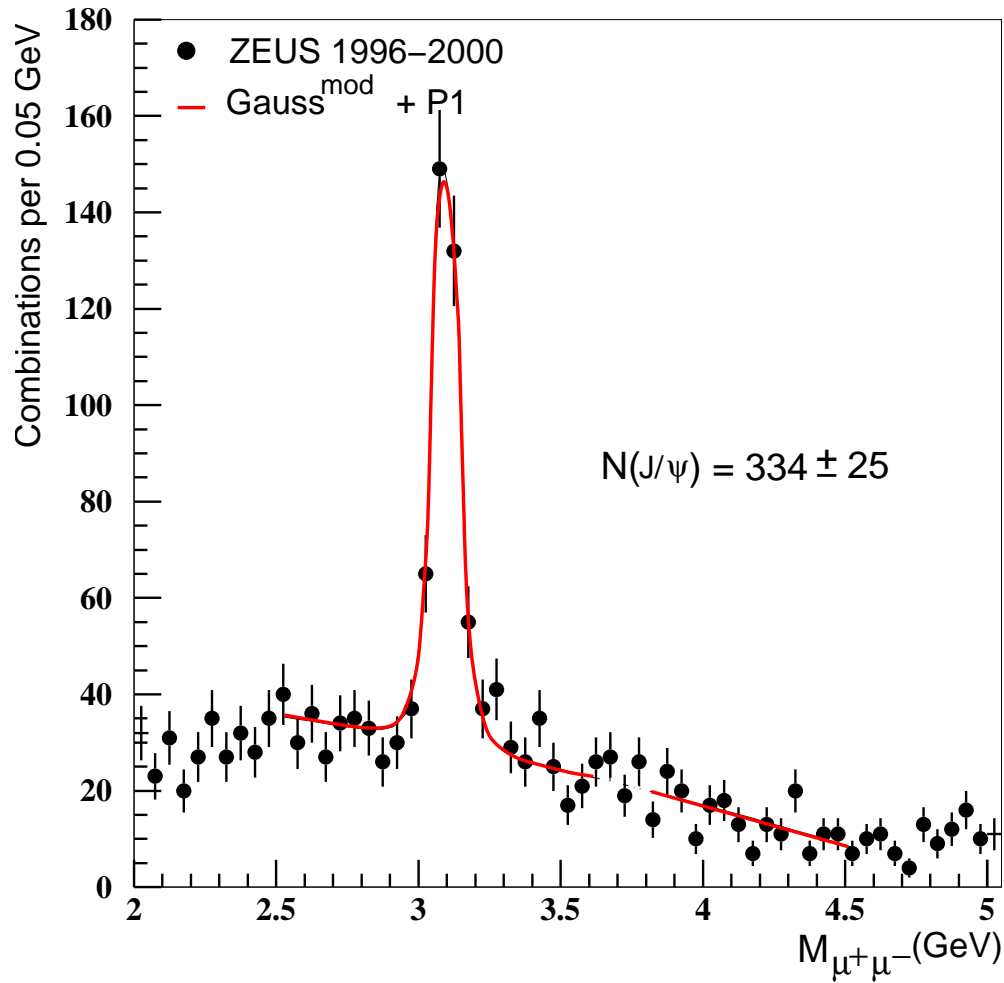


**Figure 4.14:** Invariant mass spectrum after all selection cuts in the kinematic region  $2 < Q^2 < 80 \text{ GeV}^2$ ,  $50 < W < 250 \text{ GeV}$ ,  $0.2 < z < 0.9$  and  $-1.6 < Y_{lab} < 1.3$ . The curve is the result of the fit with a modified Gaussian for the signal (see text) and a linear function (P1) for the non-resonant background.

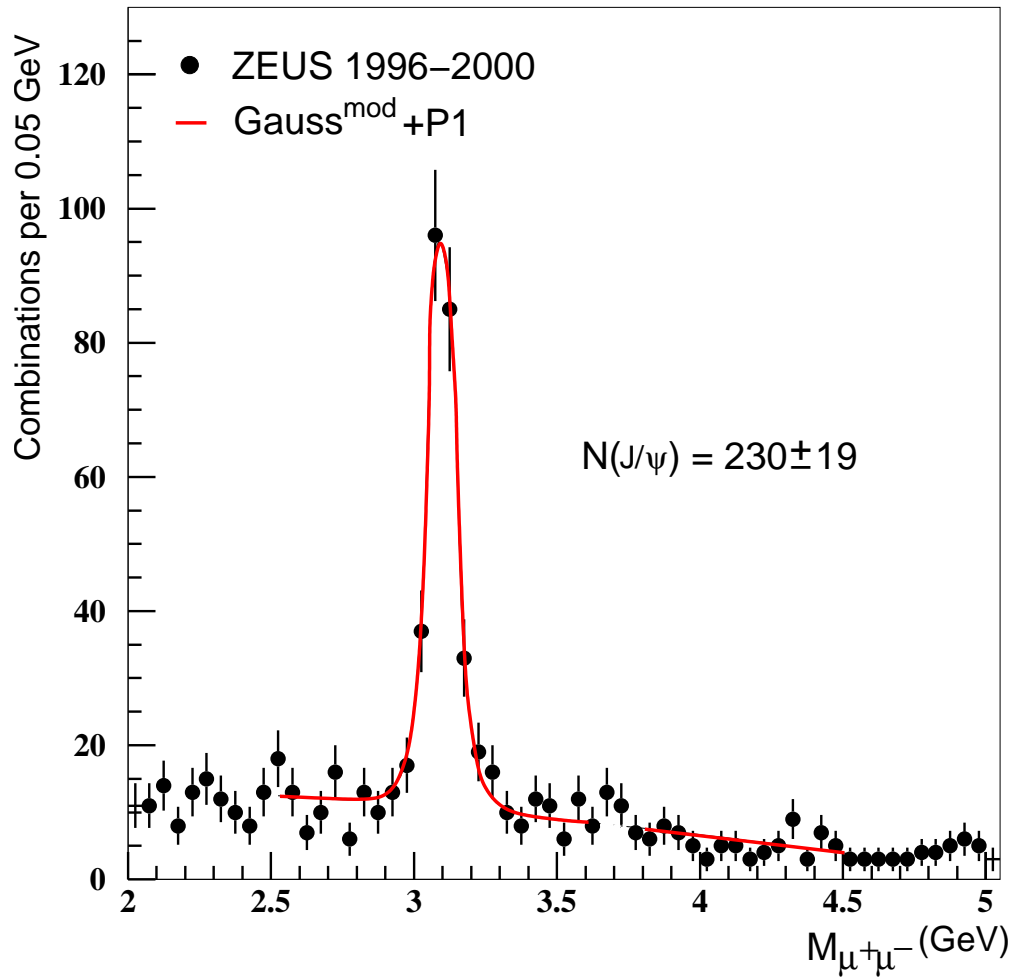


**Figure 4.15:** Invariant mass spectrum after all selection cuts in the kinematic region  $2 < Q^2 < 100 \text{ GeV}^2$ ,  $50 < W < 225 \text{ GeV}$ ,  $0.3 < z < 0.9$  and  $p_T^{*2} > 1 \text{ GeV}^2$  defined in the H1 published paper [33]. The curve is the result of the fit with a modified Gaussian (see Eq. 4.21) for the signal and a linear function (P1) for the non-resonant background.

In order to prepare combined plots of both ZEUS and (already published) H1 results [33] the cross sections are to be recalculated in the kinematic region defined by H1. For this we need to extend the range in  $Q^2$  up to 100 GeV, to reduce the range in  $W$  down to 225 GeV, to increase the lower  $z$  limit to 0.3 and to replace the restriction on rapidity,  $Y_{lab}$ , with the cut on the transverse momentum of  $J/\psi$  in the  $\gamma p$  centre-of-mass frame,  $p_T^{*2} > 1 \text{ GeV}^2$ . In the event selection we keep the track multiplicity cut and the requirement of an energy deposit above 1 GeV in the cone along the outgoing proton direction. The total invariant mass spectrum in such a modified kinematic region is presented in 4.15.

## 4.9 Monte Carlo models

Acceptance, resolution and efficiency corrections are applied to the data using simulated MC events. The MC simulation involves three stages. In the first stage four-vectors of particles are produced according to models implemented in the MC generators. In this analysis CASCADE [110] and EPJPSI [111] generators were used for inelastic  $J/\psi$  production. The proton diffractive dissociation admixture was simulated using the EPSOFT [112, 113] and DIFFVM [114] MC generators. None of the generators listed above includes radiative corrections. In the second stage a GEANT-based package is used to simulate the ZEUS detector response and trigger decision. In the last stage all generated events are passed through the same reconstruction chain as the data.

- The CASCADE version 1.2 simulates  $\gamma g^* \rightarrow J/\psi g$  process in leading order for inelastic  $J/\psi$  production, with the initial state parton shower being generated according to the CCFM evolution equations [51, 52]. In version 1.2 the gluon splitting functions contain both singular and non-singular terms. The CCFM evolution, which to some extent interpolates between BFKL and DGLAP evolutions, implies that the initial gluon can be off-shell. Currently the photon virtuality ( $Q^2$ ) dependence is not yet included into the matrix elements. The gluon density, unintegrated in transverse momentum ( $k_T$ ), is obtained from an analysis of the proton structure functions based on the CCFM equations [115]. In the event generation the gluon density used corresponds to the set named “J2003 set 2” (obtained using the CCFM splitting function containing also the non-singular terms).

The mass of the  $c$  quark was set to 1.5 GeV and the evolution scale of the strong coupling constant  $\alpha_s$  to the  $J/\psi$  transverse mass,  $\sqrt{M_\psi^2 + p_T^2}$ . The Lund string fragmentation package JETSET/PYTHIA [116, 117] is used for hadronisation in CASCADE.

The MC programs and calculations based on the CCFM evolution and/or  $k_T$ -factorisation have a number of specific features in comparison with the collinear calculations:

- the off-shellness of the initial gluon has important impact on the polarisation properties of  $J/\psi$ ; however in DIS this effect is obscured by the photon virtuality;
  - it is known that the  $k_T$  of the initial gluon leads to a broadening of charmonium transverse momentum spectra [118] (partially included NLO corrections).
- The EPJPSI MC version 3.30/16 incorporates the LO matrix elements of the photon-gluon fusion process and the colour singlet model in the collinear approach. The  $Q^2$  dependence is not included into the matrix elements. Higher-order QCD effects are simulated through initial- and final-state parton showers. The parton density “GRV98 Set LO” was used for the generation. The scale for the evaluation of the parton density functions was chosen as the centre-of-mass energy squared,  $\hat{s}$ , of the hard interacting particles.  $\alpha_s$  was chosen to be running according to the one-loop formula implemented in EPJPSI. The mass of the  $c$  quark was set to 1.5 GeV. Relativistic corrections (due to a relative motion of the  $J/\psi$  constituents) were taken into account (there are no such a corrections available in CASCADE). As for CASCADE in EPJPSI hadronisation is done according to the Lund string model.
  - The main resonant background is the proton-dissociative  $J/\psi$  production. The EPSOFT MC generator has been tuned to describe the processes of proton diffractive dissociation  $\gamma p \rightarrow V Y$  (where  $V$  is a vector meson and  $Y$  is the dissociated system) at ZEUS. In the program implementation only some basic properties of soft hadron-hadron collisions are assumed to describe pomeron-proton scattering. The diffractive process is generated

according to the formula:

$$\frac{d^2\sigma}{dt dM_Y^2} \propto \frac{\exp(-bt)}{(M_Y^2)^\beta}, \quad (4.22)$$

where  $M_Y$  is the mass of the dissociated system ( $M_Y > 1.25$  GeV),  $t$  is the four-momentum transfer at the proton vertex. The constant  $b = 0.6$  GeV<sup>-2</sup> was extracted from data measured at high  $z$  and thus dominated by the diffractive process [119].

- The DIFFVM MC simulates diffractive vector meson production in  $ep$  scattering in the framework of Regge phenomenology and the Vector Dominance Model. In this approach the electron emits a photon (generated according to the equivalent photon approximation) which fluctuates into a virtual vector meson interacting diffractively with the proton. The generator features a detailed description of the proton-dissociative final state, including both the nucleon resonances and the continuum. The DIFFVM MC version was used for systematics studies and also in order to cross check results obtained by H1, so parameters were set accordingly [120, 121].

### 4.9.1 Control plots and resolutions

After all cuts the kinematic variables are calculated according to the formulae given in Section 4.1.

The plots showing the resolution Figs. 4.16, 4.17 and the comparison between reconstructed and the true variables, after all the cuts of the analysis have been applied, are shown in 4.18

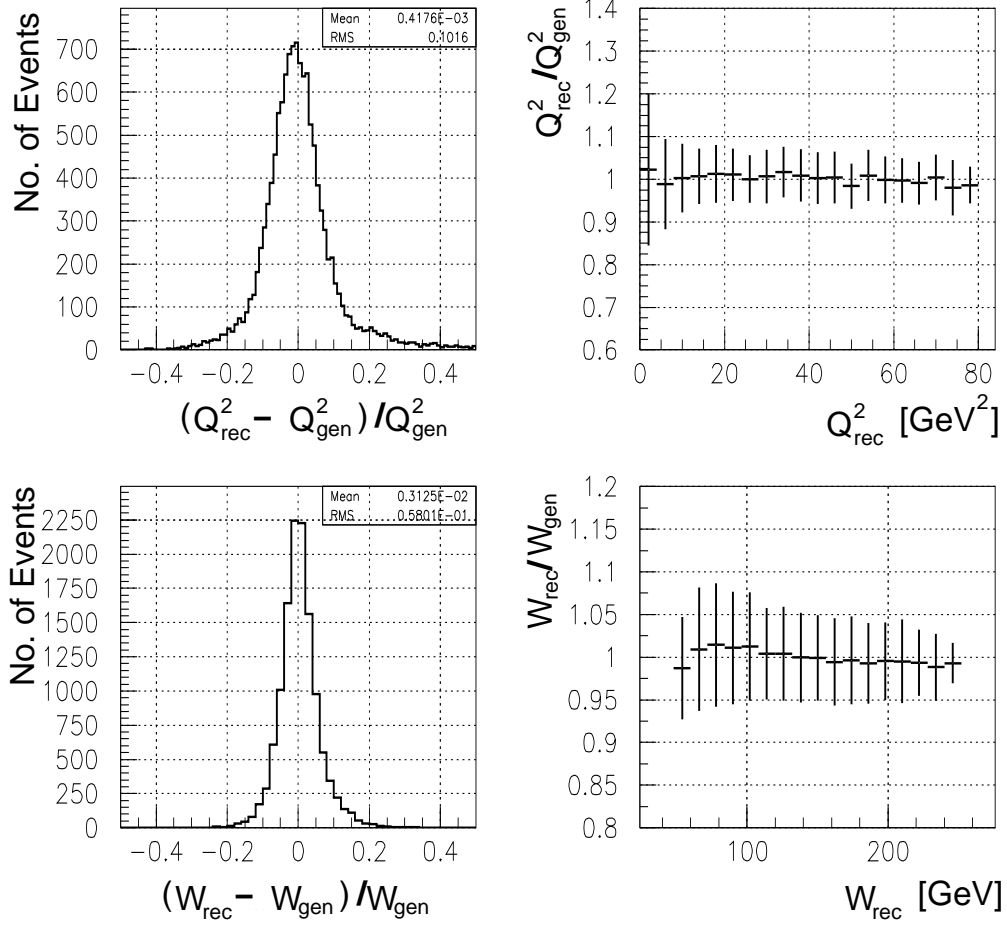


**Figure 4.16:** Resolution of  $Q^2$  and  $W$  in the kinematic region  $2 < Q^2 < 80$  GeV $^2$ ,  $50 < W < 250$  GeV,  $0.2 < z < 0.9$  and  $-1.6 < Y_{\text{lab}} < 1.3$ : the relative difference of reconstructed and generated values, the profile histogram of the ratio of reconstructed and generated values versus reconstructed value shown with the spread option.

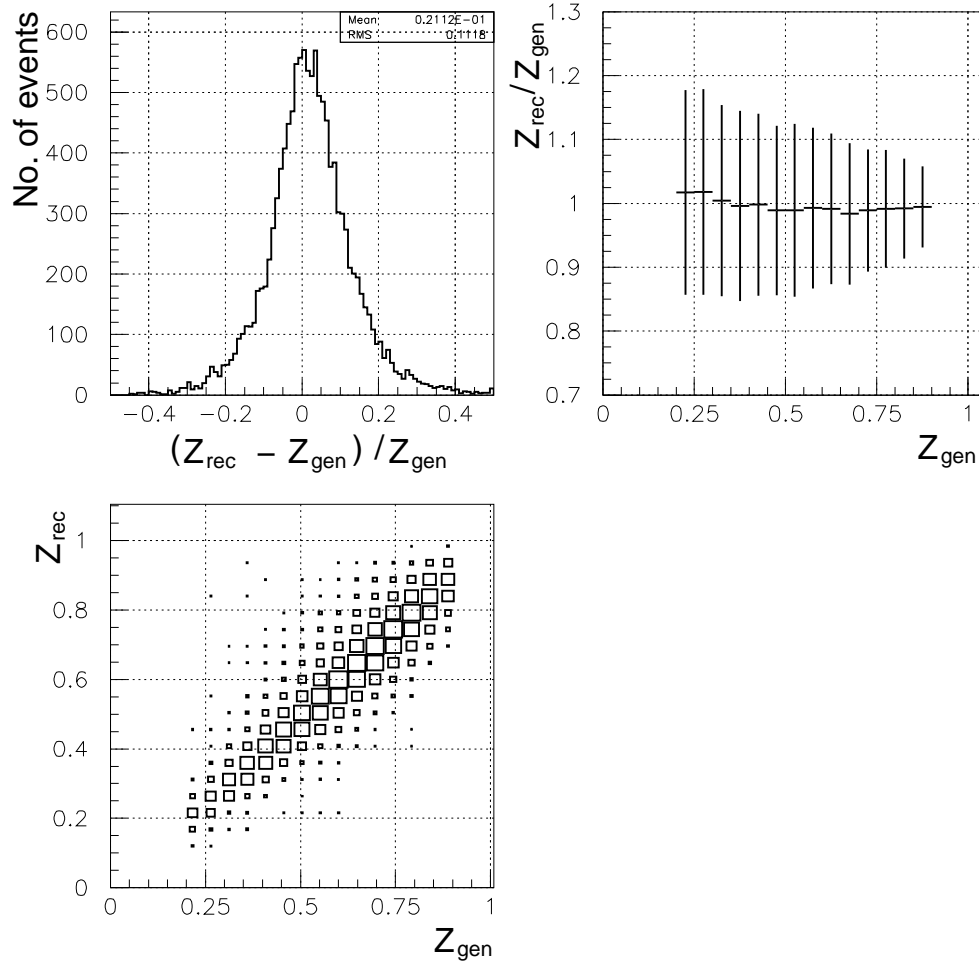


**Figure 4.17:** Resolution of  $z$  in the kinematic region  $2 < Q^2 < 80 \text{ GeV}^2$ ,  $50 < W < 250 \text{ GeV}$ ,  $0.2 < z < 0.9$  and  $-1.6 < Y_{lab} < 1.3$  shown as the relative difference, the profile histogram of the ratio (spread option) and the correlation of reconstructed and generated values.

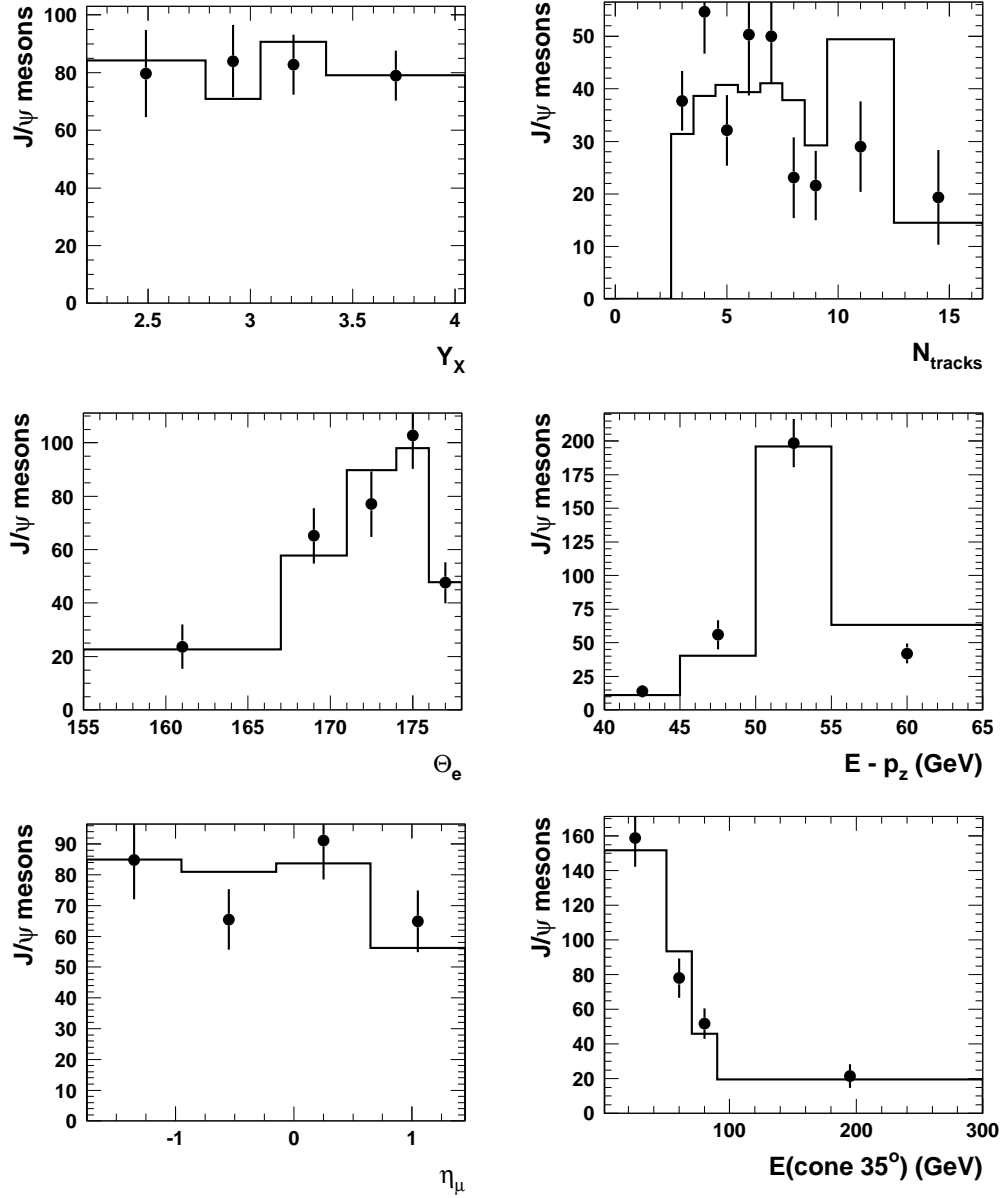


**Figure 4.18:** Shape comparison between the data (dots) and the EPJPSI MC (after bin-by-bin reweighting in  $Q^2$  and  $p_T^{*2}$ ) in the kinematic region  $2 < Q^2 < 80 \text{ GeV}^2$ ,  $50 < W < 250 \text{ GeV}$ ,  $0.2 < z < 0.9$  and  $-1.6 < Y_{lab} < 1.3$ . Number of reconstructed  $J/\psi$  mesons is shown as a function of  $Y_X$ , track multiplicity, polar angle of the scattered lepton,  $\delta$ , pseudorapidity of decay muons and energy deposit in a cone of  $35^\circ$ .



# Chapter 5

## Inelastic $J/\psi$ Production in DIS

In this chapter, results of the inelastic  $J/\psi$  mesons production in deep inelastic scattering will be derived and discussed. In the first section the procedure to correct the data for acceptance and efficiency losses as well as the background subtraction will be described. The measured cross sections are compared to the theoretical predictions based on non-relativistic QCD and the  $k_T$ -factorisation approach. The experimental results will also be compared to the CASCADE Monte Carlo simulation. The chapter closes with a discussion of the results.

### 5.1 Cross section measurement

Prior to the cross-section measurement, the residual diffractive proton-dissociative background was subtracted. Although such events are produced at  $z \sim 1$  and the inelasticity was restricted to  $0.2 < z < 0.9$ , some diffractive events migrate into the data sample due to the finite  $z$  resolution.

To estimate the admixture from proton-dissociative events remaining after the selection described in Sec.4.8, the track multiplicity distribution (without the track multiplicity cut) in data was fitted to a sum of inelastic (CASCADE) and diffractive (EPSOFT) MC predictions using CERNLIB routine HMCMLL which performs a binned maximum likelihood fit of the given Monte Carlo distributions to the data distribution. The mixture of these two MC samples was found to be 70% and 30% (see Fig. 5.1). The fit with the multiplicity cut being applied ( $N_{\text{tracks}} \geq 3$ ) yielded a contribution of  $6 \pm 1\%$  from proton dissociation for the whole sample. The proton-dissociative contributions were subtracted bin-by-bin

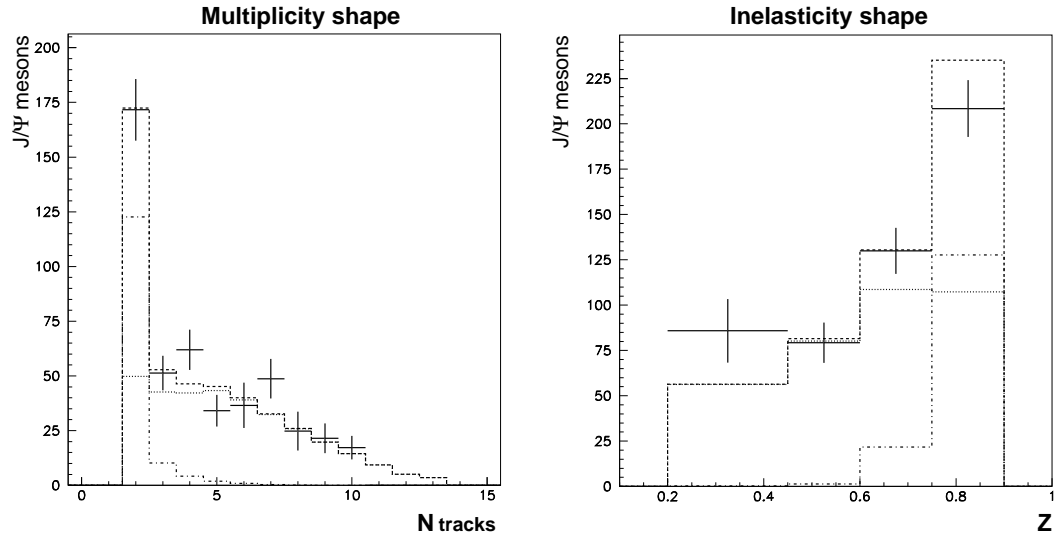


**Figure 5.1:** Mixture of two MC samples fitted to the multiplicity distribution in the kinematic region  $2 < Q^2 < 80 \text{ GeV}^2$ ,  $50 < W < 250 \text{ GeV}$ ,  $0.2 < z < 0.9$  and  $-1.6 < Y_{lab} < 1.3$  without multiplicity cut. The data are shown as crosses, CASCADE as dotted line and EPSOFT as dash-dotted line. The sum CASCADE (70%) + EPSOFT (30%) is shown as dashed line.

from all measured cross sections according to the EPSOFT predictions normalised to the above fraction.

The number of  $J/\psi$  mesons reconstructed in the kinematic region  $2 < Q^2 < 80 \text{ GeV}^2$ ,  $50 < W < 250 \text{ GeV}$ ,  $0.2 < z < 0.9$  and  $-1.6 < Y_{lab} < 1.3$ , after subtraction of the proton-dissociative admixture, was compared to the predictions of the EPJPSI MC generator. The results are shown in Fig. 5.2 for  $z$ ,  $Q^2$ ,  $W$ ,  $p_T^{*2}$ , the  $J/\psi$  rapidity in the  $\gamma p$  frame<sup>1</sup>,  $Y^*$ , and  $M_X^2$ , where  $M_X$  is the invariant mass of the final state excluding the  $J/\psi$  and the scattered electron.

A comparison of the number of  $J/\psi$  mesons reconstructed in the kinematic region in the kinematic region  $2 < Q^2 < 100 \text{ GeV}^2$ ,  $50 < W < 225 \text{ GeV}$ ,  $0.3 < z < 0.9$  and  $p_T^{*2} > 1 \text{ GeV}^2$  and predictions of the EPJPSI MC generator presented in Fig. 5.3. This kinematic region is used to prepare combined plots of both ZEUS and H1 results [33].

Data were corrected bin-by-bin for geometric acceptance, detector, trigger and reconstruction inefficiencies, as well as for detector resolution, using the

<sup>1</sup>In the  $\gamma p$  centre-of-mass frame, the photon direction was chosen to be the “forward direction”.

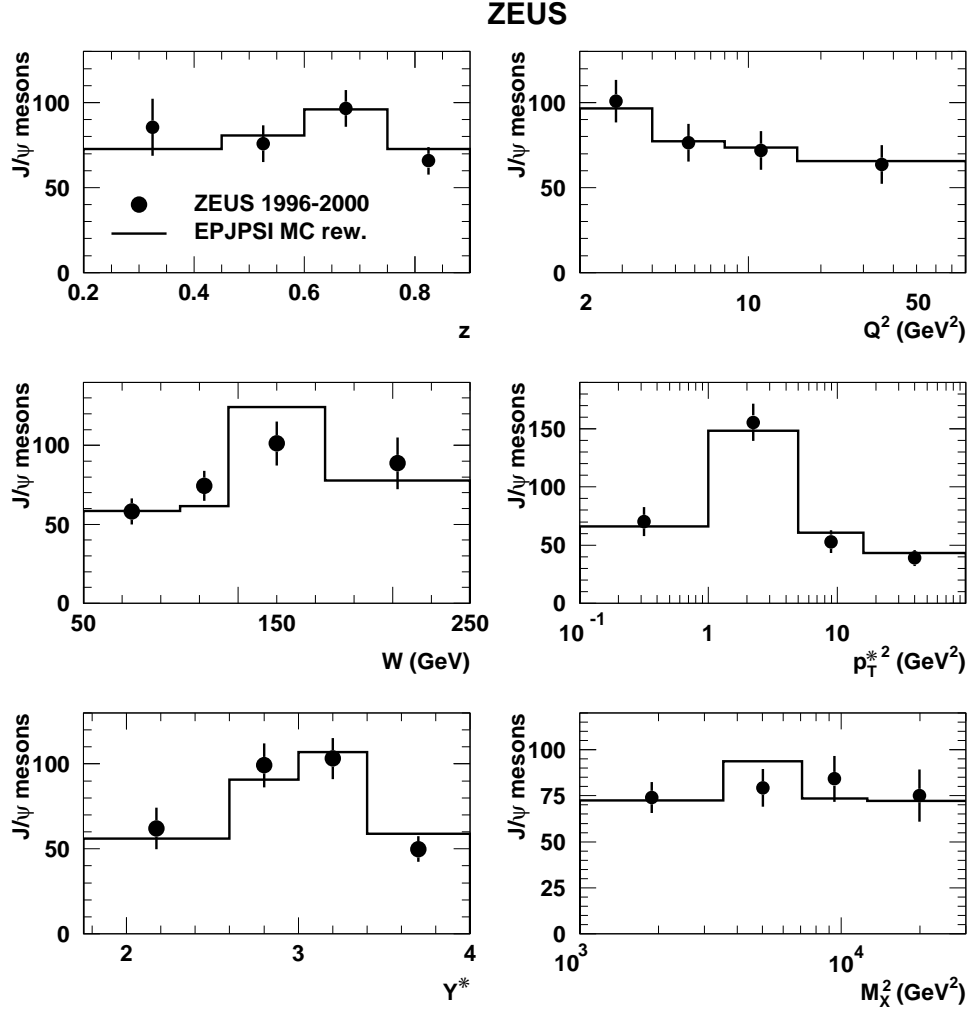


**Figure 5.2:** Shape comparison between the data (dots) and the EPJPSI MC (after bin-by-bin reweighting in  $Q^2$  and  $p_T^{*2}$ ) in the kinematic region  $2 < Q^2 < 80 \text{ GeV}^2$ ,  $50 < W < 250 \text{ GeV}$ ,  $0.2 < z < 0.9$  and  $-1.6 < Y_{lab} < 1.3$ . Number of reconstructed  $J/\psi$  mesons is shown as a function of  $z$ ,  $Q^2$ ,  $W$ ,  $p_T^{*2}$ ,  $Y^*$ ,  $M_X^2$ .

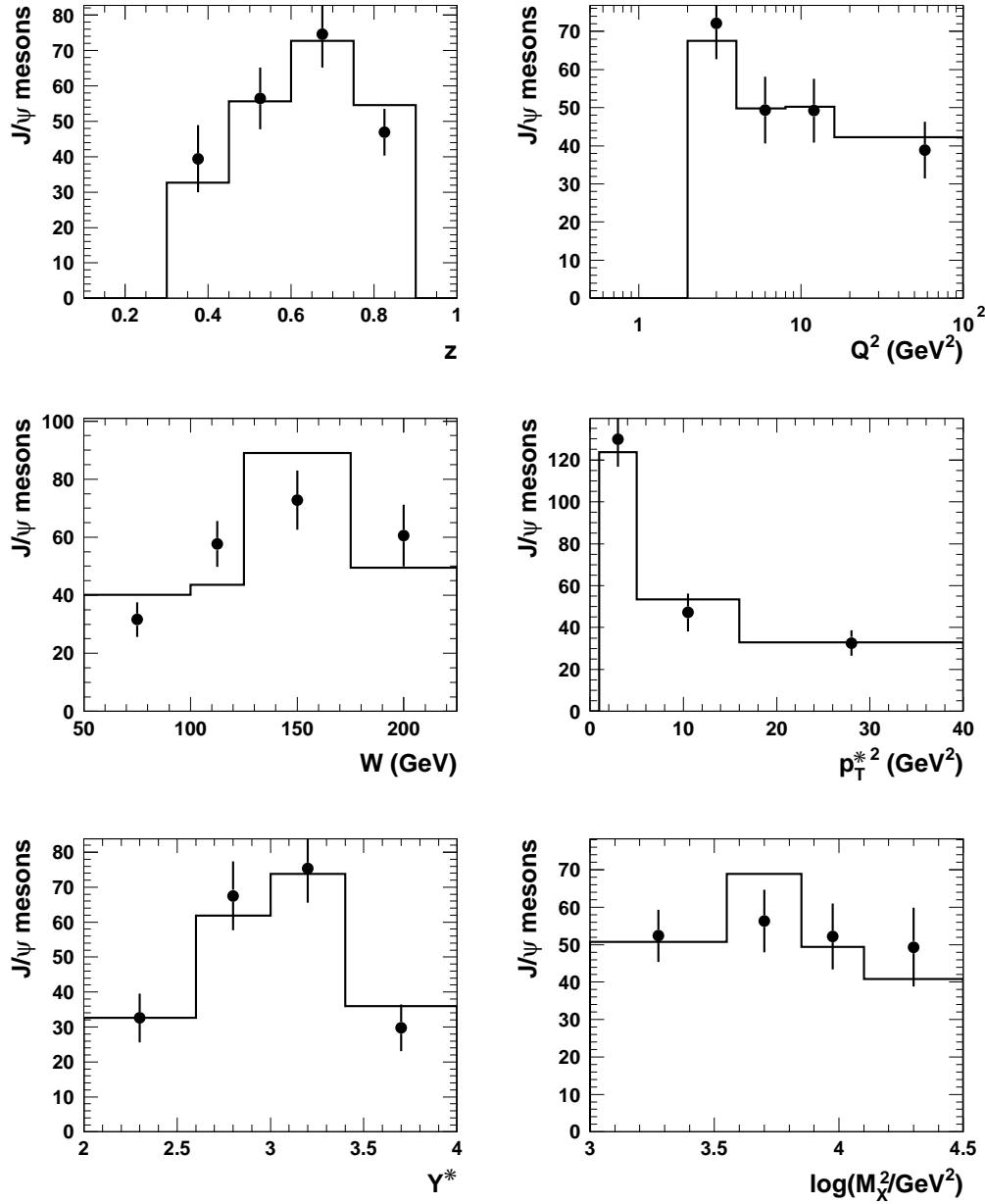


**Figure 5.3:** Shape comparison between the data (dots) and the EPJPSI MC (after bin-by-bin reweighting in  $Q^2$  and  $p_T^{*2}$ ) in the kinematic region  $2 < Q^2 < 100 \text{ GeV}^2$ ,  $50 < W < 225 \text{ GeV}$ ,  $0.3 < z < 0.9$  and  $p_T^{*2} > 1 \text{ GeV}^2$ . Number of reconstructed  $J/\psi$  mesons is shown as a function of  $z$ ,  $Q^2$ ,  $W$ ,  $p_T^{*2}$ ,  $Y^*$  and  $\log M_X^2$ .

EPJPSI MC generator. The acceptance,  $A_i(\mathcal{O})$ , as a function of an observable,  $\mathcal{O}$ , in a given bin,  $i$ , is  $A_i(\mathcal{O}) = N_i^{\text{rec}}(\mathcal{O})/N_i^{\text{gen}}(\mathcal{O})$ , where  $N_i^{\text{gen}}(\mathcal{O})$  is the number of generated MC events and  $N_i^{\text{rec}}(\mathcal{O})$  is the number of reconstructed events passing all the selection requirements.

Differential cross sections as a function of  $\mathcal{O}$  in a given bin  $i$  were obtained using the expression

$$\frac{d\sigma_i}{d\mathcal{O}} = \frac{N_i}{\mathcal{B} \mathcal{L} A_i(\mathcal{O}) \Delta_i(\mathcal{O})},$$

where  $N_i$  is the number of signal events, reconstructed in each bin after subtraction of the estimated contribution from the diffractive proton–dissociative events,  $\mathcal{B}$  the branching ratio ( $5.88 \pm 0.10\%$ ) [109],  $\Delta_i(\mathcal{O})$  the bin width and  $\mathcal{L}$  the integrated luminosity.

The background from inelastic  $\psi'$  photoproduction is expected to be 15% [124, 125]. This expectation was confirmed by a direct measurement of the  $\psi'$  to  $J/\psi$  cross section ratio [128]. Restricting the phase–space region in this analysis similar to that for photoproduction,  $50 < W < 180$  GeV and  $0.55 < z < 0.9$ , the number of observed  $\psi'$  events was consistent with the expectation from the  $\psi'$  to  $J/\psi$  ratio measured in the photoproduction regime. The contribution of  $J/\psi$  mesons from  $\psi'$  decays was assumed to yield the same kinematic distributions as the dominant direct  $J/\psi$  contribution and, therefore, the theoretical predictions for  $J/\psi$  production were scaled up by 15%. This change is small compared to the normalisation error of the LO NRQCD predictions.

Monte Carlo studies showed that the contribution from  $B$ –meson decays into  $J/\psi$  was concentrated at low– $z$  values and small elsewhere. For  $0.1 < z < 0.4$ , this contribution can be as large as 20%. The beauty contribution was estimated using the RAPGAP MC and added to the  $J/\psi$  predictions. This change is small compared to the normalisation uncertainty of the LO NRQCD predictions.

The  $J/\psi$  meson can be produced via  $\chi_c$  radiative decays,  $\chi_c \rightarrow J/\psi\gamma$ . While  $\chi_c$  mesons can be produced copiously in hadron–hadron collisions through  $gg$ ,  $gq$  and  $q\bar{q}$  interactions,  $\chi_c$  production via photon–gluon fusion is forbidden at LO in the CS model. This leaves only resolved photon processes, strongly suppressed at non–zero photon virtuality, or CO processes as sources of  $\chi_c$  production. However, the ratio of the  $\chi_c$  to  $J/\psi$  from the CO processes is expected to be below 1% [123]. This contribution was therefore neglected.

The effect of the LO electroweak corrections was studied using the HERACLES [126] MC program. The open charm DIS cross section was evaluated using

the RAPGAP [127] MC program with and without radiative corrections, as calculated by HERACLES, in a  $W-Q^2$  grid (see Fig. 5.4). The measured cross sections were then corrected to the QED Born level using the HERACLES predictions. In the region covered by the data, this correction was  $-2\%$  on average and always below  $7\%$  in absolute value.

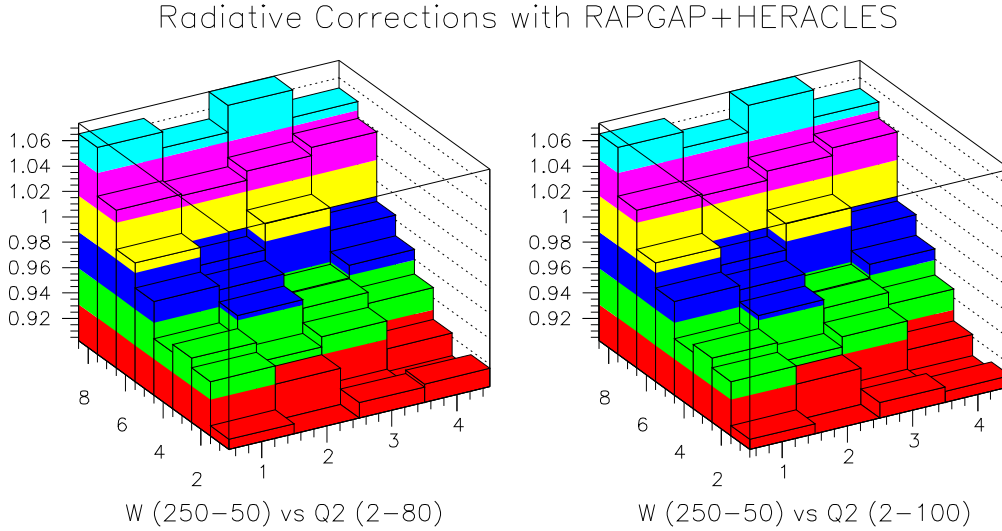


**Figure 5.4:** Radiative (LO electroweak) corrections obtained using RAPGAP+HERACLES. in a  $W - Q^2$  grid. The grid is made of 8 equidistant bins in  $W$  and 4 nominal analysis bins in  $Q^2$ :  $2 < Q^2 < 4 \text{ GeV}^2$ ,  $4 < Q^2 < 8 \text{ GeV}^2$ ,  $8 < Q^2 < 16 \text{ GeV}^2$ ,  $2 < Q^2 < 80 \text{ GeV}^2$  (right plot) or  $2 < Q^2 < 100 \text{ GeV}^2$  (left plot). The correction is the ratio  $\sigma_{Born}/\sigma_{obs}$ , where  $\sigma_{Born}$  is the Born-level cross section and  $\sigma_{obs}$  is the cross section measured in the data.

As the measured cross sections were extracted from events collected at two different centre-of-mass energies,  $\sqrt{s} = 300 \text{ GeV}$  and  $318 \text{ GeV}$ , they were corrected to  $\sqrt{s} = 318 \text{ GeV}$  using MC predictions obtained at both centre-of-mass energies. This was done according to the formula (courtesy M. Corradi):

$$\sigma_{318} = \sigma_{obs} \frac{\sigma_{318}^{MC} (\mathcal{L}_{300} + \mathcal{L}_{318})}{\sigma_{300}^{MC} \mathcal{L}_{300} + \sigma_{318}^{MC} \mathcal{L}_{318}},$$

where  $\sigma_{300}^{MC}$ ,  $\sigma_{318}^{MC}$  are the MC predictions and  $\sigma_{obs}$  is the cross section measured in the data including events with both centre-of-mass energies. These corrections did not exceed  $7\%$ .

## 5.2 Systematic uncertainties

The systematic uncertainties of the measured differential cross sections were determined by changing the selection cuts or the analysis procedure in turn and repeating the extraction of the differential cross sections. The resulting uncertainty on the total cross section is given in parentheses. The following categories of systematic uncertainties were considered:

- scattered electron reconstruction: these uncertainties were evaluated as described elsewhere [129] (2%);
- CAL energy scale and resolution simulation: these uncertainties were evaluated as described elsewhere [129] (2%);
- tracking: the resolutions on track momenta and angles were varied by  $\pm 20\%$  of their values and the magnetic field by  $\pm 0.3\%$  (1%);
- muon reconstruction: the uncertainty of the muon acceptance, including those of the efficiency of the muon chambers, the trigger selection algorithms and the offline reconstruction, was obtained from a study based on an independent dimuon sample at high  $Q^2$ , performed following the method discussed elsewhere [130] (6%);
- fitting procedure: the invariant-mass range and the functional form of the background were varied (2%);
- simulation of the process  $\gamma^*g \rightarrow J/\psi g$ : the CASCADE MC rather than the EPJPSI MC was used to calculate acceptances (5%);
- subtraction of the remaining diffractive proton-dissociative admixture: DIFFVM rather than EPSOFT was used to perform the subtraction of the proton diffractive events (3%).

These estimations were also made in each bin of the differential cross sections. All of the above individual sources of systematic uncertainty were added in quadrature.

The following sources resulted in an overall shift of the cross section and were therefore treated as normalisation uncertainties:

- the integrated luminosity determination has an uncertainty of 2%;  
The systematic error for the integrated luminosity is derived from the systematic error of the luminosity measurement for each run period:  $\Delta\mathcal{L} = \sum_i \mathcal{L}_i \sigma_i$ , where  $i$  runs over run periods, namely 96, 97, 98,  $99e^-$ ,  $99e^+$  and 00;  $\mathcal{L}_{96} = 5.08 \text{ pb}^{-1}$ ,  $\mathcal{L}_{97} = 27.63 \text{ pb}^{-1}$ ,  $\mathcal{L}_{98} = 3.98 \text{ pb}^{-1}$ ,  $\mathcal{L}_{99e^-} = 11.91 \text{ pb}^{-1}$ ,  $\mathcal{L}_{99e^+} = 17.82 \text{ pb}^{-1}$ ,  $\mathcal{L}_{00} = 42.36 \text{ pb}^{-1}$ ;  $\sigma_{96} = 1.1\%$ ,  $\sigma_{97} = 1.8\%$ ,  $\sigma_{98} = 1.8\%$ ,  $\sigma_{99e^-} = 1.8\%$ ,  $\sigma_{99e^+} = 2.25\%$ ,  $\sigma_{00} = 2.25\%$ .
- the branching ratio of  $J/\psi \rightarrow \mu^+ \mu^-$  has an uncertainty of 1.7% [109].

The normalisation uncertainties were not included in the total systematic uncertainty.

### 5.3 Results

The cross section for the process  $ep \rightarrow eJ/\psi X$  in the kinematic region  $2 < Q^2 < 80 \text{ GeV}^2$ ,  $50 < W < 250 \text{ GeV}$ ,  $0.2 < z < 0.9$  and  $-1.6 < Y_{lab} < 1.3$  is

$$302 \pm 23 \text{ (stat.) } {}^{+28}_{-20} \text{ (syst.) pb,}$$

where the first uncertainty is statistical and the second systematic. In Figs. 5.5, 5.6 and 5.7, the differential cross sections as a function of  $z$ ,  $Q^2$ ,  $W$ ,  $p_T^{*2}$ ,  $Y^*$ ,  $\log M_X^2$  and the rapidity of the hadronic system  $X$ ,  $Y_X$ , are shown. They are compared to the predictions of the NRQCD model [131], the CS model with  $k_T$  factorisation (LZ) [132] and to the CASCADE MC. The beauty contribution, estimated using the RAPGAP MC, is also shown separately in Figs. 5.5c and 5.6a. All differential cross sections and normalised cross sections are given in Appendix-A Tables A.1, A.2 and A.3. The uncertainties for the CS and CO NRQCD predictions correspond to variations of the charm-quark mass ( $m_c = 1.5 \pm 0.1 \text{ GeV}$ ) and of the renormalisation and factorisation scales from  $1/2\sqrt{Q^2 + M_\psi^2}$  to  $2\sqrt{Q^2 + M_\psi^2}$ . The uncertainty on the long-distance matrix elements and the effect of different choices of parton distribution functions (default set is MRST98LO) are also taken into account. The bands in the figures shows all these uncertainties added in quadrature.

In general, the CSM is consistent with the data. The predictions including both CS and CO contributions are higher than the data, especially at high  $z$  and

low  $p_T^{*2}$ . At high values of  $p_T^{*2}$  the agreement with the data is reasonable. The prediction does not describe the shapes of the  $z$ ,  $Y^*$ ,  $\log M_X^2$  and  $Y_X$  distributions. Previous photoproduction results [31, 32] showed that the agreement between data and theory at high  $z$  can be improved using resummed LO NRQCD predictions [133]. It should be noted that, in photoproduction, inclusion of the NLO corrections to the CSM, not available for DIS, significantly improved the description of the data.

For the LZ  $k_T$ -factorisation predictions, the parametrisation, KMS [134], of the unintegrated gluon density was used. The charm-quark mass was set to  $m_c = 1.4$  GeV, which is the mass used in the KMS parametrisation. The renormalisation and factorisation scales were both set to  $\mu = k_T$  for  $k_T > 1$  GeV. For  $k_T \leq 1$  GeV the scales were fixed at 1 GeV. Calculations based on the  $k_T$ -factorisation approach give a reasonable description of the data both in shape and normalisation.

The data are also compared with the predictions of the CASCADE MC using the  $k_T$ -factorisation approach, where gluons are treated according to the CCFM evolution equations. These predictions were obtained by setting the charm-quark mass to 1.5 GeV (default JETSET/PYTHIA value for  $m_c$ ), the evolution scale of the strong coupling constant to the  $J/\psi$  transverse mass,  $\sqrt{M_\psi^2 + p_T^2}$ , and using the unintegrated gluon-density parametrisation “J2003 set 2”. The CASCADE MC is above the data for  $z > 0.45$  and for  $W < 175$  GeV.

In order to compare the present measurements directly to the H1 results [33], differential cross sections were determined in the kinematic range  $2 < Q^2 < 100$  GeV<sup>2</sup>,  $50 < W < 225$  GeV,  $0.3 < z < 0.9$  and  $p_T^{*2} > 1$  GeV<sup>2</sup>. All ZEUS differential cross sections and normalised cross sections are given in Table A.4. The results of this comparison are shown in Fig. 5.8. The present results are in agreement with those from H1. In Fig. 5.5a, the ZEUS data are in better agreement with the CSM prediction than in Fig. 5.8a. This is a consequence of the  $p_T^{*2} > 1$  GeV<sup>2</sup> cut used in Fig. 5.8a combined with the fact that the CS prediction underestimate the data at high  $p_T^{*2}$ , as seen in Fig. 5.6a.

## 5.4 Conclusions

In this chapter we have presented the measurements of total and single differential cross sections of inelastic  $J/\psi$  production in neutral current deep inelastic  $e^+p$  scattering.

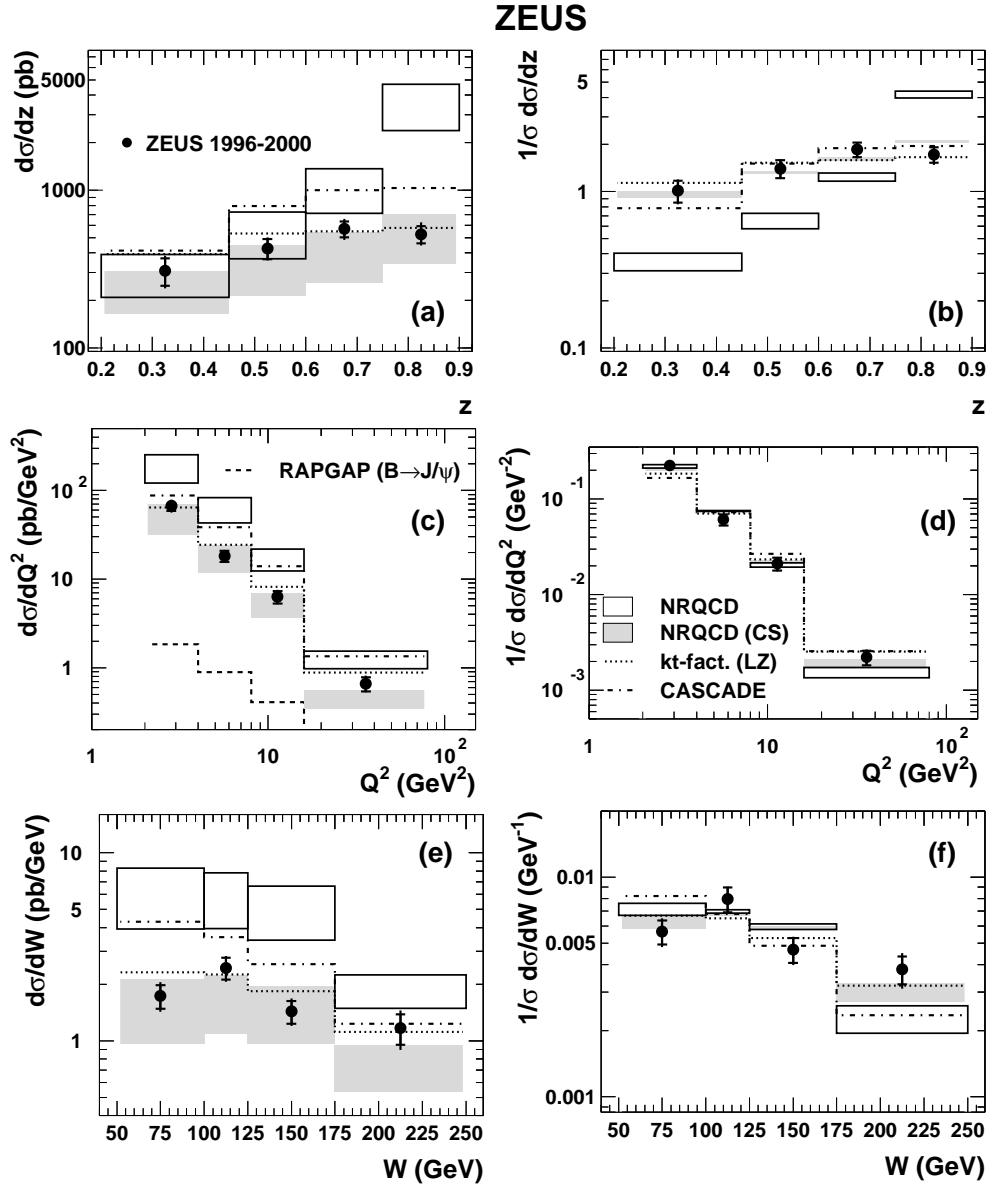


**Figure 5.5:** Differential cross sections for the reaction  $ep \rightarrow eJ/\psi X$  in the kinematic region  $2 < Q^2 < 80 \text{ GeV}^2$ ,  $50 < W < 250 \text{ GeV}$ ,  $0.2 < z < 0.9$  and  $-1.6 < Y_{lab} < 1.3$  as a function of (a)  $z$ , (c)  $Q^2$  and (e)  $W$ . The inner error bars of the data points show the statistical uncertainty; the outer bars show statistical and systematic uncertainties added in quadrature. The data are compared to LO NRQCD predictions, a LO CS calculation, a prediction in the  $k_T$ -factorisation approach within the CSM and the CASCADE MC predictions. (b), (d) and (f) show the data and the theoretical predictions normalised to unit area.

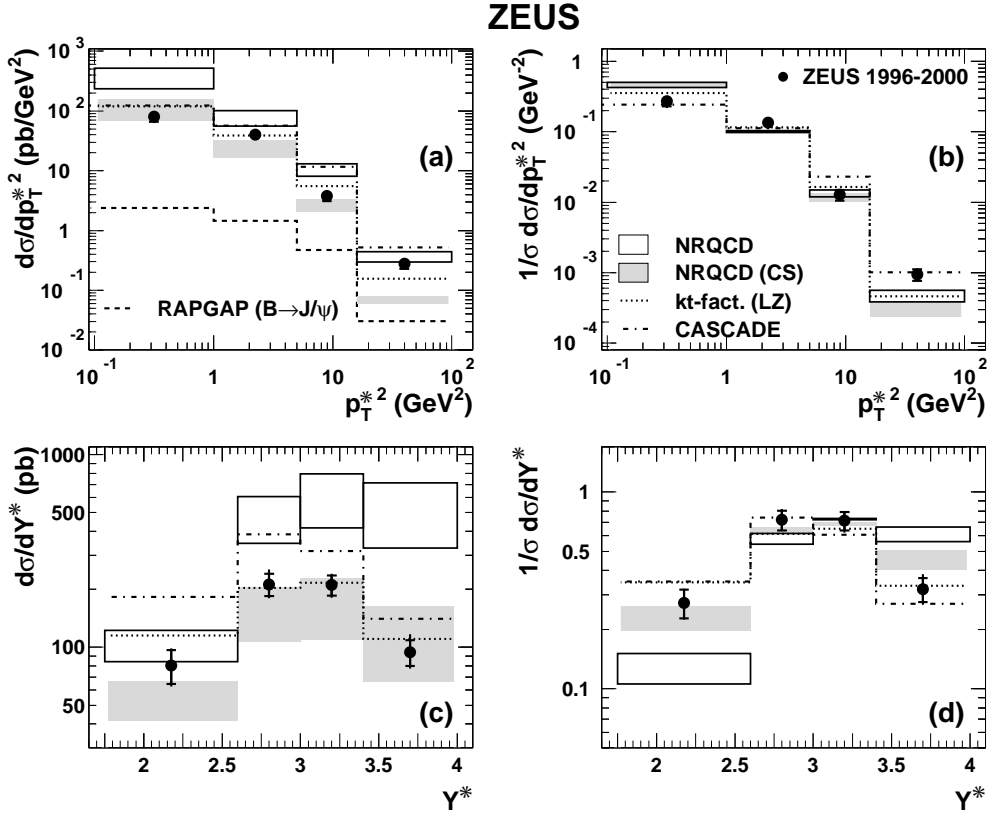


**Figure 5.6:** Differential cross sections for the reaction  $ep \rightarrow e J/\psi X$  in the kinematic region  $2 < Q^2 < 80 \text{ GeV}^2$ ,  $50 < W < 250 \text{ GeV}$ ,  $0.2 < z < 0.9$  and  $-1.6 < Y_{lab} < 1.3$  as a function of (a)  $p_T^{*2}$  and (c)  $Y^*$ . The inner error bars of the data points show the statistical uncertainty; the outer bars show statistical and systematic uncertainties added in quadrature. The data are compared to LO NRQCD predictions, a LO CS calculation, a prediction in the  $k_T$ -factorisation approach within the CSM and the CASCADE MC predictions. (b), (d) show the data and the theoretical predictions normalised to unit area.

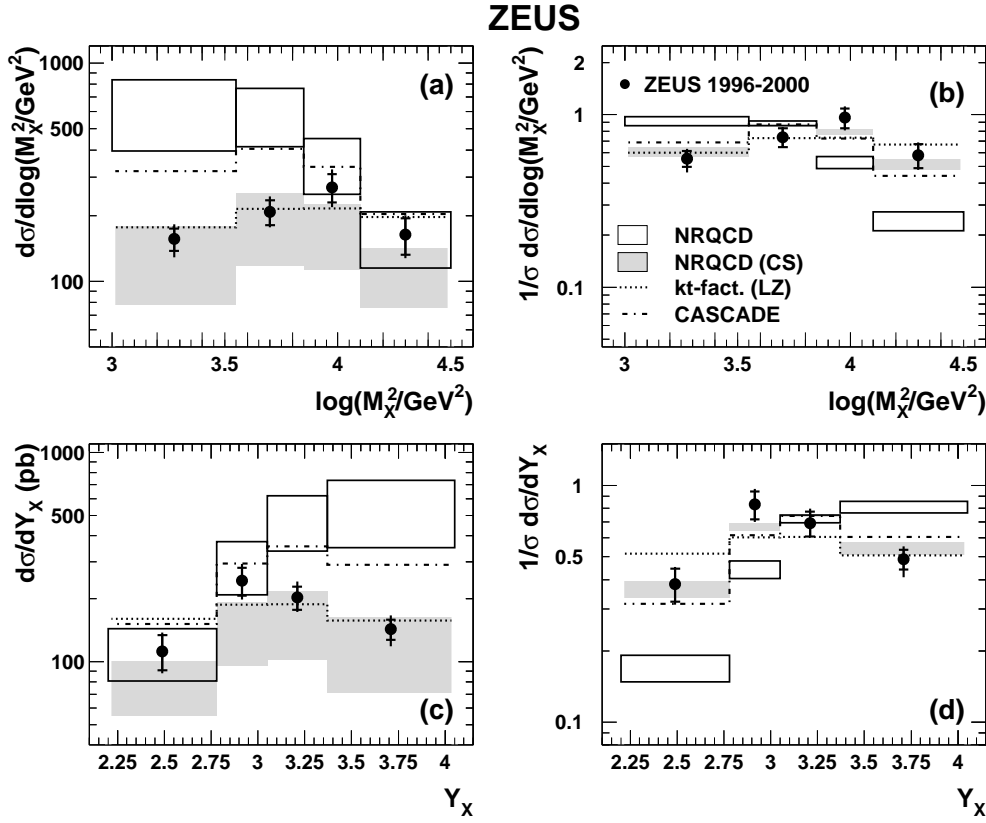


**Figure 5.7:** Differential cross sections for the reaction  $ep \rightarrow e J/\psi X$  in the kinematic region  $2 < Q^2 < 80 \text{ GeV}^2$ ,  $50 < W < 250 \text{ GeV}$ ,  $0.2 < z < 0.9$  and  $-1.6 < Y_{lab} < 1.3$  as a function of (a)  $\log M_X^2$  and (c)  $Y_X$ . The inner error bars of the data points show the statistical uncertainty; the outer bars show statistical and systematic uncertainties added in quadrature. The data are compared to LO NRQCD predictions, a LO CS calculation, a prediction in the  $k_T$ -factorisation approach within the CSM and the CASCADE MC predictions. (b), (d) show the data and the theoretical predictions normalised to unit area.

The measurements were performed with the ZEUS detector at HERA using an integrated luminosity of  $109\text{pb}^{-1}$ . The  $J/\psi$  mesons were identified using the decay channel  $J/\psi \rightarrow \mu^+\mu^-$ . The measurements were performed in the kinematic range  $2 < Q^2 < 80 \text{ GeV}^2$ ,  $50 < W < 250 \text{ GeV}$ ,  $0.2 < z < 0.9$  and  $-1.6 < Y_{lab} < 1.3$ , where  $Q^2$  is the virtuality of the exchanged photon,  $W$  is the photon-proton centre-of-mass energy,  $z$  is the fraction of the photon energy carried by the  $J/\psi$  meson in the proton rest frame and  $Y_{lab}$  is the rapidity of

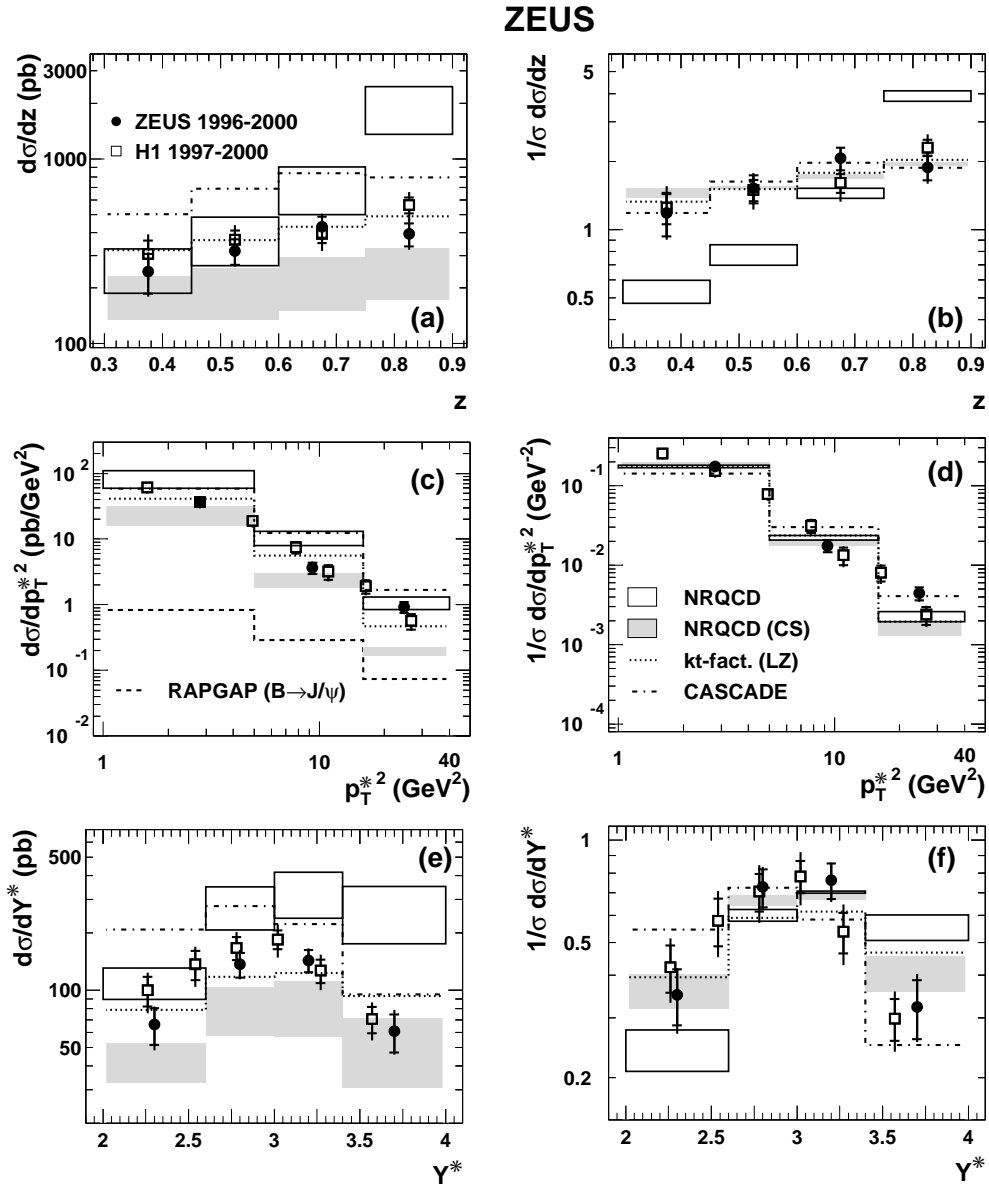


**Figure 5.8:** Differential cross sections for the reaction  $ep \rightarrow e J/\psi X$  in the kinematic region  $2 < Q^2 < 100 \text{ GeV}^2$ ,  $50 < W < 225 \text{ GeV}$ ,  $0.3 < z < 0.9$  and  $p_T^{*2} > 1 \text{ GeV}^2$  as a function of (a)  $z$ , (c)  $p_T^{*2}$  and (e)  $Y^*$ . The inner error bars of the data points show the statistical uncertainty; the outer bars show statistical and systematic uncertainties added in quadrature. The ZEUS and H1 data are compared to LO NRQCD predictions, a LO CS calculation, a prediction in the  $k_T$ -factorisation approach within the CSM and the CASCADE MC predictions. The H1 data points are plotted at the mean value of the data in each interval [33]. The ZEUS data for the  $p_T^{*2}$  differential cross section are plotted at the weighted mean, for each bin, of the EPJPSI MC prediction. (b), (d) and (f) show the data and the theoretical predictions normalised to unit area.

the  $J/\psi$  in the laboratory frame. The measured cross sections are compared to theoretical predictions within the non-relativistic QCD framework including colour-singlet and colour-octet contributions, as well as to predictions based on the  $k_T$ -factorisation approach. Calculations of the colour-singlet process generally agree with the data, whereas inclusion of colour-octet terms spoils this agreement.

From similar studies in photoproduction it is known that resummation techniques for soft gluon emission can improve the theoretical description, however such calculations are not available for DIS. NLO calculations are also not yet available in DIS. CASCADE Monte Carlo predictions are above the data but the shapes are well described. A calculation in the  $k_T$ -factorisation approach based on the BFKL evolution equations gives the best description of the data.

The measurements were performed with the ZEUS detector first time. The data are in agreement with the H1 results in the kinematic region  $2 < Q^2 < 100 \text{ GeV}^2$ ,  $50 < W < 225 \text{ GeV}$ ,  $0.3 < z < 0.9$  and  $p_T^{*2} > 1 \text{ GeV}^2$ .

The measurements can not give a basis for strong conclusions as statistical errors rather large. But we can state that theoretical description of the inelastic  $J/\psi$  production in DIS within the non-relativistic QCD framework requires further developments.

The results of  $J/\psi$  polarization measurements at the Tevatron [146] show strong disagreement with the NRQCD prediction. All this indicates that there is some aspect of the  $J/\psi$  production mechanism that is not yet understood. Further studies may lead to important new insight into the production of charmonium.

A more precise measurement of the studied process will be possible using the HERA II data.

# Chapter 6

## HERA II and the ZEUS Straw-Tube Tracker

In this chapter the luminosity upgrade of the HERA collider and of the ZEUS detector is presented. The heavy flavour physics potential of the upgraded accelerator is discussed together with a brief description of HERA machine. The upgraded ZEUS detector includes new Straw-Tube Tracker (STT) which improve tracking in the forward region. In the second part of this Chapter the STT is described. The ZEUS upgrade has also triggered new software projects. The GEANT simulation and a track pattern reconstruction of the STT will be described in detail.

### 6.1 The HERA luminosity upgrade

In August 2000 the first phase of operation (Run I) of HERA, DESY's electron/positron-proton collider, came to a successful conclusion after the machine reached a luminosity of  $2 \cdot 10^{31} \text{cm}^{-2} \text{s}^{-1}$ , surpassing its original design luminosity by 30%.

The objective of the second phase of the HERA program, Run II, was to operate with a greater luminosity, about four times higher than the design luminosity of Run I. The luminosity can be increased either injecting bunches with higher number of particles, which means higher currents, or reducing the size of the beam cross section. During a long shutdown started in May 2000 the HERA collider has been modified in order to deliver more luminosity for the ZEUS and H1 experiments. This is achieved by substantial modifications of the interaction regions, in order to focus the beams more strongly. Nearly

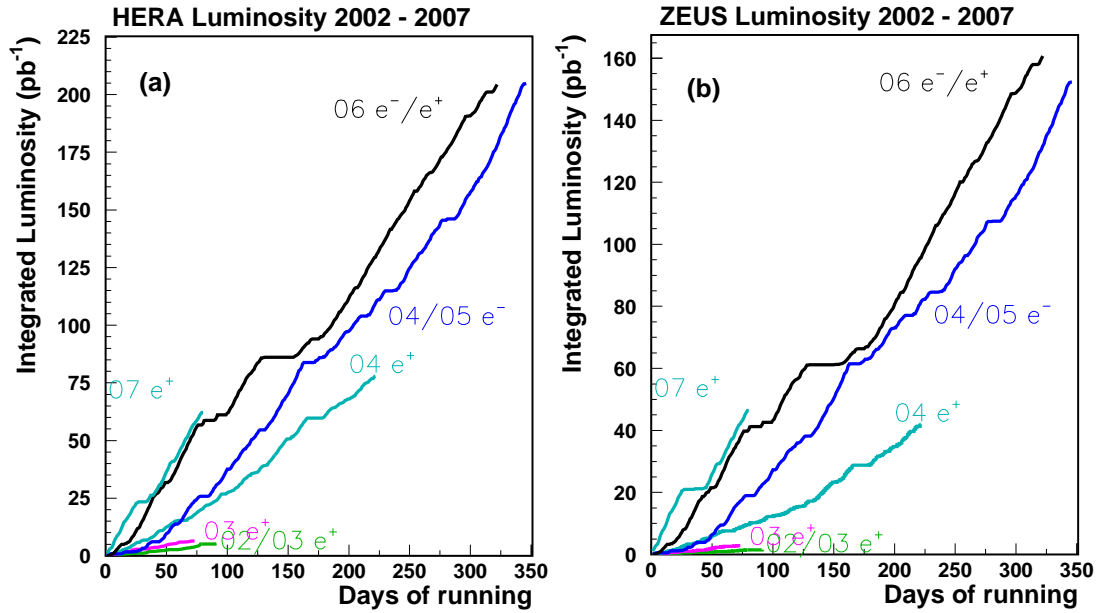


**Figure 6.1:** Integrated luminosity delivered by HERA (a) and collected by ZEUS (b) in the 2002-2007 years.

80 new magnets – weighing up to 7t – were installed in HERA’s proton and electron accelerators during the luminosity upgrade from September 2000 to July 2001. From January to June 2004, the HERA luminosity was increased from  $1.6 \cdot 10^{31} \text{ cm}^{-2} \text{ s}^{-1}$  to  $3.8 \cdot 10^{31} \text{ cm}^{-2} \text{ s}^{-1}$ , which is twice the value achieved in 2000. Figure 6.1 shows the luminosity delivered by HERA in the 2002-2007 years and collected by ZEUS. During the shutdown two spin rotators were installed before and behind the H1 and ZEUS interaction points (Fig 6.2) in order to provide longitudinally the electron beam. Beam polarization and higher luminosity will give more insight on electroweak physics. Furthermore, new important tests of strong interactions will be possible. A review of the physics goals of the next HERA II run is collected in Ref. [135].

## 6.2 The ZEUS upgrade

Together with the upgrade of the HERA collider, new detectors have been realized for the ZEUS and H1 experiment. In particular, the ZEUS experiment has been equipped with a new silicon Micro Vertex Detector (MVD) [136] and a new

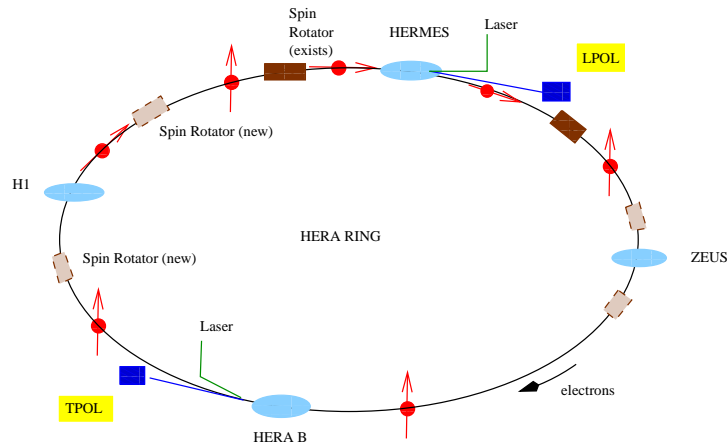


Figure 6.2: Location of the spin rotators on the HERA ring.

forward tracking detector Straw Tube Tracker (STT) [137]. The STT is placed between the existing planar drift chambers (FTD) (see figure 6.3) in the forward region of the ZEUS detector.

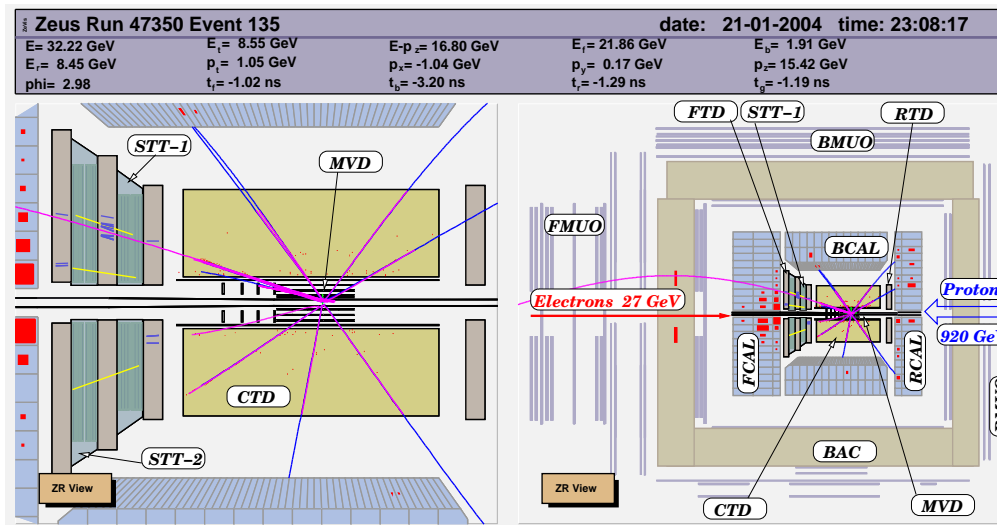
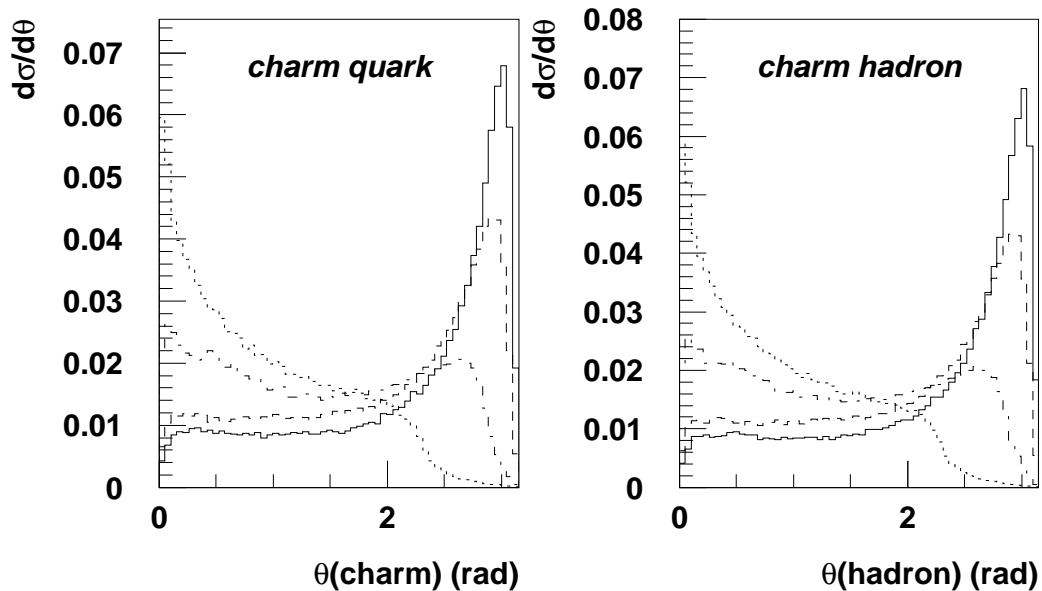


Figure 6.3: Schematic view of the upgraded ZEUS detector.

There are many physics issues that will benefit from the new detectors, in particular the reconstruction of high  $Q^2$  neutral current (NC) and charged current (CC) events and the tagging of events containing heavy quarks.

Any heavy object would mostly have decay products in the forward region due to the asymmetric beam energies. This effect will be even more pronounced since the proton beam energy is increased from 820 GeV to 920 GeV.

The charm production cross section peaks in the forward direction for deep inelastic scattering (DIS) events at high  $Q^2$ . Figure 6.4 shows the angular distribution of charm production in DIS. Bottom production is even more peaked.



**Figure 6.4:** The polar angle distribution of charm quarks and hadrons for different values of  $Q^2$ . Solid line  $Q^2 = 1 \text{ GeV}^2$ , dashed line  $Q^2 = 10 \text{ GeV}^2$ , dot-dashed line  $Q^2 = 100 \text{ GeV}^2$ , short dashed line  $Q^2 = 1000 \text{ GeV}^2$ . The cross sections have all been normalised to the same area.

The reconstruction of  $D^*$  mesons in the forward direction needs efficient track finding, as well as a good momentum measurement.

This will be provided by combining the very good resolution of the microvertex detector with a reliable and efficient track finding using the new tracker. Global tracking including the STT is also beneficial for the tracking of muons into the forward muon chambers. This would be helpful to reduce background in a charm sample selected using semileptonic decays.

The forward tracking is also important for extending the  $W$  range for many other physics topics, such as vector meson production and QCD studies.

## 6.3 The ZEUS Straw-Tube Tracker

In this section the STT detector, GEANT simulation of the STT and a track pattern reconstruction will be described in detail.

### 6.3.1 The STT detector

The STT consists of straw drift tube layers grouped into sectors of trapezoidal shape (wedges). In the  $z$ -direction, i.e. along the beam, the sectors are grouped into 4 super-layers (2 super-layers in each of two 208 mm gaps). A super-layer contains two planes, and each plane is composed of 6 sectors covering the full azimuthal angle. There are in total 48 sectors, among which 24 are small which form one module named STT1. The other 24 sectors are large and they form the 2nd module STT2 (see Fig. 6.5).

A sector consists of 3 layers of straw tubes along the  $z$  direction (see Figure 6.6), it contains 194 (STT1) or 266 (STT2) straws depending on super-layer  $z$  position to match the angular acceptance.

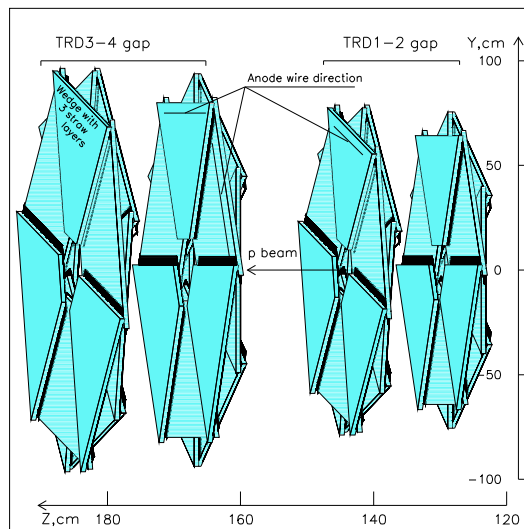


**Figure 6.5:** The complete straw tube tracker. STT1 is in the TRD1-2 gap, while STT2 is in the TRD3-4 gap. Each TRD gap contains 2 super-layers and each super-layer contains two planes rotated by  $30^\circ$  with respect to each other. The super-layers are rotated by  $15^\circ$  with respect to each other. In the figure pairs of superlayers in each gap are artificially separated for clarity.

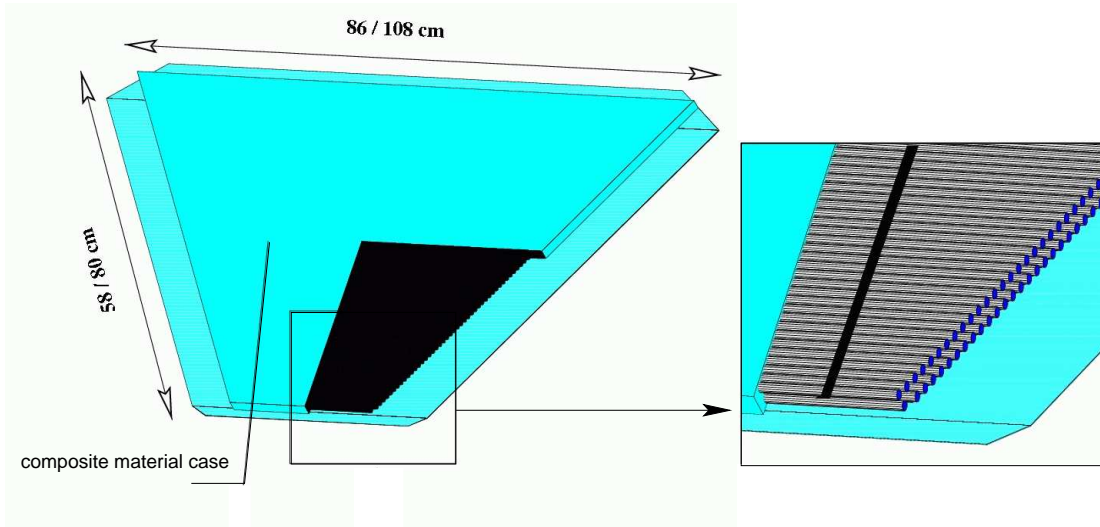


**Figure 6.6:** Single STT sector and arrangement of straws in it.

Straw or tube chambers are proportional chambers constructed with a single anode wire centered in a aluminized plastic tube forming the grounded cathode. Because each sense wire has its own source of electric field, straw tube chambers can be operated reliably in higher rate environments. They also have the additional benefit of being more reliable since a single broken wire only impacts one channel. The straw tubes operate reliably in high radiation fields - no aging effects have been seen up to  $2C/cm$  [138]. Straw chambers have several advantages over conventional wire chambers:

- the cylindrical geometry of the straw tube results in good electrostatic and mechanical stability;
- broken wires are insulated from other wires and do not compromise seriously the data from the detector while inaccessible for repair;
- the self-supporting property of the straw allows optimal straw orientations without strong external frames;

The straw wall is made of a multilayer Kapton film (2 layers of  $50 \mu m$  Du Pont VN200 film covered with  $0.2 \mu m$  Al +  $4 \mu m$  Carbon +  $3-4 \mu m$  of polyurethane welding layer). The total thickness of the straw wall is around  $120 \mu m$  resulting

in an 7.74 mm outer straw diameter. The straws are assembled in a 3 layer array by gluing the straws densely packed, using a specially developed technology. This technology utilises precise templates and special glue (liquid epoxy resin), so that an accuracy of the straw position in the straw array of better than  $50 \mu\text{m}$  can be achieved. While the glued straw array is fixed in the precise tooling, strips made of high Young's modulus carbon fibres are glued to the straws on the top and bottom of the straw array.

Angular acceptance	$5^\circ - 25^\circ$
Number of straw tubes	11040
Straw tube outward diameter	7.740 mm
Straw tube wall thickness	$\sim 120\mu\text{m}$
Straw tube length	15-83 cm
Number of straw layers in $z$	24
Max. drift time	80 ns
Radiation thickness	$\leq 15\%X_0$
Gas mixture Ar-CO <sub>2</sub>	80:20
Straw occupancy	
average	$\sim 8\%$
local in DIS jet	$\sim 20\%$
Single wire spatial resolution	$\sim 300\mu\text{m}$
Efficiency per straw	98.5%
Radiation hardness	$\geq 2\text{C/cm}$
Number of readout channels	2112

**Table 6.1:** The overall specification of the straw-tube tracker

The mechanical, electrical and operating properties of a similar straw tubes are now well understood as shown by RD-6 R&D programme for the ATLAS TRT detector [139].

The STT specifications are given in Table 6.1.

### 6.3.2 The STT readout electronics

The front-end electronics consists of two boards: the *main board* located close to the straws and the *cable driver board* installed on the rim of the detector. The *main* or multiplexing board performs the following tasks: shape and discriminate

the signals from the individual straws, multiplex six straws into one readout channel by introducing time delays in increments of  $\sim 200$  nsec.

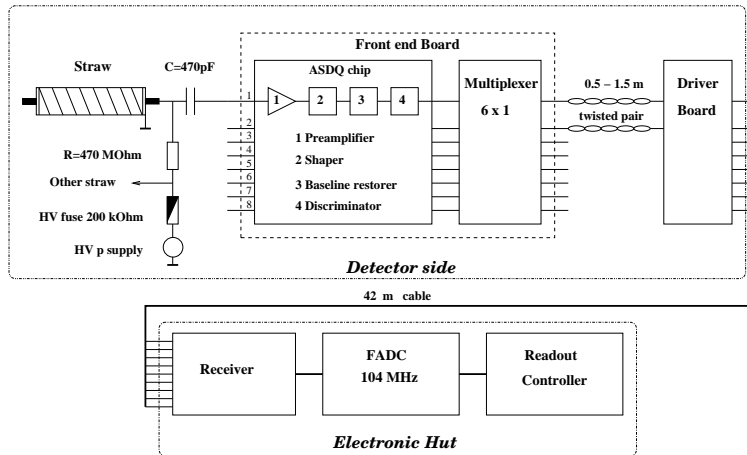


**Figure 6.7:** The STT readout.

The shaping and discriminating of the signals is done by the ASDQ chip developed by the University of Pennsylvania for CDF [140]. The signal path from the wires through the electronics is shown in figure 6.7.

Each standard main board contains electronics for 96 straws, whose signals are then fed into 16 readout channels. With this scheme the 10944 straws of the STT can be read out using the 1824 FADC channels available from the TRD.

### 6.3.3 The STT Monte-Carlo simulation

In order to verify the validity of the proposed upgrade solution for the real ZEUS FDET geometry and environment, a Monte Carlo simulation of a few possible variants of an STT design was performed. GEANT was used as well as dedicated routines for ionisation losses (now included in GEANT version 3.16 and following). The principal applications of GEANT are the tracking of particles through an experimental detector model for acceptance studies (i.e. the fraction of a certain physics process that are observed in a detector) or simulation of the detector response, and the graphical representation of the model and of the particle trajectories. In view of these applications, the GEANT system allows to:

- describe an experimental detector model in an efficient and simple way. The model is represented by a structure of geometrical volumes;

- generate simulated events from standard HEP Monte Carlo generators;
- control the transport of particles through the various regions of the detector model, taking into account the geometrical volume boundaries and relevant physical effects due to the nature of the particles themselves, to their interactions with matter and the effects of magnetic fields;
- record the elements of the particle trajectories and the response from the sensitive detectors;
- visualise the detector models and the particle trajectories;
- simulate the detector response;

A detailed geometrical description of the STT detector as well as the new forward beampipe and magnets was developed. Figures 6.9 and 6.10 illustrate the STT geometry structure in GEANT.

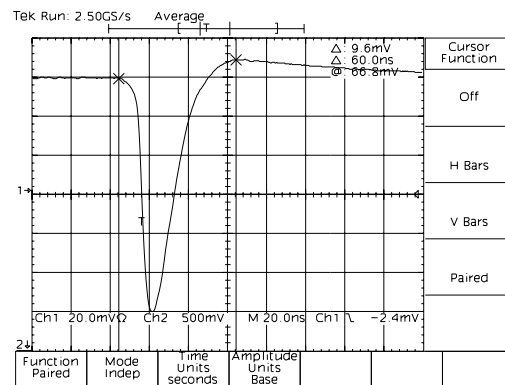


**Figure 6.8:** The average signal from monitor analog output ASDQ using  $^{55}\text{Fe}$  source. The gas mixture is Ar/Co<sub>2</sub> 80/20, HV=1850 V.

The dedicated simulation program was developed in order to simulate the performance of the straws. The description of the physical processes occurring in the straws was made as realistic as possible. The straw simulation model includes:

- The straw attenuation length of  $\sim 2$  m,
- The signal propagation time of  $\sim 4$  ns/m,

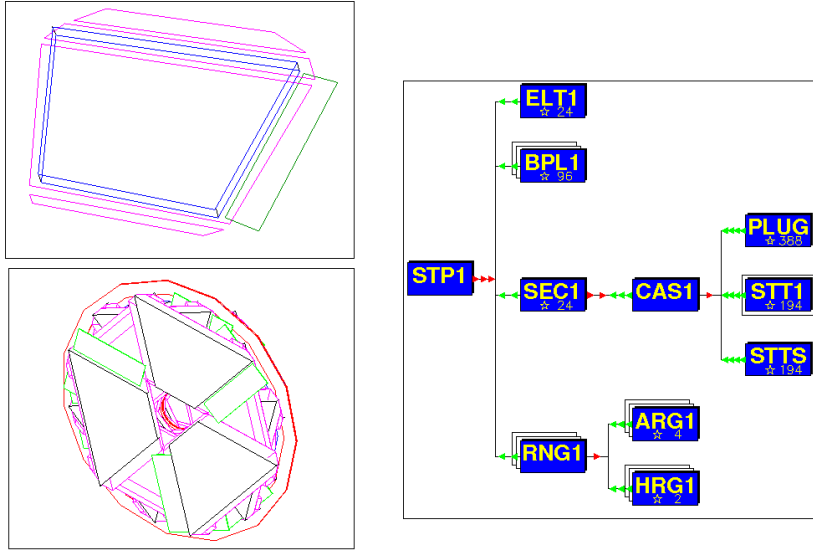


**Figure 6.9:** The STT geometry structure in the GEANT simulation. Parts of a sector (top left) the STT half with a support structure (bottom left) and the STT geometry tree in GEANT.

- The signal reflection from the far end of the straw,
- The signal shaping  $A(t)$ , using a real signal shape from an  $^{55}\text{Fe}$  source (Fig. 6.8),
- Ionisation in the straws, computed as a number of clusters on the particle track. The probability for a given distance  $x$  between collisions in the gas is

$$W(x) = \exp(-x/x_0), \quad (6.1)$$

where  $x_0 = L/N_{cl}$ ,  $L$  is the length of the track in the straw and  $N_{cl}$  is the average number of clusters per unit length. The energy of these clusters,  $E_{cl}$ , is calculated on the basis of the photoabsorption ionization (PAI) model [141]. In thin layers, the Landau model of energy loss fluctuations is not valid, because the number of collisions is too small. In this case, the atomic structure of the atom has to be taken into account. The PAI model uses the photoelectric cross-sections to describe the energy loss distribution.

- Electronics noise, simulated as

$$A_{noise}(t) = E_n \sin(2\pi\omega t + 2\pi P) \quad (6.2)$$

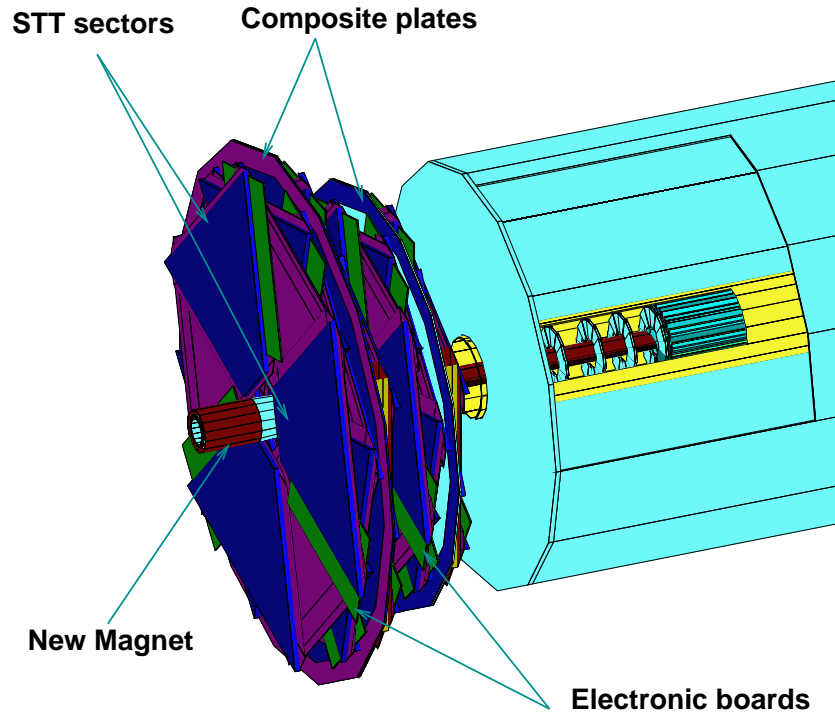


**Figure 6.10:** Full STT detector and new magnets in GEANT.

where  $E_n$  is distributed following a Gaussian of  $\sim 70$  eV resolution and  $P$  is a random number between 0 and 1, and  $\omega$  defined according to the ASDQ shaper characteristic ( $\omega = 25$  MHz),

- Gas gain fluctuations are also taken into account

$$\sigma_{Ecl} \sim 0.25 \cdot \sqrt{Ecl} \quad (6.3)$$

with  $Ecl$  in keV (the energy resolution  $\sim 25\%$  at FWHM for cluster energies of 6 keV from an  $^{55}\text{Fe}$  source,

- The dependence of the drift velocity on electric field, taken from the MAGBOLZ program [142],

The output signal amplitude is then defined as:

$$A_{out}(t) = \sum_i E_{cl}^i A(t - t_i) + A_{noise}(t), \quad (6.4)$$

where  $t_i$  is a drift time measured for given cluster.

The straw model was compared to the data from the test beam and data taking with the ZEUS detector.

Simulation of the electrons drift for the STT straw tubes shown in fig. 6.11. Figures 6.12 and 6.13 show a drift time vs drift distance distributions for test beam data and 2004 data taking period compared to GEANT simulation. The GEANT simulation of the STT straw tube drift time measurements is in a good agreement with real data.

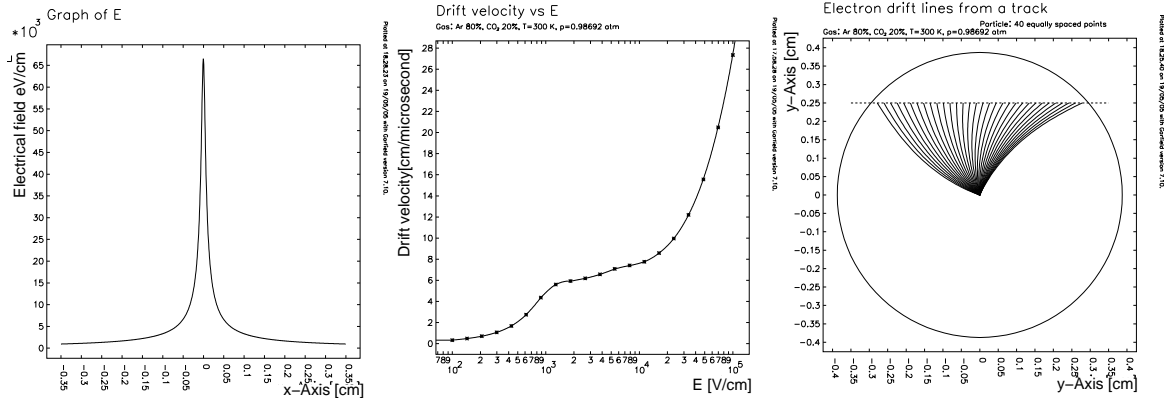


**Figure 6.11:** Simulation of the electrons drift for the STT straw tube.

The single straw efficiency as a function of the ASDQ threshold settings for test beam and the GEANT simulation is compared in Fig. 6.14. The value of threshold for simulation was obtained by matching a mean number of fired straws on STRECON track (see 6.3.4) for data taken during 2004 run period and GEANT simulation(see Fig. 6.15). The discriminator threshold corresponds to a single straw efficiency of about 88 – 96% depending on particle Lorenz factor (see Fig. 6.14).

Figure 6.16 shows a single straw drift radius measurement resolution for test beam data and the STT GEANT simulation.

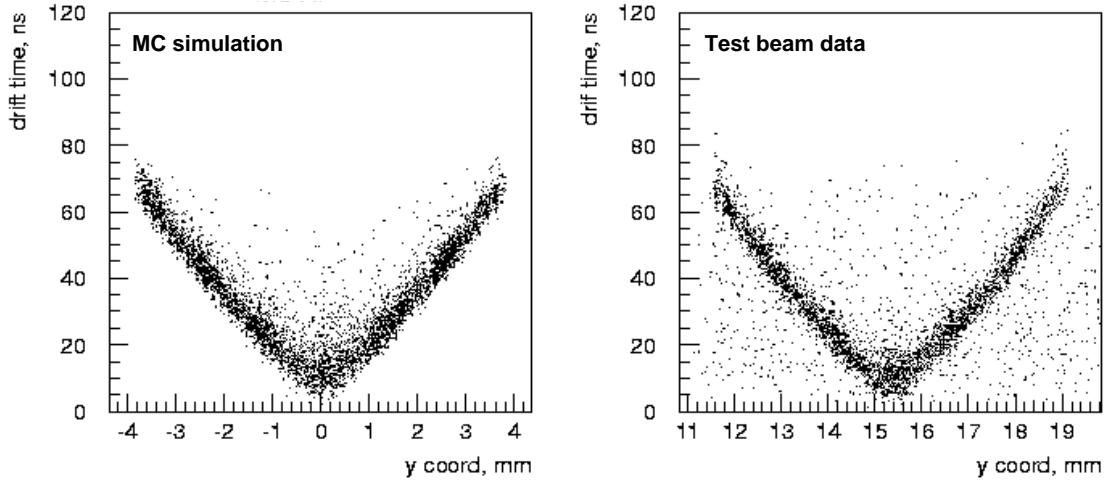


Figure 6.12: Drift time vs drift distance, Monte Carlo (left) and test beam data (right) using 1 ns clock TDC.

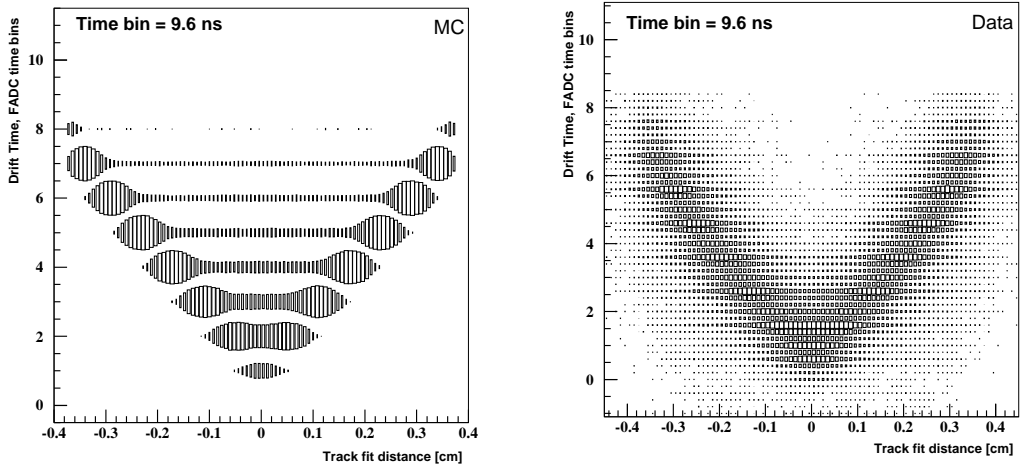
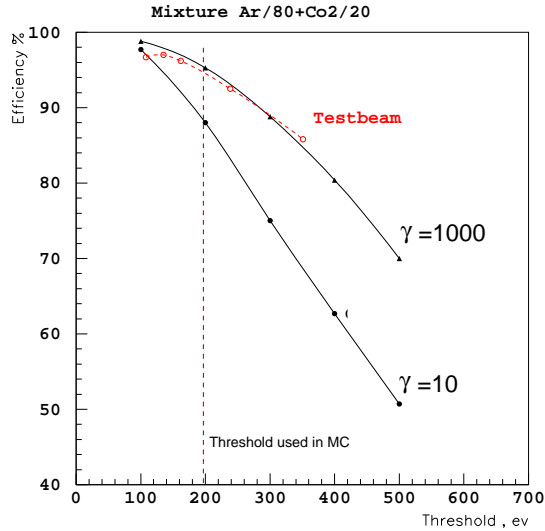
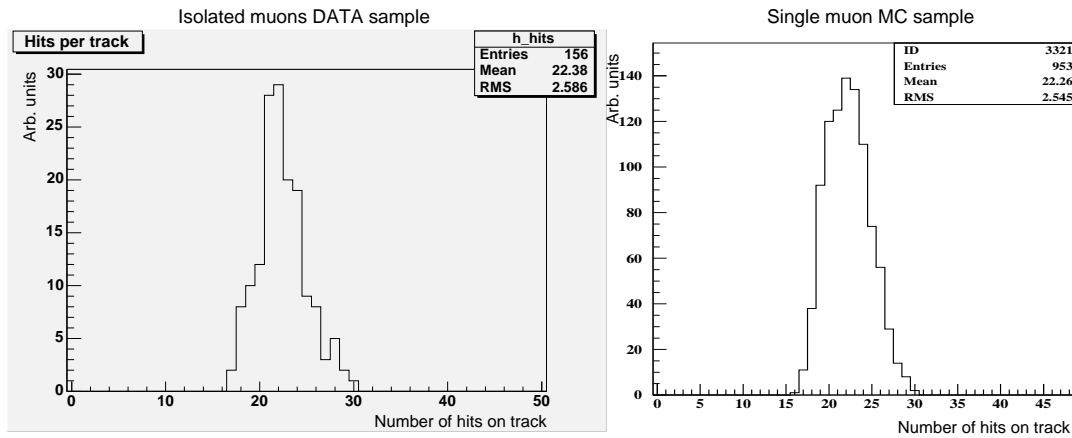


Figure 6.13: Drift time vs drift distance distribution for MC data and 2004 data data taking, using 104 MHz FADC.

In general, the GEANT simulation of the STT performance are in good agreement with the test beam data and data taken with the ZEUS detector.



**Figure 6.14:** Single straw efficiency for different Lorentz factor of ionising particle MC data (solid) and the test beam data (dashed).



**Figure 6.15:** Number of straws used in STRECON track candidate for real data (left) and MC data (right).

### 6.3.4 The STT pattern recognition program STRECON

The most important task of the STT is to find tracks with high efficiency in the forward region of the ZEUS detector. The MVD and FTDs have good resolution,

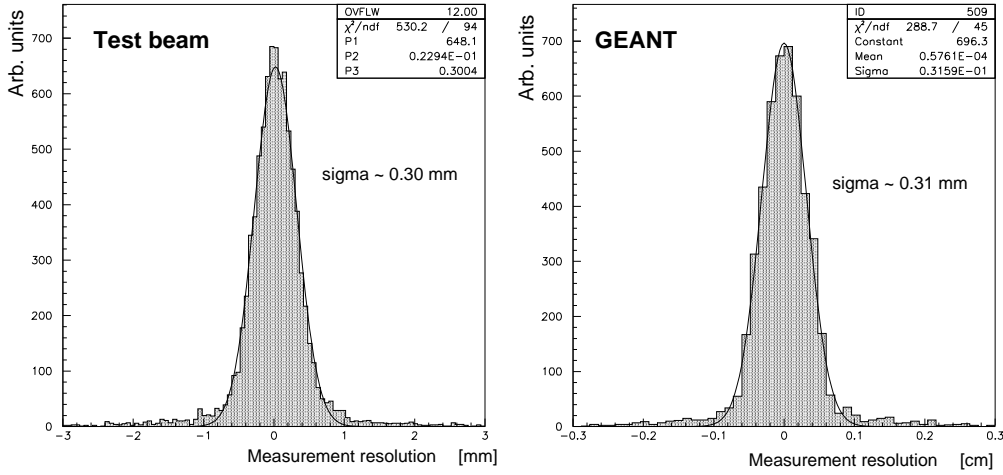


**Figure 6.16:** Single straw drift radius measurement resolution for test beam data(left) and the STT GEANT simulation (right).

however due to the limited number of micro-vertex layers and the large cell size in the FTD's, pattern finding is difficult in high multiplicity events. The idea is first to find tracks with high efficiency using STT alone and then to combine this information with that from the FTDs, the CTD and the MVD to construct high precision tracks. We developed the STRECON pattern finding and track fitting program.

The STRECON pattern finding is based on Histogramming method. Histogramming can be regarded as a discrete implementation of the Hough transform [144]. Hit information is converted to a constraint in a binned feature space, and the frequency of entries in a bin above a certain limit is indicative for a track candidate. However, a single measurement is not sufficient to constrain all track parameters. One solution is then to convert each measurement into a discretized curve in parameter space, and to sample the contribution of all hits in corresponding accumulator cells. This technique is implemented is the STT pattern finding. Figure 6.17 shows the STT measurement structure. The straws are arranged in the four different stereo views  $0^\circ$ ,  $\pm 15^\circ$  and  $30^\circ$ . Each hit provides an arc-like constraint in the parameter space spanned by polar angle  $\theta$  and the azimuth angle  $\phi$ . This structure is displayed in the histogram from four views for a single track in fig. 6.18. The parameters of the track are clearly indicated by the

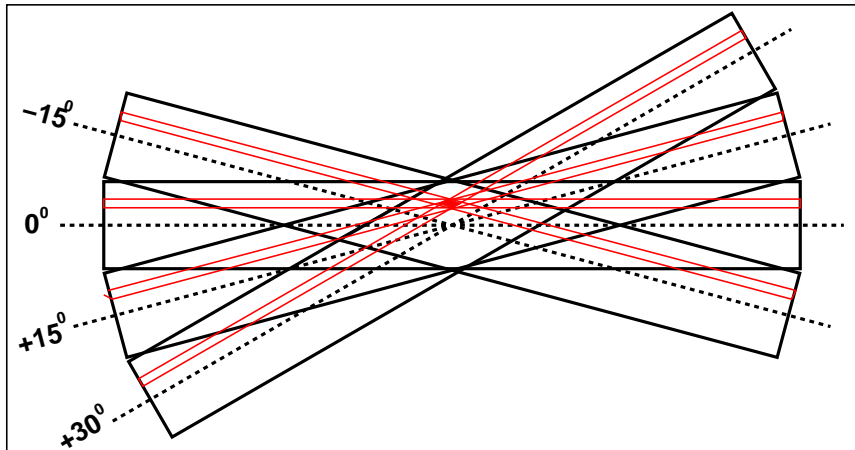


**Figure 6.17:** Wire orientations in the ZEUS straw-tube tracker. In this representation, the beam is oriented vertical to the page, displaced towards the bottom of the page.

intersection of the four constraints that define a spike. The resulting histogram is already much more complex in a NC DIS sample, where combinatorial overlaps occur (fig. 6.19).

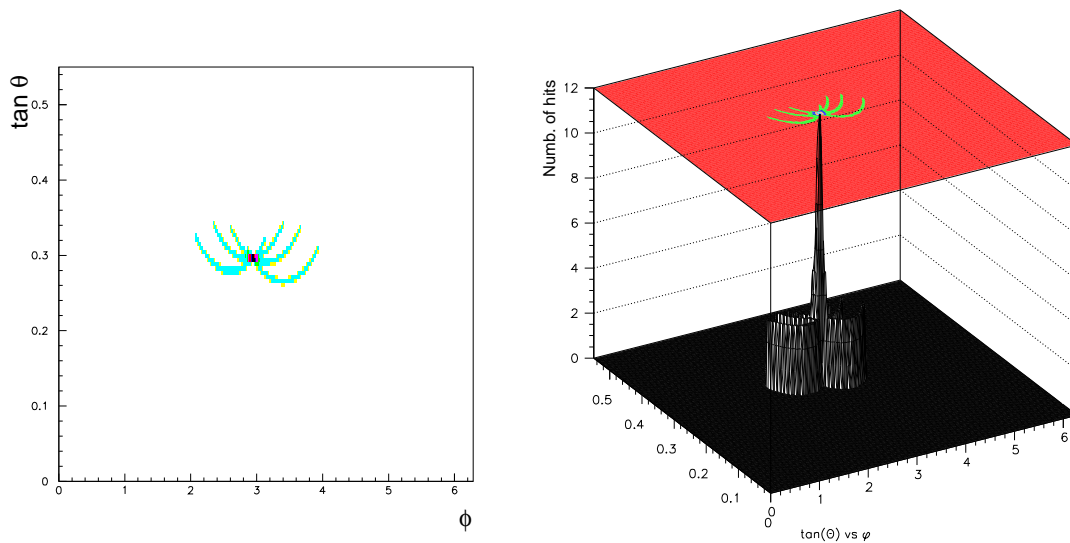


**Figure 6.18:** Hough transform of a single simulated track in the ZEUS straw-tube tracker.

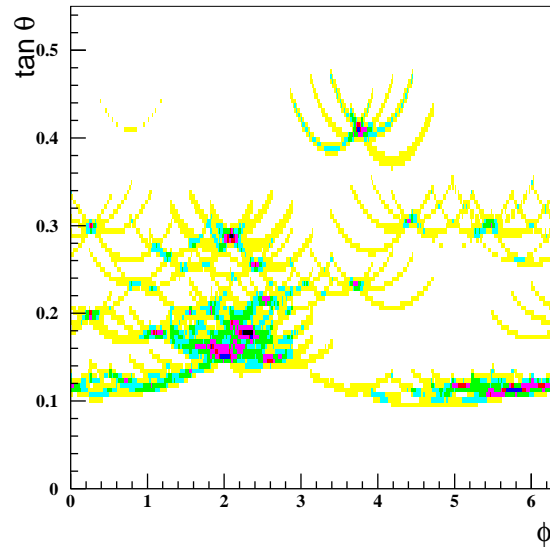


**Figure 6.19:** Hough transform of a set of simulated tracks in the ZEUS straw-tube tracker.

Because of the inhomogeneous magnetic field and the inactive material in the forward region of the ZEUS detector, it is not possible to reconstruct a track as a single helix in the entire detector. The reconstruction is therefore based on a hit-to-hit helix extrapolation in a piecewise constant magnetic field.

In a first step histogramming method provides a group of hits for every track candidate in STT1 and STT2. A track seeds in the wide spikes are built using a combinatorial procedure. In the second step a 3D hit-to-hit helix fit takes place where the helix parameters are determined by minimization of the estimated covariance matrix (Kalman filter). In the last step, (see Fig. 6.20) the reconstructed track elements in STT1 and STT2 are matched and an overall fit to all hits belonging to this track candidate is made.

The STRECON package has been running in the ZEUS reconstruction ZEPHYR since 2001 and provides information on:

- STT only track candidates and helix parameters.
- STT candidates matching with FTD1 and FTD3 track segments and combined fit.

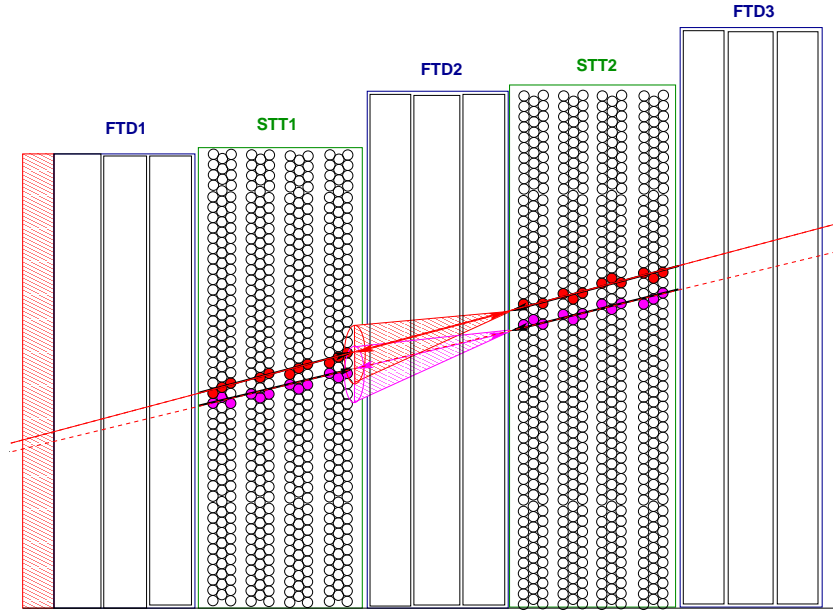


**Figure 6.20:** Schematic view of the STT1 and STT2 candidates matching.

- STT/FTD candidates matching with CTD/MVD candidate.
- Z coordinate of an event vertex position (see fig. 6.21).
- Extrapolation of STT/FTD track candidate on the FCAL surface.

Adapted STRECON is used in the ZEUS third level trigger.

The STRECON efficiency was studied using MC and real data. The table 6.2 summarizes the efficiency values for different MC samples.

Sample	Momentum range (GeV)	Efficiency %
Single $\mu$ tracks	$\geq 1$	$97 \pm 1$
5 $\mu$ in $5^\circ$ cone	$\geq 1$	$85 \pm 1$
Single electron	10	$80 \pm 1$
NC $Q^2 > 100 \text{ GeV}^2$	$\geq 0.5$	$80 \pm 1$

**Table 6.2:** Pattern finding efficiency using STT alone determined using MC simulation.

The single track efficiency of the STRECON is below 100% because of a compromise between track finding efficiency and CPU time consumption.

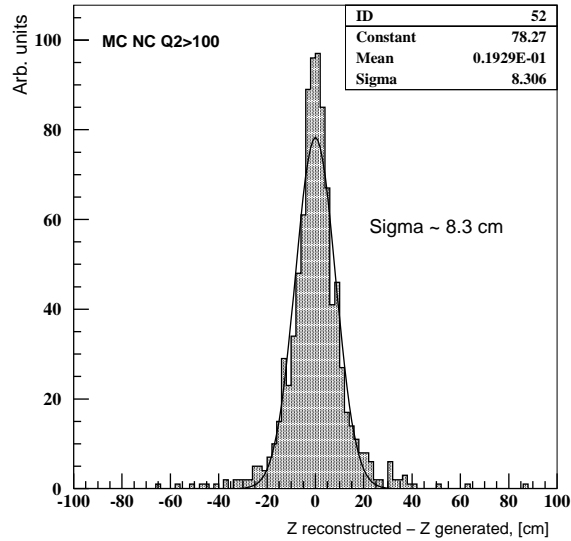


**Figure 6.21:** The STRECON resolution of primary vertex  $Z$  position.

Another reason is a smaller than expected single straw efficiency (88 – 96% fig. 6.14) as a threshold used during data taking is higher than threshold used on test beam.

The efficiency evaluation method using MC is based on hit matching technique from [145]. Track candidate defined as found if number of common hits (fired straws) with a fiducial GEANT track is greater than 70%. A fiducial GEANT track defined by:

- MC track comes from primary vertex vicinity (within a sphere of 10 cm radius);
- MC track has a polar angle within the STT acceptance;
- MC track momentum  $\geq 1 \text{ GeV}$  ( $p_t \sim 250 \text{ MeV}$ );

The STREON efficiency dependence on polar angle and momentum of a track for MC DIS sample is given in fig. 6.22. The main reason for efficiency losses is a presence of large amount of inactive material right after the CTD ( $\sim 55\%X_0$ ) and the new magnet installed in a region of the STT2. Figures 6.23 shows the

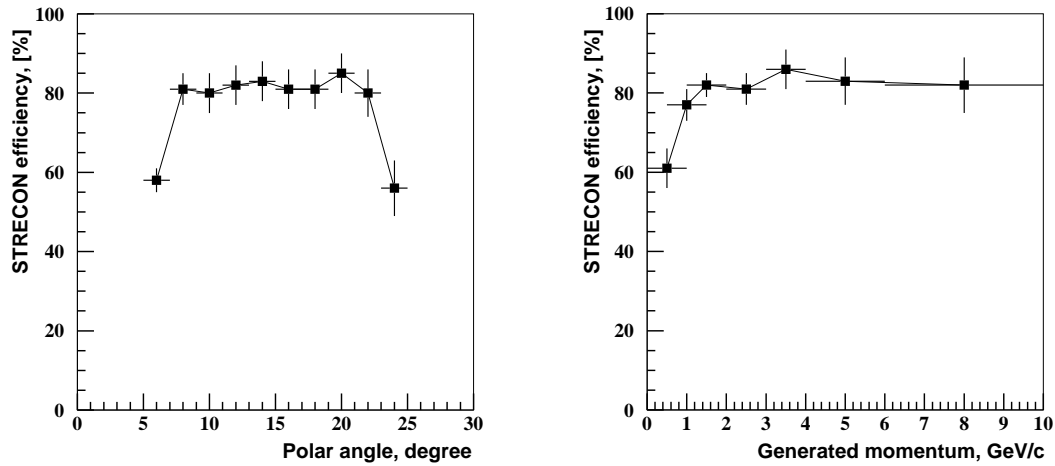


**Figure 6.22:** The STRECON efficiency dependence on polar angle (left) and generated momentum (right) for MC DIS sample.

occupancy distribution in the STT. There is a large increase of occupancy in the STT2 close to beampipe. The main reason for large occupancy (up to 25%) in the STT2 is a secondary interaction of particles with a material of the new magnet. Inactive material distribution in the forward region of the ZEUS detector shown in fig. 6.24. The distribution illustrates an amount of material collected on a GEANT track from vertex to FCAL surface. An amount of inactive material for a track with polar angle larger than  $10^\circ$  is about  $100\% X_0$  increasing to  $170\% X_0$  below  $10^\circ$  degree.

An effect of inactive material in the ZEUS forward region was studied using the GEANT simulation. Figure 6.25 shows the difference of the STRECON track finding efficiency for the same MC sample but with secondary interactions OFF and ON in the GEANT. An efficiency decrease of about 10% was observed. Figure 6.36 shows an example of the GEANT simulated event display with effects of inactive material ON and OFF. There is a clear indication of photon conversions, bremsstrahlung, and other processes that lead to a significant increase of the STT occupancy.

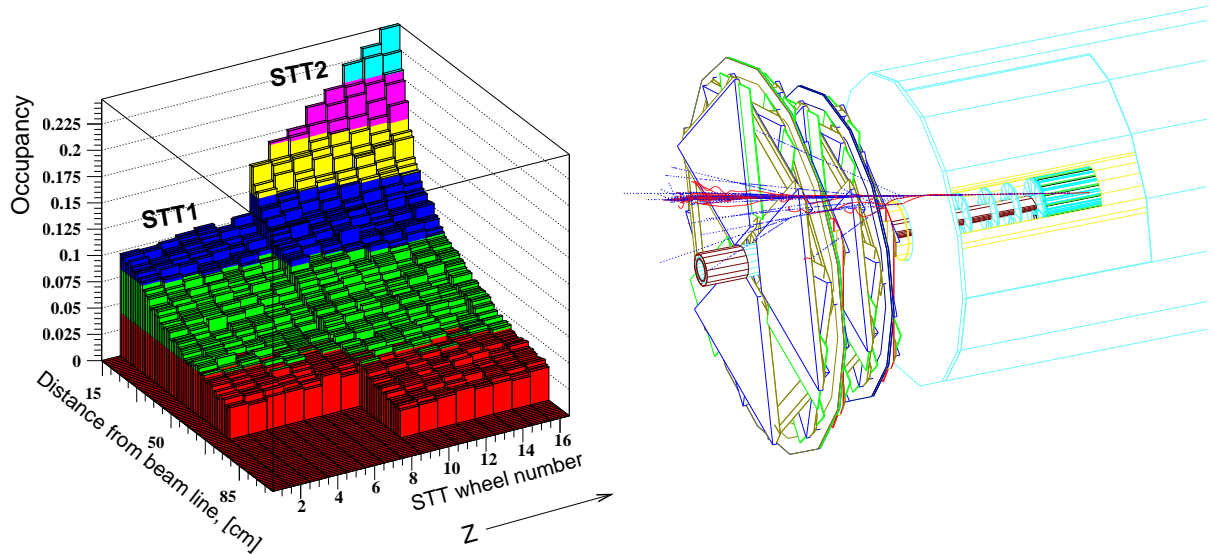


**Figure 6.23:** The occupancy distribution in the STT (MC DIS sample) as a function of straw Z and R positions (left) and single electron track GEANT simulation (right).

### 6.3.5 Study of the STT performance with real data

The STT detector performance with a real data and a comparison with MC presented here. A typical DQM distributions used during data taking shown on figures 6.26, 6.27. Figure 6.26 shows number of fired straws in STT per event, number of found STRECON track and a pseudorapidity of the candidates. Figure 6.27 illustrates the CPU time to reconstruct one event depending on the even data size. The STRECON CPU time to reconstruct average event ( $\sim 825$  fired straws) is about 100 milliseconds. In general the STRECON time consumption is about 70% of VCRECON reconstruction package.

#### 6.3.5.1 Drift time measurements calibration and alignment.

The STT consists of 11040 straws and the readout chain of every straw tube have some deviations of parameters from the design values. This leads to a smearing of time delays of all straws. An example of the FADC pulstrain (128 time bins) is shown in figure 6.28. One FADC pulstrain contains drift time spectra of six straws in one readout channel. The STT drift time measurements can be used

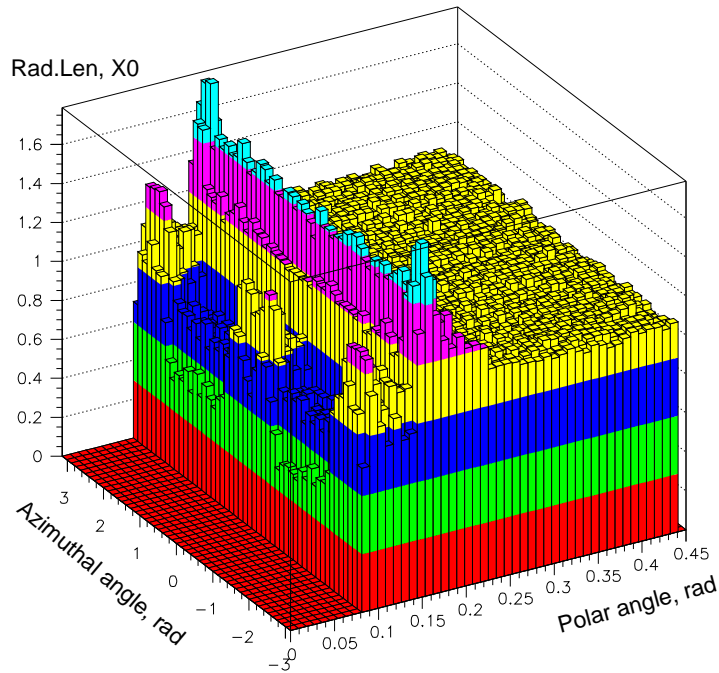


**Figure 6.24:** Amount of material collected on a forward track from vertex to FCAL surface.

only if time reference of all straws is defined. T0 calibration was made during data taking period using fit of a drift time spectrum of every straw. The fit allows to define a slope of the spectrum leading edge and T0 respectively. Figure 6.29 shows an average over the STT T0 values for runs covering 2004 and 2006 data taking periods. The error bars indicates an RMS of T0 distribution.

The average STT T0 is rather stable, that's why only three T0 sets are defined and used. One set of T0's for all STT straws used for 2004 and two sets used for 2006 data taking period.

Another important step to obtain a best resolution for every tracking detector is an alignment with respect to other tracking detectors (global) and internal alignment of sensitive elements (local). The STT was aligned with respect to the central tracks (CTD/MVD). The STRECON track candidates were used to find relative shifts of the STT sectors. Figure 6.30 shows a distribution of mean

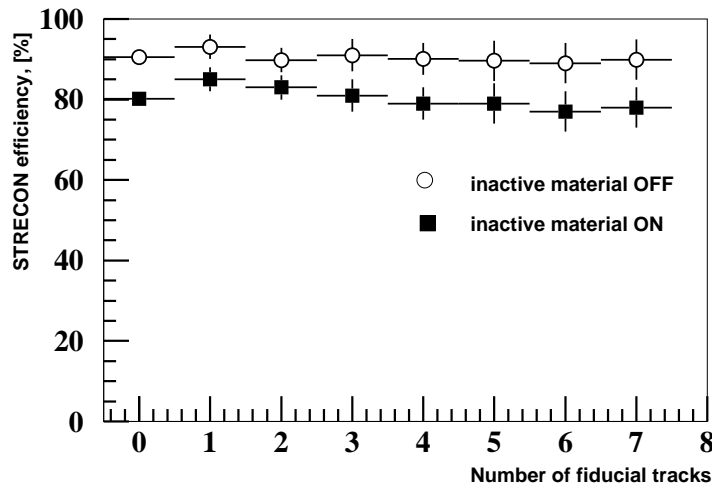


**Figure 6.25:** The STRECON efficiency dependence on number of fiducial tracks in event for MC DIS sample. Open circles is an efficiency for the MC sample with all processes of particles interaction with material switched off in GEANT. Reconstruction efficiency with all processes simulated in GEANT is indicated by filled squares. Points at zero show an average efficiency.

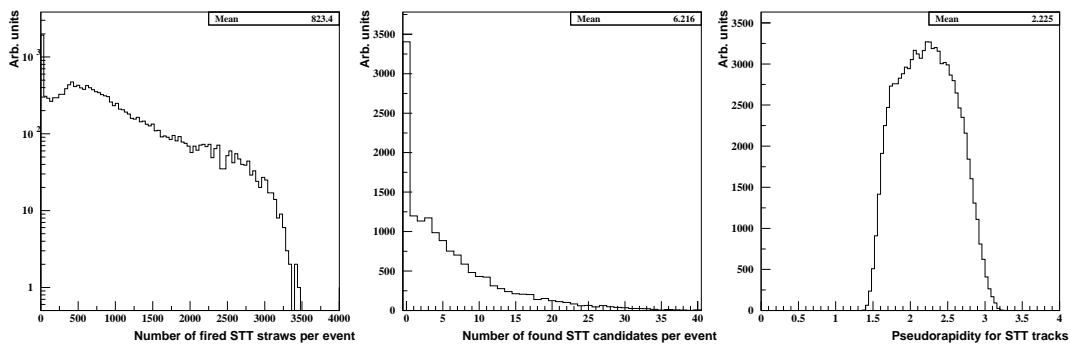


**Figure 6.26:** Example of STT reconstruction for data taken in a year 2004. Number of fired STT straws per event (left), number of found STT candidates per event (middle) and pseudorapidity of found STT candidates (right).

values of residuals between the STRECON track fit and the straw drift radius measurement. The error bars indicate the RMS of the residuals distribution.

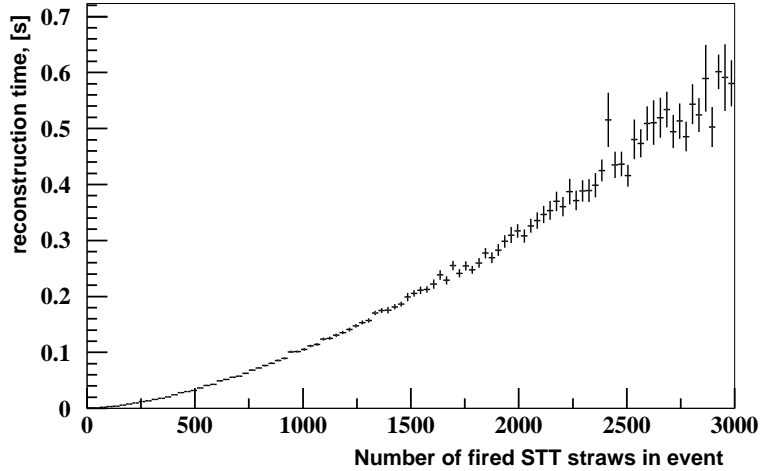


**Figure 6.27:** The STRECON CPU time consumption for one event.

There is an obvious improvement of shifts after alignment but there are still sizable deviations from zero. The remaining shifts could be removed by the next iteration of alignment. Another opportunity is to use CTD/MVD/STT combined tracks that have better accuracy.

Figure 6.31 shows a distribution of residuals between the STRECON track fit position and a straw drift radius measurement. The left and central figures present the residuals before and after alignment. There is a distinct improvement of mean value and a width of the distribution.

A comparison of 2004 data and MC sigmas of the residuals are shown in figure 6.31 (right). The average value of the residuals sigma is about  $430 \mu\text{m}$  which is in good agreement with the GEANT simulation. There are several reasons explaining the wider residuals distribution in comparison to obtained with the test beam ( $\sim 330 \mu\text{m}$  [143])

- larger discriminator threshold and smaller average particle energy (Lorenz factor) in a data than in a test beam. This leads to smaller ionization energy depositions and smaller measurement accuracy;
- large occupancy in the STT gives a sizable amount of wrong straws used in the STRECON fit;
- remaining misalignment;

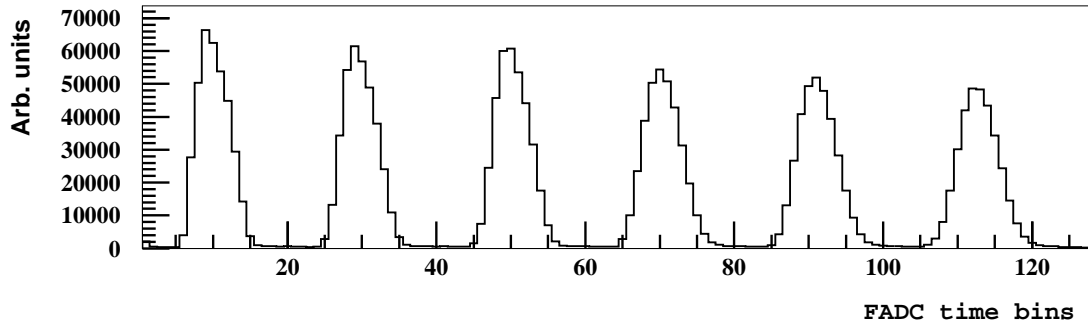


**Figure 6.28:** The STT FADC pulstrain example for data taken in a year 2004. Pulstrain contains drift time spectra of 6 straws combined in one read-out channel.

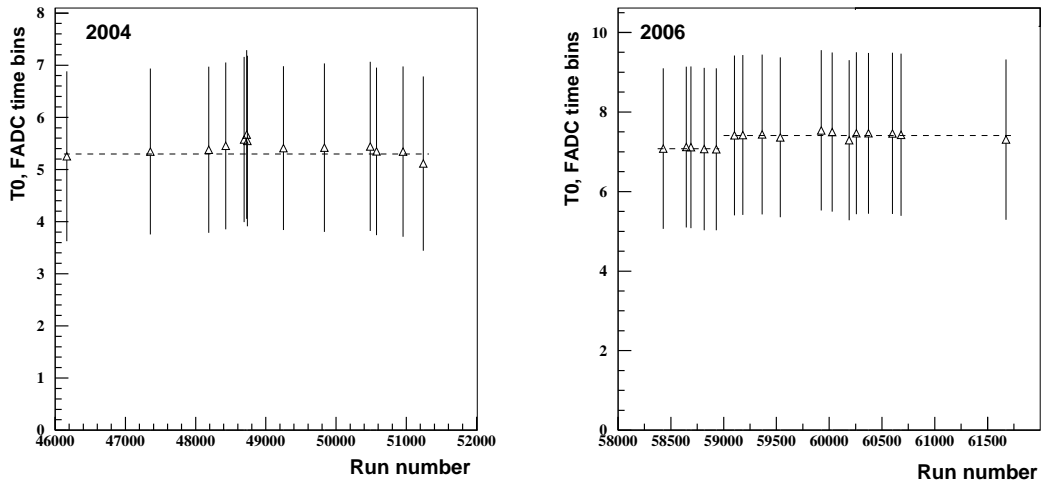


**Figure 6.29:** The STT average  $T_0$  for 2004 (right) and 2006 (left). The error bars indicates an RMS of  $T_0$  distribution.

### 6.3.5.2 The STRECON efficiency

The STRECON efficiency in data was evaluated by matching STT track candidates with ZEUS central region CTD/MVD candidates.

The CTD/MVD track candidates extrapolated to STT region are matched with the STT standalone candidate if a distance between them on a plane perpendicular to the beam line is less than 5cm.

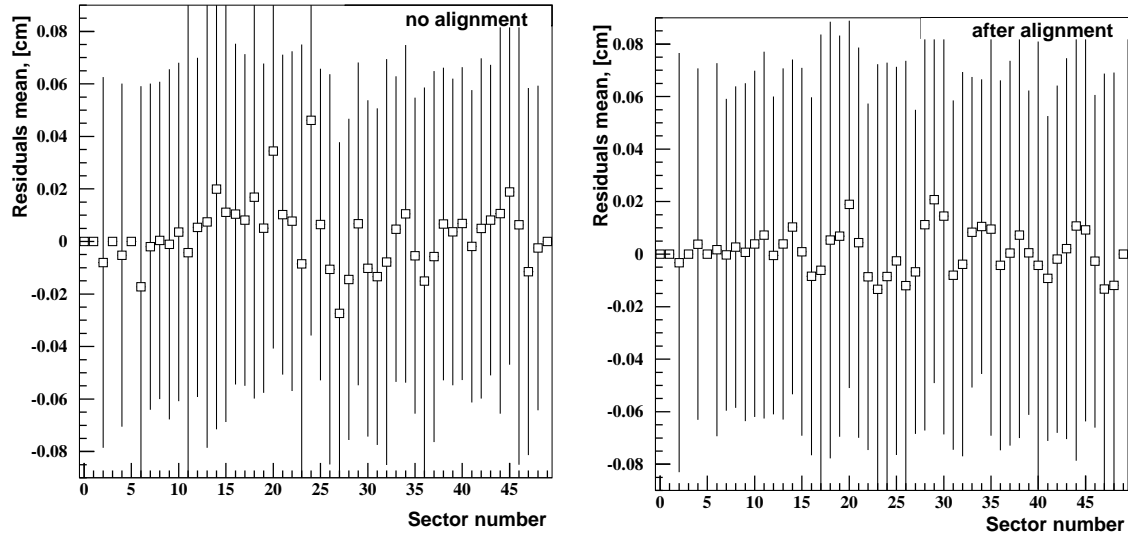


**Figure 6.30:** The mean values of residuals between STRECON fit and drift radius measurement. for all STT sectors without alignment (left) and with alignment (right). The error bars indicates an RMS of residuals distribution.

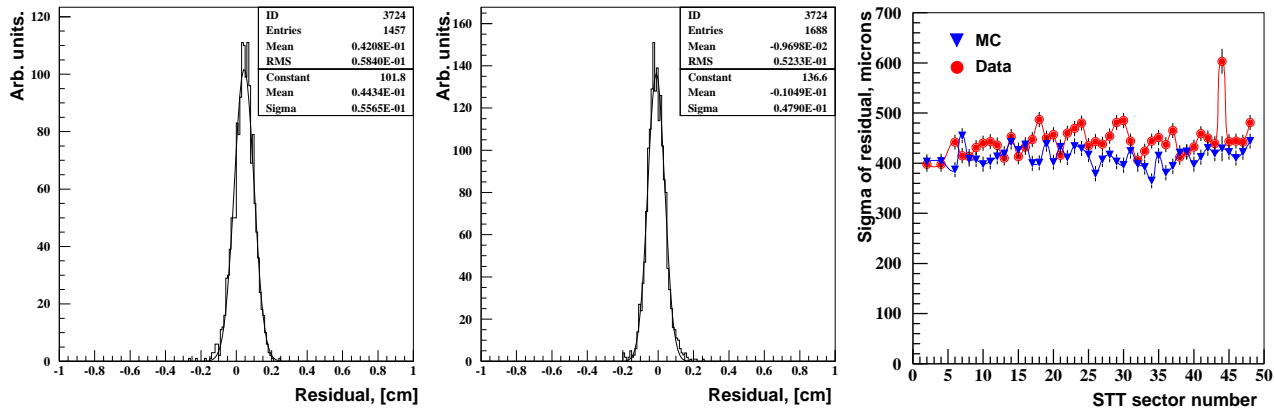


**Figure 6.31:** Distribution of residuals between the STRECON track fit position and a straw drift radius measurement. Left and central figures present the residuals before and after alignment applied. Comparison of 2004 data and MC (right) sigmas of residuals over all STT sectors.

This method only provides an estimation of the STRECON efficiency as CTD/MVD candidates in forward region have low purity. A requirement of central region candidate matching also with the FTD segments (FTD1,FTD2,FTD3) used as this decrease a probability that CTD/MVD is a ghost. This procedure allows comparison of MC with data and to evaluate the STT GEANT simulation quality.

The values of CTD/MVD to STT matching probabilities for NC DIS data sample from year 2004 and a MC NC DIS sample are summarized in table 6.3.

CTD/MVD matching with	DATA %	MC %
STT only	$67\pm 1$	$70\pm 1$
STT + FTD1	$77\pm 1$	$78\pm 1$
STT + all FTDs	$88\pm 2$	$88\pm 2$

**Table 6.3:** CTD/MVD to STT matching probability for DATA and MC.

An increase of matching probability with an extra FTD segments requirement indicates the better quality of CTD/MVD candidates used.

In general, a very good agreement between DATA and MC simulation is found. To achieve this agreement the dead straws map were built and used during the reconstruction of GEANT simulation.

Figure 6.32 shows a total amount of non working straws in the STT during 2004, 2006 data taking. The STT was off in year 2005 because of an issue with excessive STT heat dissipation that was solved during shutdown in December 2005. The number of empty STT straws is gradually increasing. The fraction of empty straws is about 8% for 2004 and  $\sim 15\%$  by the end of 2006.

### 6.3.6 Conclusions

During the HERA luminosity upgrade the ZEUS detector was upgraded with the Straw-Tube-Tracker. In this Chapter we have presented the description of developed GEANT simulation and track reconstruction software for the STT. The STT GEANT simulation provides the STT performance simulation that is very close to test beam data studies and data taking values. The STT measurement structure and accuracies are well understood and reproduced in Monte Carlo simulation.

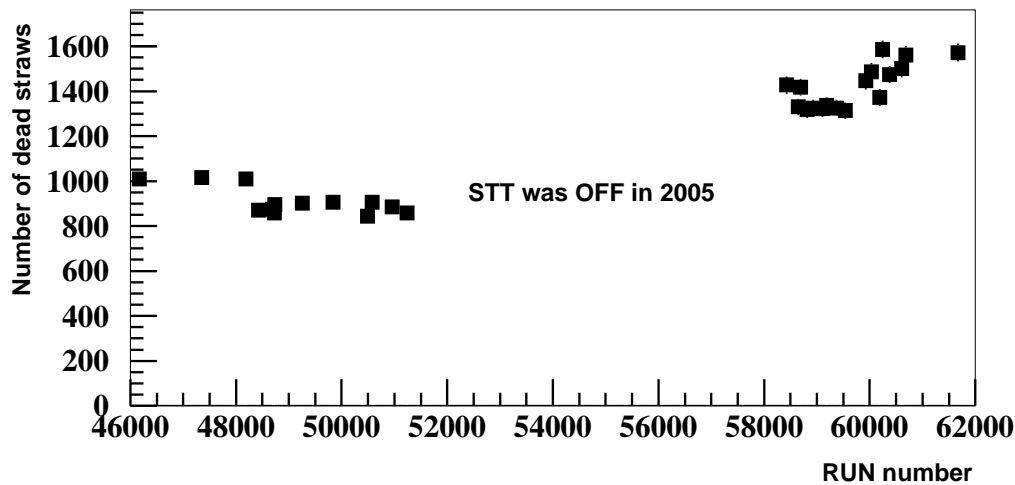


**Figure 6.32:** Number of dead straws in the STT during 2004–2006 data taking.

The STT standalone track finding and fitting tool developed. Figures 6.33, 6.34, 6.37 shows tracks reconstructed in forward region of the ZEUS detector using the STRECON. The STRECON provides:

- STT only track candidates and helix parameters.
- STT candidates matching with FTD1 and FTD3 track segments and combined fit.
- STT/FTD candidates matching with CTD/MVD candidate.
- Z coordinate of an event vertex position.
- Extrapolation of STT/FTD track candidate on the FCAL surface.
- Adapted STRECON is used in the ZEUS third level trigger.

The STRECON performance with real data was studied and compared to MC data. Good agreement between real data and MC found for the efficiency of tracking and drift radius measurement residuals. The STRECON average reconstruction efficiency for NC DIS sample is about 75–80% for MC data and real data. Main reasons for the efficiency losses are large occupancy in the STT and the detector hardware degradation.

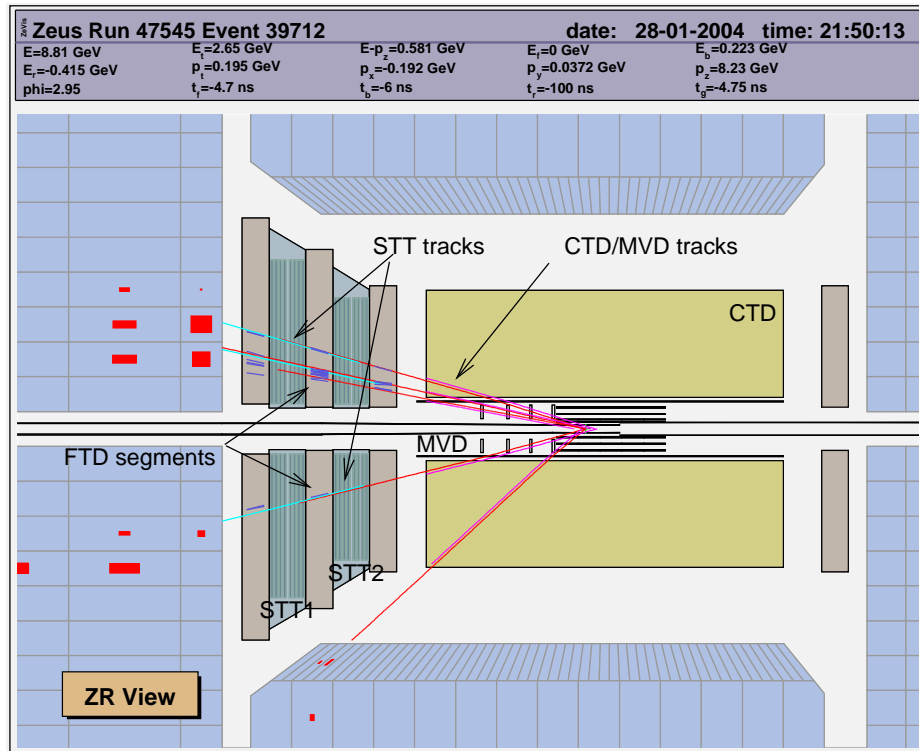


Figure 6.33: Reconstructed tracks in forward detector as seen at ZEUS event display.

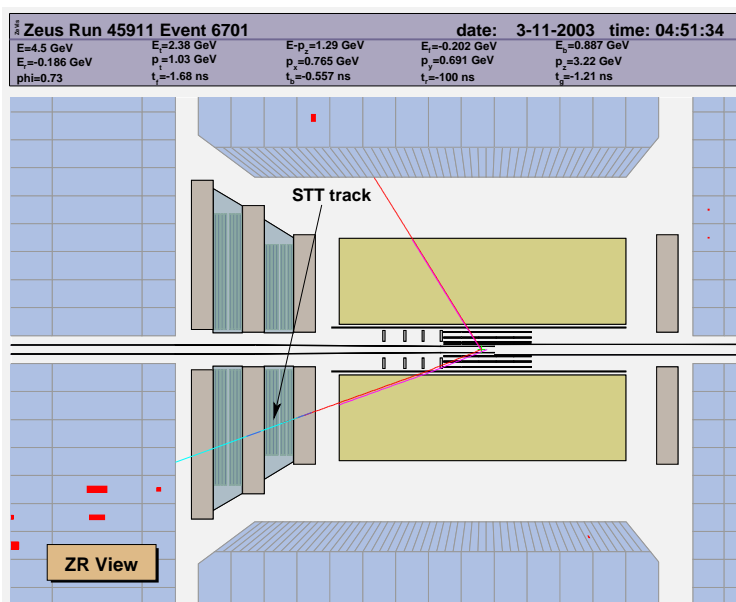


Figure 6.34: A muon from a decaying  $J/\psi$  has been measured in the STT.

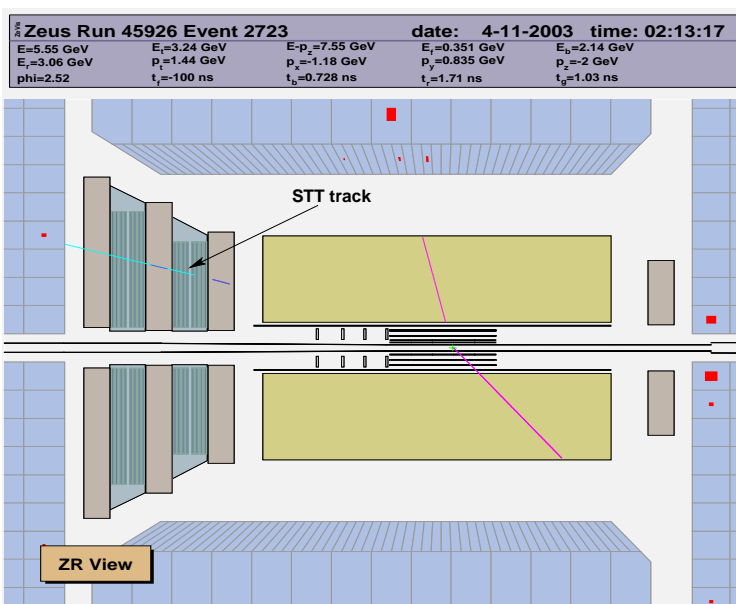
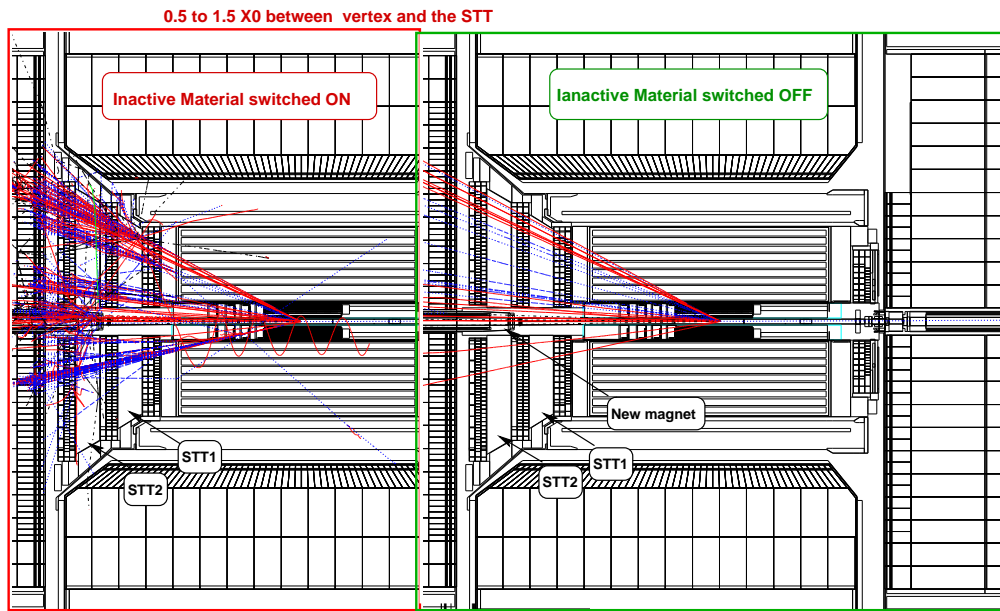
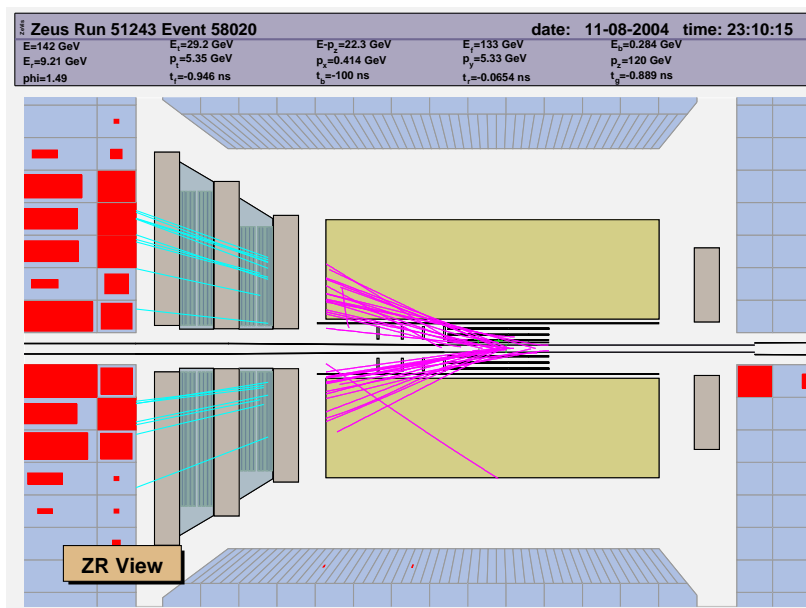


Figure 6.35: ZEUS event display with forward track reconstructed only in STT and FTD's.



**Figure 6.36:** The effect of inactive material in forward region of the ZEUS detector. GEANT simulated display of the same DIS event with all processes of interactions with material switched off (left) and on (right).



**Figure 6.37:** An event with two jets in forward region as seen at ZEUS event display.



# Chapter 7

## Summary and outlook

In this dissertation the measurements of total and single differential cross sections of inelastic  $J/\psi$  production in neutral current deep inelastic  $e^+p$  scattering, have been presented.

The measurements were performed with the ZEUS detector at HERA using an integrated luminosity of  $109\text{pb}^{-1}$ . The  $J/\psi$  mesons were identified using the decay channel  $J/\psi \rightarrow \mu^+\mu^-$ . The measurements were performed in the kinematic range  $2 < Q^2 < 80 \text{ GeV}^2$ ,  $50 < W < 250 \text{ GeV}$ ,  $0.2 < z < 0.9$  and  $-1.6 < Y_{lab} < 1.3$ , where  $Q^2$  is the virtuality of the exchanged photon,  $W$  is the photon-proton centre-of-mass energy,  $z$  is the fraction of the photon energy carried by the  $J/\psi$  meson in the proton rest frame and  $Y_{lab}$  is the rapidity of the  $J/\psi$  in the laboratory frame. The measured cross sections are compared to theoretical predictions within the non-relativistic QCD framework including colour-singlet and colour-octet contributions, as well as to predictions based on the  $k_T$ -factorisation approach. Calculations of the colour-singlet process generally agree with the data, whereas inclusion of colour-octet terms spoils this agreement.

From similar studies in photoproduction it is known that resummation techniques for soft gluon emission can improve the theoretical description, however such calculations are not available for DIS. NLO calculations are also not yet available in DIS. CASCADE Monte Carlo predictions are above the data but the shapes are well described. A calculation in the  $k_T$ -factorisation approach based on the BFKL evolution equations gives the best description of the data.

The measurements were performed with the ZEUS detector first time. The data are in agreement with the H1 results in the kinematic region  $2 < Q^2 < 100 \text{ GeV}^2$ ,  $50 < W < 225 \text{ GeV}$ ,  $0.3 < z < 0.9$  and  $p_T^{*2} > 1 \text{ GeV}^2$ .

The measurements can not give a basis for strong conclusions as statistical errors rather large. But we can state that theoretical description of the inelastic  $J/\psi$  production in DIS within the non-relativistic QCD framework requires further developments.

The results of  $J/\psi$  polarization measurements at the Tevatron [146] show strong disagreement with the NRQCD prediction. All this indicates that there is some aspect of the  $J/\psi$  production mechanism that is not yet understood. Further studies may lead to important new insight into the production of charmonium.

A more precise measurement of the studied process will be possible using the HERA II data.

During the HERA luminosity upgrade the ZEUS detector was upgraded with the Micro Vertex Detector and the Straw–Tube–Tracker. The later allows to find tracks with high efficiency in the forward region of the ZEUS detector.

In this dissertation we have presented the developed GEANT simulation and track reconstruction software for the STT. The STT GEANT simulation provides a performance simulation that is very close to test beam data studies and data taking values. The STT measurement structure and accuracies are well understood and reproduced in Monte Carlo simulation.

The STT standalone track finding and fitting tool was developed. The STRECON provides:

- STT only track candidates and helix parameters.
- STT candidates matching with FTD1 and FTD3 track segments and combined fit.
- STT/FTD candidates matching with CTD/MVD candidate.
- Z coordinate of an event vertex position.
- Extrapolation of STT/FTD track candidate on the FCAL surface.
- Adapted STRECON is used in the ZEUS third level trigger.

The STRECON performance with data was studied and compared to Monte Carlo (MC). Good agreement between data and MC found for a drift radius measurement accuracy and the efficiency of track finding.

The STRECON reconstruction efficiency for the NC DIS sample is about 75–80% for MC and data. Main reasons for the efficiency losses are large occupancy in the STT.

There are many physics issues that will benefit from the new detectors, in particular the reconstruction of high  $Q^2$  neutral current (NC) and charged current (CC) events and the tagging of events containing heavy quarks.



# Appendix A

## Values of the cross sections

In this Appendix the values and their uncertainties are given of the measured differential and normalised cross sections of the process  $ep \rightarrow eJ/\psi X$  in the kinematic region  $2 < Q^2 < 80 \text{ GeV}^2$ ,  $50 < W < 250 \text{ GeV}$ ,  $0.2 < z < 0.9$  and  $-1.6 < Y_{lab} < 1.3$ .

$z$ range	$d\sigma/dz$ (pb)	$1/\sigma d\sigma/dz$
0.20 – 0.45	$309 \pm 61^{+41}_{-34}$	$1.01 \pm 0.16^{+0.09}_{-0.08}$
0.45 – 0.60	$428 \pm 62^{+44}_{-32}$	$1.40 \pm 0.19^{+0.09}_{-0.06}$
0.60 – 0.75	$568 \pm 65^{+64}_{-55}$	$1.86 \pm 0.20^{+0.08}_{-0.13}$
0.75 – 0.90	$526 \pm 66^{+74}_{-47}$	$1.72 \pm 0.20^{+0.17}_{-0.15}$
$W$ range GeV	$d\sigma/dW$ (pb/GeV)	$1/\sigma d\sigma/dW$
50 – 100	$1.73 \pm 0.25^{+0.20}_{-0.16}$	$0.0056 \pm 0.0007^{+0.0005}_{-0.0005}$
100 – 125	$2.44 \pm 0.32^{+0.23}_{-0.20}$	$0.0080 \pm 0.0010^{+0.0004}_{-0.0005}$
125 – 175	$1.43 \pm 0.20^{+0.14}_{-0.12}$	$0.0047 \pm 0.0006^{+0.0003}_{-0.0003}$
175 – 250	$1.17 \pm 0.22^{+0.19}_{-0.17}$	$0.0038 \pm 0.0006^{+0.0004}_{-0.0004}$

**Table A.1:** Differential cross sections and normalised differential cross sections in the kinematic region  $2 < Q^2 < 80 \text{ GeV}^2$ ,  $50 < W < 250 \text{ GeV}$ ,  $0.2 < z < 0.9$  and  $-1.6 < Y_{lab} < 1.3$  as a function of  $z$  and  $W$ . The first uncertainty is statistical and the second is systematic. Overall normalisation uncertainties due to the luminosity measurement ( $\pm 2\%$ ) and to the  $J/\psi$  decay branching ratio ( $1.7\%$ ) are not included in the systematic error.

$Q^2$ range ( $\text{GeV}^2$ )	$d\sigma/dQ^2$ (pb/ $\text{GeV}^2$ )	$1/\sigma d\sigma/dQ^2$
2 – 4	$66.9 \pm 8.4^{+7.7}_{-6.8}$	$0.223 \pm 0.019^{+0.008}_{-0.012}$
4 – 8	$18.3 \pm 2.7^{+1.6}_{-1.3}$	$0.0609 \pm 0.0079^{+0.0033}_{-0.0028}$
8 – 16	$6.3 \pm 1.0^{+0.7}_{-0.6}$	$0.0211 \pm 0.0032^{+0.0013}_{-0.0015}$
16 – 80	$0.66 \pm 0.12^{+0.09}_{-0.05}$	$0.00221 \pm 0.00038^{+0.00026}_{-0.00014}$
$p_T^{*2}$ range ( $\text{GeV}^2$ )	$d\sigma/dp_T^{*2}$ (pb/ $\text{GeV}^2$ )	$1/\sigma d\sigma/dp_T^{*2}$
0 – 1	$80 \pm 14^{+8}_{-9}$	$0.269 \pm 0.041^{+0.012}_{-0.034}$
1 – 5	$40.1 \pm 4.1^{+5.7}_{-2.6}$	$0.1345 \pm 0.0096^{+0.0080}_{-0.0014}$
5 – 16	$3.81 \pm 0.70^{+0.44}_{-0.32}$	$0.0128 \pm 0.0022^{+0.0010}_{-0.0008}$
16 – 100	$0.280 \pm 0.051^{+0.031}_{-0.027}$	$0.00094 \pm 0.00017^{+0.00006}_{-0.00009}$
$Y^*$ range	$d\sigma/dY^*$ (pb)	$1/\sigma d\sigma/dY^*$
1.75 – 2.60	$80 \pm 16^{+9}_{-7}$	$0.274 \pm 0.045^{+0.017}_{-0.021}$
2.60 – 3.00	$212 \pm 28^{+30}_{-16}$	$0.722 \pm 0.083^{+0.052}_{-0.031}$
3.00 – 3.40	$211 \pm 25^{+18}_{-16}$	$0.716 \pm 0.077^{+0.026}_{-0.055}$
3.40 – 4.00	$94 \pm 14^{+18}_{-9}$	$0.321 \pm 0.045^{+0.041}_{-0.024}$

**Table A.2:** Differential cross sections and normalised differential cross sections in the kinematic region  $2 < Q^2 < 80 \text{ GeV}^2$ ,  $50 < W < 250 \text{ GeV}$ ,  $0.2 < z < 0.9$  and  $-1.6 < Y_{lab} < 1.3$  as a function of  $Q^2$ ,  $p_T^{*2}$  and  $Y^*$ . The first uncertainty is statistical and the second is systematic. Overall normalisation uncertainties due to the luminosity measurement ( $\pm 2\%$ ) and to the  $J/\psi$  decay branching ratio ( $1.7\%$ ) are not included in the systematic error.

$\log(M_X^2/\text{GeV}^2)$ range	$d\sigma/d\log(M_X^2/\text{GeV}^2)$ (pb)	$1/\sigma d\sigma/d\log(M_X^2/\text{GeV}^2)$
3.00 – 3.55	$156 \pm 18^{+19}_{-20}$	$0.556 \pm 0.057^{+0.052}_{-0.074}$
3.55 – 3.85	$208 \pm 27^{+25}_{-16}$	$0.740 \pm 0.091^{+0.056}_{-0.021}$
3.85 – 4.10	$270 \pm 40^{+38}_{-31}$	$0.96 \pm 0.13^{+0.09}_{-0.08}$
4.10 – 4.50	$164 \pm 31^{+21}_{-18}$	$0.581 \pm 0.092^{+0.054}_{-0.050}$
$Y_X$ range	$d\sigma/dY_X$ (pb)	$1/\sigma d\sigma/dY_X$
2.20 – 2.78	$112 \pm 21^{+13}_{-11}$	$0.383 \pm 0.061^{+0.033}_{-0.033}$
2.78 – 3.05	$243 \pm 37^{+33}_{-26}$	$0.83 \pm 0.11^{+0.08}_{-0.07}$
3.05 – 3.37	$203 \pm 26^{+29}_{-15}$	$0.692 \pm 0.083^{+0.067}_{-0.018}$
3.37 – 4.05	$143 \pm 16^{+17}_{-18}$	$0.488 \pm 0.047^{+0.044}_{-0.063}$

**Table A.3:** Differential cross sections and normalised differential cross sections in the kinematic region  $2 < Q^2 < 80 \text{ GeV}^2$ ,  $50 < W < 250 \text{ GeV}$ ,  $0.2 < z < 0.9$  and  $-1.6 < Y_{lab} < 1.3$  as a function of  $\log(M_X^2/\text{GeV}^2)$  and  $Y_X$ . The first uncertainty is statistical and the second is systematic. Overall normalisation uncertainties due to the luminosity measurement ( $\pm 2\%$ ) and to the  $J/\psi$  decay branching ratio ( $1.7\%$ ) are not included in the systematic error.

$z$ range	$d\sigma/dz$ (pb)	$1/\sigma d\sigma/dz$
0.30 – 0.45	$246 \pm 60^{+28}_{-29}$	$1.18 \pm 0.25^{+0.07}_{-0.13}$
0.45 – 0.60	$317 \pm 50^{+39}_{-24}$	$1.53 \pm 0.22^{+0.13}_{-0.10}$
0.60 – 0.75	$430 \pm 56^{+51}_{-34}$	$2.07 \pm 0.23^{+0.09}_{-0.11}$
0.75 – 0.90	$392 \pm 57^{+64}_{-41}$	$1.89 \pm 0.24^{+0.22}_{-0.17}$
$p_T^{*2}$ range (GeV <sup>2</sup> )	$d\sigma/dp_T^{*2}$ (pb/GeV <sup>2</sup> )	$1/\sigma d\sigma/dp_T^{*2}$
1 – 5	$36.4 \pm 3.7^{+4.1}_{-2.4}$	$0.1752 \pm 0.0092^{+0.0054}_{-0.0054}$
5 – 16	$3.65 \pm 0.71^{+0.17}_{-0.32}$	$0.0176 \pm 0.0030^{+0.0022}_{-0.0011}$
16 – 40	$0.92 \pm 0.18^{+0.12}_{-0.10}$	$0.00443 \pm 0.00083^{+0.00028}_{-0.00051}$
$Y^*$ range	$d\sigma/dY^*$ (pb)	$1/\sigma d\sigma/dY^*$
2.00 – 2.60	$66 \pm 14^{+7}_{-10}$	$0.351 \pm 0.066^{+0.023}_{-0.048}$
2.60 – 3.00	$137 \pm 20^{+15}_{-10}$	$0.728 \pm 0.094^{+0.053}_{-0.048}$
3.00 – 3.40	$144 \pm 19^{+13}_{-11}$	$0.762 \pm 0.091^{+0.035}_{-0.049}$
3.40 – 4.00	$61 \pm 14^{+12}_{-6}$	$0.323 \pm 0.064^{+0.049}_{-0.025}$

**Table A.4:** Differential cross sections and normalised differential cross sections in the kinematic region  $2 < Q^2 < 100 \text{ GeV}^2$ ,  $50 < W < 225 \text{ GeV}$ ,  $0.3 < z < 0.9$  and  $p_T^{*2} > 1 \text{ GeV}^2$  as a function of  $z$ ,  $p_T^{*2}$  and  $Y^*$ . The first uncertainty is statistical and the second is systematic. Overall normalisation uncertainties due to the luminosity measurement ( $\pm 2\%$ ) and to the  $J/\psi$  decay branching ratio (1.7%) are not included in the systematic error.



# Bibliography

- [1] NMC Coll., D. Allasia et al., Phys. Lett. **B 258**, 493 (1991).
- [2] EMC Coll., J. J. Aubert et al., Nucl. Phys. **B 213**, 1 (1983).
- [3] UA1 Coll., C. Albajar et al., Phys. Lett. **B 256**, 112 (1991).
- [4] CDF Coll., F. Abe et al., Phys. Rev. Lett. **69**, 3704 (1992).
- [5] E. L. Berger and D. Jones, Phys. Rev. **D 23**, 1521 (1981).
- [6] CDF Coll., F. Abe et al., Phys. Rev. Lett. **79**, 572 (1997).
- [7] CDF Coll., F. Abe et al., Phys. Rev. Lett. **79**, 578 (1997).
- [8] G. T. Bodwin, E. Braaten and G. P. Lepage, Phys. Rev. **D 51**, 1125 (1995).  
Erratum-ibid **D 55**, 5853 (1997).
- [9] DELPHI Coll., J. Abdallah et al., Phys. Lett. **B 565**, 76 (2003).
- [10] CDF Coll., T. Affolder et al., Phys. Rev. Lett. **85**, 2886 (2000).
- [11] BaBar Coll., B. Aubert et al., Phys. Rev. Lett. **87**, 162002 (2001).
- [12] Belle Coll., K. Abe et al., Phys. Rev. Lett. **88**, 52001 (2002).
- [13] S. Fleming et al. Phys. Rev. **D 68**, 094011 (2003).
- [14] Belle Coll., K. Abe et al. Phys. Rev. **D 70**, 071102 (2004).
- [15] L.V. Gribov, E.M. Levin and M.G. Ryskin, Phys. Rep. **100**, 1 (1983).
- [16] E.M. Levin and M.G. Ryskin, Phys. Rep. **189**, 267 (1990).

- [17] E.M. Levin et al., Sov. J. Nucl. Phys. **53**, 657 (1991).
- [18] E.M. Levin et al., Sov. J. Nucl. Phys. **54**, 867 (1991).
- [19] S. Catani, M. Ciafaloni and F. Hautmann, Phys. Lett. **B 242**, 97 (1990).
- [20] S. Catani, M. Ciafaloni and F. Hautmann, Nucl. Phys. **B 366**, 135 (1991).
- [21] J.C. Collins and R.K. Ellis, Nucl. Phys. **B 360**, 3 (1991).
- [22] G. Marchesini and R.K. Webber, Nucl. Phys. **B 386**, 215 (1992).
- [23] E.A. Kuraev, L.N. Lipatov and V.S. Fadin, Sov. Phys. JETP **44**, 443 (1976).
- [24] E.A. Kuraev, L.N. Lipatov and V.S. Fadin, Sov. Phys. JETP **45**, 199 (1977).
- [25] Ya.Ya. Balitskiĭ and L.N. Lipatov, Sov. J. Nucl. Phys. **28**, 822 (1978).
- [26] M. Ciafaloni, Nucl. Phys. **B 296**, 49 (1988).
- [27] S. Catani, F. Fiorani and G. Marchesini, Phys. Lett. **B 234**, 339 (1990).
- [28] A. V. Lipatov and N. P. Zotov, Eur. Phys. J. **C 27**, 87 (2003).
- [29] S. P. Baranov and N. P. Zotov, J. Phys., **G 29**, 1395 (2003).
- [30] S. P. Baranov, Phys. Rev. **D 66**, 114003 (2002).
- [31] H1 Coll., C. Adloff et al., Eur. Phys. J. **C 25**, 25 (2002).
- [32] ZEUS Coll., S. Chekanov et al., Eur. Phys. J. **C 27**, 173 (2003).
- [33] H1 Coll., C. Adloff et al., Eur. Phys. J. **C 25**, 41 (2002).
- [34] J. J. Aubert et al., Phys. Rev. Lett. **33**, 1404 (1974).
- [35] J. E. Augustin et al., Phys. Rev. Lett. **33**, 1406 (1974).
- [36] Y. S. Derbenev et al., Part. Accel. **8**, 115 (1978).
- [37] R. M. Barnett et al., Phys. Rev. Lett. **D54**, 1 (1996).
- [38] G. Zweig, *An  $SU(3)$  Model for Strong Interaction Symmetry and Breaking*, CERN preprint CERN-TH-412.

- 
- [39] R.G. Roberts ; “*The Structure of the Proton*”, CUP (1990).
- [40] C.G. Callan & D. Gross ; Phys. Rev. Lett. **22** (1969) 156.
- [41] T. Eichen et al., Phys. Lett. **B46**, 274. (1973).
- [42] TASSO Coll., R. Bradelik et al., Phys. Lett. **B86**, 243 (1979).
- [43] F. Halzen & A. Martin ; “*Quarks and Leptons*”, (1984).
- [44] H1 Collaboration, S. Aid et al., *Nucl. Phys.* **B 470** (1996) 3.
- [45] ZEUS Collaboration, M.Derrick et al., *Z. Phys.* **C 72** (1996) 3, 399-424.
- [46] G. Alterelli & G. Parisi ; Nucl. Phys. B126 (1977) 298.  
G. Alterelli ; Nucl. Phys. B91 (1981) 1.  
V.N. Gribov & L.N. Lipatov ; Sov. J. Nucl. Phys. 15 (1972) 438.  
L.N. Lipatov ; Sov. J. Nucl. Phys. 20 (1975) 96.  
Y.L. Dokshitzer ; Sov. Phys. JETP 46 (1977) 641.
- [47] R.K. Ellis, W.J. Stirling & B.R. Webber ; “*QCD and Collider Physics*” ; CUP (1996).
- [48] Ya. Balitski & L. Lipatov ; Sov. J. Nucl. Phys. 28 (1978) 822.  
E. Kuraev, L. Lipatov & V. Fadin ; Sov. Phys. JETP 45 (1977) 199.
- [49] S. Catani, M. Ciafaloni and F. Hautmann, Nucl. Phys. **B366**, 135 (1991).
- [50] Small-x Collab., B. Andersson et al., J. Mod. Phys. **A17**, 3185 (2002).
- [51] M. Ciafaloni, Nucl. Phys. **B 296**, 49 (1988).
- [52] S. Catani, F. Fiorani and G. Marchesini, Phys. Lett. **B 234**, 339 (1990).
- [53] ZEUS Collaboration; J.Breitweg et al., *Measurement of  $D^{*\pm}$  production and the charm contribution to  $F_2$  in deep inelastic scattering at HERA* The European Physical Journal **C12** 35 (2000) 1.
- [54] H1 Collaboration ; “*Determination of the Gluon Density in the Proton from Charm Electro- and Photo- Production using NLO QCD*” ; Abstract 538 ICHEP98, Vancouver.

- [55] H. Fritzsch, Phys. Lett. **B 67**, 217 (1977).
- [56] F. Halzen, Phys. Lett. **B 69**, 105 (1977).
- [57] M. Glück, J. Owens and E. Reya, Phys. Rev. **D 17**, 2324 (1978).
- [58] J.F. Amundson, O.J.P. Eboli, E.M. Gregores and F. Halzen, Phys. Lett. **B 390**, 323 (1997). Phys. Lett. **B 372**, 127 (1996).
- [59] G. T. Bodwin, E. Braaten and G. P. Lepage, Phys. Rev. **D 46**, 1914 (1992).
- [60] E. Braaten and S. Fleming, Phys. Rev. Lett. **74**, 3327 (1995).
- [61] W.E. Caswell and G. P. Lepage, Phys. Lett. **B 167**, 437 (1986).
- [62] ZEUS Collaboration, *The ZEUS Detector, Status Report 1993*, U. Holm ed. (1993).
- [63] *HERA: A Proposal for a Large Electron Proton Beam Facility at DESY* (Hamburg, 1981), DESY-HERA-81/10.
- [64] ZEUS Collaboration, *HERA Luminosity Upgrade Report for Funding Agencies*, October 28, 1997.
- [65] N. Harnew et al., Nucl. Inst. Meth. **A 279**, 290 (1989),  
B. Foster et al., Nucl. Phys. Proc. Suppl. **B 32**, 181 (1993),  
B. Foster et al., Nucl. Inst. Meth. **A 338**, 254 (1994).
- [66] M. Derrick et al., Nucl. Inst. Meth. **A 309**, 77 (1991),  
A. Andresen et al., Nucl. Inst. Meth. **A 309**, 101 (1991),  
A. Caldwell et al., Nucl. Inst. Meth. **A 321**, 356 (1992),  
A. Bernstein et al., Nucl. Inst. Meth. **A 336**, 23 (1993).
- [67] E. Iarocci et al., Nucl. Inst. Meth. **A 217**, 30, (1983).
- [68] G. Abbiendi et al., Nucl. Inst. Meth. **A 333**, 342, (1993).
- [69] W.H. Smith et al., *The ZEUS trigger system* (unpublished). Zeus-Note 89-084 (1989).
- [70] F. Chlebana, Zeus-Note 94-102 (1995).

- [71] A. Bamberger et al., *Nucl. Instr. and Meth.* **A 401** ( 1997) 63-80.
- [72] P. Göttlicher (for the ZEUS-HES Group). *The ZEUS hadron electron separator, performance and experience*, Proc. of 10th International Conference on Calorimetry in High Energy Physics (CALOR 2002) /R.-Y. Zhu (ed.). - Pasadena, California, 25-30 March 2002. - P.296-303.
- [73] Andruszkow, J. et al., *Luminosity measurement in the ZEUS experiment* Acta Phys. Polon. **B32**, 2025(2001).
- [74] H. Bethe and W. Heitler, Proc. Roy. Soc., **A 146**, 83 (1934),  
H. Bethe, Phys. Rev. **89**, 1256 (1953).
- [75] W.H. Smith et al., *The ZEUS trigger system*, Zeus–Note 89–084 (1989).
- [76] F. Chlebana, Zeus–Note 94–102 (1995).
- [77] INMOS Limited, *The Transputer Book*, 2<sup>nd</sup> edition (1989).
- [78] Brun, R., Bruyant, F., Maire, M., McPherson, A. C., *GEANT3*. CERN-DD/EE/84-1.
- [79] R. Sinkus & T. Voss, "Particle Identification with Neutral Networks Using a Rotational Invariant Moment Representation", DESY 96-264.
- [80] R. Sinkus & H. Abramowicz; "Electron Identification with Neural Networks at ZEUS", ZEUS–Note 93-117, 1993.
- [81] H. Abramowicz, A. Caldwell & R. Sinkus; NIM **A365** (1995) 508.
- [82] A. Lopez-Duran Viani, S. Schlenstedt. *Electron finder efficiencies and impurities. A comparison between SINISTRA95, EM and EMNET*, ZEUS–Note 99-078 (1999).
- [83] T. Doeker, A. Frey and M. Nakao, *Electron Position Reconstruction - Update of the ELECPO routines*, ZEUS–Note 94-123 (1994).
- [84] Ch. Amelung, *Electron Position Reconstruction in ZEUS: Further Update on the ELECPO Package (Based on 1995 Data)*, ZEUS–Note 96-093 (1996).

## **Bibliography**

---

- [85] J. Ng and W. Verkerke *An Overview of SRTD Analysis* ZEUS–Note 95-037 (1995).
- [86] Briskin, Gennady M. DESY-THESIS-1998-036.
- [87] Tuning, N., *ZUFOS: Hadronic final state reconstruction with calorimeter, tracking and backplash correction* (unpublished). ZEUS–Note 01-021, 2001.
- [88] Longhin, A., *Misura delle sezioni d'urto di fotoproduzione di Open Beauty ad HERA. (In Italian)* (unpublished). PhD Thesis at the University of Padua, 2000.
- [89] F. Goebel, *Measurement of the Diffractive Contribution to the DIS Cross Section using the ZEUS Forward Plug Calorimeter*. Report DESY–THESIS–2001–049, 2001.
- [90] M. Ernst, *Electron–hadron separation in a ZEUS FCAL prototype including HES diodes. Report on an analysis of CERN test data.* (unpublished). ZEUS–91-042, 1991.
- [91] J.I. Fleck, K. Ohrenberg, *Electron identification in the HES and a new way to determine the efficiency of electron finders (unpublished)*. ZEUS–95-009, 1995.
- [92] J. Ng and W. Verkerke, *An Overview of SRTD Analysis*. (unpublished) ZEUS–95–037, 1995.
- [93] A. Kreisel, *Improving SRTD position reconstruction*. (unpublished) ZEUS–03–007, 2003.
- [94] F. Jacquet & A. Blondel; Proceedings of the Study for an *ep* facility in Europe, DESY-79/48 (1979).
- [95] S. Bentvelsen, J. Engelen & P. Kooijman; Proc. of Workshop on Physics at HERA 1991, 23.
- [96] U. Bassler & G. Bernadi; NIM A361(95) 197.
- [97] G.F. Hartner et al., ZEUS–Note 97-064, 1997,  
G.F. Hartner, ZEUS–Note 98-058, 1998.

- [98] P. Billoir and S. Qian, Nucl. Inst. Meth. **A311** (1992).
- [99] G. Abbiendi, Global tracking of Muons in the Barrel and Rear Region (unpublished). ZEUS–Note 99-063, 1999.
- [100] Kuzmin, V. A., Nucl. Instrum. Meth. **A453**, 336 (2000).
- [101] S. Limentani, M. Posocco and L. Stanco, *Muon Barrel Reconstruction*, ZEUS–Note 98-058.
- [102] V. Innocente, M. Maire and E. Nagy, *GEANE: average tracking and error propagation package*, proceedings of MC91: Detector and event simulation in High Energy Physics, Amsterdam, 1991.
- [103] ZEUS Collaboration ; “*Measurement of the Proton Structure Function  $F_2$  in  $e^+p$  Collisions at HERA*”, Abstract 769 ICHEP98, Vancouver.
- [104] B. Straub, [http://www-zeus.desy.de/~straub/ZEUS\\_ONLY/doc/em.ps](http://www-zeus.desy.de/~straub/ZEUS_ONLY/doc/em.ps).
- [105] T. Doeker, A. Frey and M. Nakao, *Electron Position Reconstruction - Update of the ELECPO routines*, ZEUS–Note 94-123 (1994).
- [106] Ch. Amelung, *Electron Position Reconstruction in ZEUS: Further Update on the ELECPO Package (Based on 1995 Data)*, ZEUS–Note 96-093 (1996).
- [107] L. Adamczyk et al. *Luminosity measurement in the ZEUS experiment*. ZEUS–Note 01-004.
- [108] [http://www-zeus.desy.de/~mturcato/ZEUS\\_ONLY/BMUON/mbtake.fpp](http://www-zeus.desy.de/~mturcato/ZEUS_ONLY/BMUON/mbtake.fpp).
- [109] Particle Data Group, S. Eidelman et al. Phys. Lett. **C 592**, 1 (2004).
- [110] H. Jung and G. P. Salam, Eur. Phys. J. **C 19** (2001)
- [111] H. Jung, Proc. Workshop on Physics at HERA, W. Buchmueller and G. Ingelman (eds.), Vol. 3, p. 1488. Hamburg, Germany, DESY (1992).
- [112] M. Kasprzak, *Inclusive Properties of Diffractive and Non-diffractive Photoproduction at HERA*. Ph.D. Thesis, Warsaw University, Warsaw, Poland, Report DESY F35D-96-16, DESY, 1996.

- [113] L. Adamczyk, *Vector Meson Photoproduction at Large Momentum Transfer at HERA*. Ph.D. Thesis, University of Mining and Metallurgy, Cracow, Poland, Report DESY-THESIS-1999-045, DESY, 1999
- [114] B. List and A. Mastroberardino, *Proc. Workshop on Monte Carlo Generators for HERA Physics*, p. 396. DESY, Hamburg, Germany (1999). Also in preprint DESY-PROC-1999-02.
- [115] M. Hansson and J. Jung, Preprint hep-ph/0309009, 2003.
- [116] B. Andersson et al., Rep. **97**, 31 (1983).
- [117] T. Sjöstrand, Comp. Phys. Comm. **82**, 74 (1994).
- [118] Small x Coll., B. Andersson et al., Eur. Phys. J. **C 25**, 77 (2002).
- [119] A. Bertolin, R. Brugnera, *Inelastic  $\psi'$  and  $J/\psi$  photoproduction at HERA* (unpublished), 2003 ZEUS-Note 03-004, 2003.
- [120] A. Meyer, *Charmonium Production in deep inelastic scattering at HERA*. Ph.D. Thesis, II. Exp. Phys. Inst. Univ. HH, Hamburg (Germany), Report DESY-THESIS-1998-012, 1998.
- [121] S. Mohrdieck, *Inelastische  $J/\psi$ -Erzeugung in Elektroproduktion am H1 Experiment bei HERA*. Ph.D. Thesis, II. Exp. Phys. Inst. Univ. HH, Hamburg (Germany), Report DESY-THESIS-2000-059, 2000.
- [122] S. Fleming, T. Mehen, Leptoproduction of  $J/\psi$ , Phys. Rev., D **57**, 1846, (1998).
- [123] M. Krämer, Prog. Part. Nucl. Phys., **47**, 141 (2001).
- [124] M. Krämer et al., Phys. Lett. **B 348**, 657 (1995).
- [125] M. Krämer Nucl. Phys. **B 459**, 3 (1996).
- [126] A. Kwiatkowski, H. Spiesberger and H.-J. Möhring, Comp. Phys. Comm. **69**, 155 (1992).
- [127] H. Jung, Comp. Phys. Comm. **86**, 147 (1995).

- [128] ZEUS Coll., S. Chekanov et al., Eur. Phys. J. **C 27**, 173 (2003).
- [129] ZEUS Coll., S. Chekanov et al., Phys. Rev. **D 69**, 12004 (2004).
- [130] M. Turcato, Ph.D. Thesis, Padova University (2002). DESY-THESIS-2003-039.
- [131] B. A. Kniehl and L. Zwirner, Nucl. Phys. **B 621**, 337 (2002).
- [132] A. V. Lipatov and N. P. Zotov, Eur. Phys. J. **C 27**, 83 (2003).
- [133] M. Beneke, G. A. Schuler and S. Wolf, Phys. Rev. **D 62**, 34004 (2000).
- [134] J. Kwiecinski, A. D. Martin and A. M. Stasto, Phys. Rev. **D 56**, 3991 (1997).
- [135] G. Ingelman, A. De Roeck, and R. Klanner, DESY-96-235.
- [136] ZEUS Collaboration, A Microvertex Detector for ZEUS, ZEUS Note 97-006, 22 January 1997.
- [137] ZEUS Collaboration, A Straw-Tube Tracker for ZEUS, ZEUS Note 98-046, 24 June 1998.
- [138] B. Dolgoshein, Nucl. Instrum. Methods **A 326** (1993) 434.
- [139] A. Antonov et al., Nucl. Instrum. Methods **A 449** (2000) 446.
- [140] T. Affolder, CDF Central Outer Tracker, FERMILAB-Pub-03/355-E.
- [141] W.W.M Allison and J.H. Cobb, Ann. Rev. Nucl. Part. Sci. **30** (1980) 253.
- [142] S.F. Biagi, Nucl. Instrum. Methods **A 283** (1989) 716.
- [143] S. Fourletov, Nucl. Inst. Meth. **A 535**, 191 (2004).
- [144] P.V.C. Hough, *Machine Analysis of Bubble Chamber Pictures*, Int. Conf. on High Energy Accelerators and Instrumentation, 554-556, CERN, 1959.
- [145] D. Shaw, D.M. Gingrich and K. Long, *A Technique for Evaluating Pattern Recognition Performance in Tracking Chambers*. ZEUS-Note 90-101 (1990).
- [146] CDF Collaboration A. Abulencia et al., *Polarization of  $J/\psi$  and  $\psi(2S)$  mesons produced in  $p$  anti- $p$  collisions at  $\sqrt{s} = 1.96$  TeV*. FERMILAB-PUB-07-072-E, Apr 2007.

# Acknowledgments

The results presented in this thesis are based on the constant efforts of the members of the ZEUS collaboration and would not have been possible without their help and support. I am very grateful for the friendly atmosphere within the ZEUS collaboration.

I would like to thank my professor, Prof. Dr. Robert Klanner, for giving me the opportunity to work on my PhD in the ZEUS collaboration. I am thankful for all his support during my work. Especially I want to thank him for many long and fruitful discussions and patient explanations and for reading and discussing my thesis draft.

The work in the ZEUS Heavy Flavour group I enjoyed very much. I would like to thank Richard Hall-Wilton, Massimo Corradi, Matthew Wing and Achim Geiser for their coordinating efforts and for answering numerous questions concerning the analysis. Special thanks to Leonid Gladilin, Rik Yoshida and Elisabetta Gallo for the useful comments and advises. The achievement of the results was possible due to the very good collaboration with my colleagues Alessandro Bertolin, Riccardo Brugnera and in particular with Igor Katkov.

I owe special thanks to Prof. Dr. Boris Dolgoshein. I would like to thank him for giving me the opportunity to work within the ZEUS collaboration and for his continuous support during my work at the DESY.

Many thanks to my colleagues from Moscow Engineering and Physics Institute Alexei Stifutkin, Sergey Fourletov, Julia Fourletova, Dmitri Gladkov, Igor Rubinskiy, Valerij Sosnovtsev, Anatoli Romaniouk, Pavel Nevski.

My family has a big share in what I achieved during the last years. I want to thank my parents, who supported me during the years of study and who encouraged me and guided me with their advice and example. And I want to thank my wife Tatiana for help in everything I did.

